bioRxiv preprint doi: https://doi.org/10.1101/632547; this version posted May 9, 2019. The copyright holder for this preprint (which was not certified by peer review) is the author/funder. All rights reserved. No reuse allowed without permission.

Systematic discovery of Short Linear Motifs decodes calcineurin phosphatase signaling

Callie P. Wigington[1&], Jagoree Roy[1&], Nikhil P. Damle[1*], Vikash K. Yadav[2^], Cecilia Blikstad[2$], Eduard Resch[3], Cassandra J. Wong[4], Douglas R. Mackay[5], Jennifer T. Wang[1], Izabella Krystkowiak[6], Tim Stearns[1], Anne-Claude Gingras[4,7], Katharine S. Ullman[5], Ylva Ivarsson[2], Norman E. Davey[8#] and Martha S. Cyert[1#]

1. Department of Biology, Stanford University
2. Department of Chemistry – BMC, Uppsala University, Uppsala, Sweden
3. Fraunhofer Institute for Molecular Biology and Applied Ecology (IME), Branch for Translational Medicine and Pharmacology (TMP), Frankfurt am Main, Germany
4. Lunenfeld-Tanenbaum Research Institute at Mount Sinai Hospital, University of Toronto, Toronto, Canada
5. Department of Oncological Sciences, Huntsman Cancer Institute, University of Utah, Salt Lake City, Utah
6. Conway Institute of Biomolecular and Biomedical Research, University College Dublin, Belfield, Dublin 4, Ireland
7. Department of Molecular Genetics, University of Toronto, Toronto, M5S 3H7 ON, Canada
8. Division of Cancer Biology, The Institute of Cancer Research, 237 Fullham Road, London SW3 6JB, UK

[&]Contributed equally to this work

* Present address: OSTHUS GmbH, Aachen, Germany
^ Present address: Department of Biochemistry, University of Oxford, UK
[$] Present address: Department of Molecular and Cell Biology, University of California, Berkeley, US

#Corresponding authors
mcyert@stanford.edu
norman.davey@icr.ac.uk

bioRxiv preprint doi: https://doi.org/10.1101/632547; this version posted May 9, 2019. The copyright holder for this preprint (which was not certified by peer review) is the author/funder. All rights reserved. No reuse allowed without permission.

Summary

Short linear motifs (SLiMs) form dynamic protein-protein interactions essential for signaling, but sequence degeneracy and low binding affinities make them difficult to identify. We harnessed unbiased systematic approaches for SLiM discovery to elucidate the regulatory network of calcineurin (CN), the Ca^{2+}-regulated phosphatase that recognizes LxVP and PxIxIT motifs. *In vitro* proteome-wide detection of CN-binding peptides, *in situ* SLiM-dependent proximity labeling, and *in silico* modeling of motif determinants uncovered unanticipated CN interactors, including Notch1, which we establish as a CN substrate. Unexpectedly, CN shows SLiM-dependent proximity to centrosomal and nuclear pore complex (NPC) proteins – structures where Ca^{2+} signaling is largely uncharacterized. CN dephosphorylates human and yeast NPC proteins and promotes accumulation of a nuclear reporter, suggesting conserved NPC regulation by CN. The CN network assembled here provides a resource to investigate Ca^{2+} and CN signaling and the demonstrated synergy between experimental and computational methods establishes a blueprint for examining SLiM-based networks.

bioRxiv preprint doi: https://doi.org/10.1101/632547; this version posted May 9, 2019. The copyright holder for this preprint (which was not certified by peer review) is the author/funder. All rights reserved. No reuse allowed without permission.

Introduction

Cellular networks signal through dynamic protein-protein interactions (PPIs), many of which are formed by low-affinity docking of short linear interaction motifs (SLiMs) onto globular domains. These degenerate 3-10 amino acid long sequences occur in intrinsically disordered protein regions (Tompa et al., 2014). SLiMs also evolve rapidly to rewire signaling networks and are sites of many disease-causing mutations (Davey et al., 2017; Uyar et al., 2014). Up to one hundred thousand distinct SLiMs, most of which are yet to be identified, are thought to underlie the transient, dynamic, and often conditional regulatory interactome of the human cell (Tompa et al., 2014). These interactions determine many critical properties of a protein including complex association, protein modification state, localization, and stability, and thereby control much of the decision making that directs a protein from translation to degradation (Van Roey et al., 2014). Recent discoveries show that SLiMs mediate specific interactions between protein phosphatases and their substrates (Brautigan and Shenolikar, 2018; Ivarsson and Jemth, 2018; Kataria et al., 2018). Systems-level elucidation of protein phosphatase signaling has been limited by technical challenges to substrate identification, but rapidly developing methods for SLiM discovery can now be harnessed to revolutionize our understanding of these enigmatic enzymes (Davey et al., 2017; Krystkowiak et al., 2018).

Calcineurin (CN; also known as PP2B or PPP3) is the only phosphoserine/threonine protein phosphatase that is regulated by Ca^{2+} and calmodulin. This highly conserved phosphatase is ubiquitously expressed and plays critical regulatory roles in the cardiovascular, nervous and immune systems; however, only ~70 proteins are currently established as CN substrates (Table S4). CN is required for T-cell activation, where it dephosphorylates the Nuclear Factor of Activated T-cells (NFAT) family of transcription factors (Jain et al., 1993). Consequently, CN inhibitors FK506 (Tacrolimus) and cyclosporin A (CsA), are commonly prescribed as immunosuppressants (Liu, 1993). Unfortunately, due to CN inhibition in non-immune tissues, these drugs also cause a range of unwanted effects, including hypertension, diabetes, and seizures (Roy and Cyert, 2019). Systematically mapping CN signaling pathways throughout the body will aid in understanding and potentially ameliorating these effects.

The CN heterodimer, composed of two subunits (catalytic: CNA, regulatory: CNB), recognizes substrates by binding to PxIxIT and LxVP SLiMs (Figure 1A), a mechanism that is evolutionarily conserved (Roy and Cyert, 2009). However, positioning of these motifs with respect to each other, and to sites of dephosphorylation varies between substrates, and these motifs play distinct roles during dephosphorylation (Nygren and Scott, 2016; Roy and Cyert, 2019). Under non-signaling conditions, the CN heterodimer is inactive due to masking of the active site by autoinhibitory sequences in CNA. During signaling, Ca^{2+} binding sites in CNB become occupied, and Ca^{2+}-bound calmodulin interacts with CNA to affect conformational changes that disrupt autoinhibition and activate the enzyme (Roy and Cyert, 2019). PxIxIT docking on CNA is unaffected by CN activation, thus these peptides target CN to substrates and regulators under both basal and signaling conditions. In contrast, LxVP motifs bind to a hydrophobic groove that becomes accessible only after calmodulin binds to CNA, and are thought to orient phosphorylated residues for catalysis (Roy and Cyert, 2019). Mutation of PxIxIT or LxVP sequences in substrates or their conserved binding surfaces on CN disrupts dephosphorylation, and many CN inhibitors, including CsA, FK506, and the viral A238L protein, function by blocking SLiM binding (Grigoriu et al., 2013). Although these SLiMs have been characterized at the structural level (Li et al., 2004; Sheftic et al., 2016), the small number of validated PxIxIT and

bioRxiv preprint doi: https://doi.org/10.1101/632547; this version posted May 9, 2019. The copyright holder for this preprint (which was not certified by peer review) is the author/funder. All rights reserved. No reuse allowed without permission.

LxVP instances in humans has limited our understanding of the specificity determinants of the CN SLiM-binding pockets and hampered global identification of these motifs.

In this work, we discover unexpected functions and substrates of CN by systematically identifying CN-binding SLiMs in the human proteome. Using proteomic phage display (ProP-PD), we uncovered and validated PxIxIT and LxVP sequences in 40 proteins whose association with CN is unexplored. These include the Notch1 intracellular domain (NICD), which we show is dephosphorylated by CN *in vivo* and *in vitro*. Furthermore, using this rich collection of motifs we developed powerful *in silico* tools that identified CN-binding SLiMs throughout the proteome. Finally, we probed SLiM-dependent CN associations *in vivo* via proximity labeling (BioID) with wildtype and docking-defective versions of CN, which revealed its surprising proximity to proteins at the centrosome and the nuclear pore complex (NPC). We identify an unanticipated, conserved role for CN at the NPC by demonstrating SLiM-dependent dephosphorylation of human and yeast NPC nuclear basket proteins by CN *in vitro*, and by showing that CN activity is required for efficient nuclear accumulation of a reporter cargo *in vivo*. In this work, experimental and computational approaches synergize to transform our understanding of Ca^{2+}/CN signaling and establish a blueprint for future investigations of SLiM-based networks.

Results

Proteomic Peptide Phage Display discovers human CN-binding peptides

To discover human CN-binding peptides, we utilized Proteomic Peptide Phage Display (ProP-PD), a powerful method for direct identification of SLiMs (Davey et al., 2017). Phages displaying a library of 479,846 overlapping 16-mer peptides from 18,682 proteins representing all intrinsically disordered regions of the human proteome, where SLiMs reside (Tompa et al., 2014), were selected using recombinant heterodimeric CN as bait. Constitutively active, truncated CN was used (O'Keefe et al., 1992) to ensure the accessibility of both PxIxIT and LxVP binding surfaces, and selections were performed with and without Ca^{2+}, which enhances the binding of LxVP peptides to CN (Rodriguez et al., 2009) (see STAR methods). Selections employed truncated CN_{WT} and mutants, CN_{NIR} and CN_{WF}, which have reduced binding to PxIxIT or LxVP peptides, respectively (Figure 1A, S1D) (Li et al., 2004; Rodriguez et al., 2009), and were successful with CN_{WT} and CN_{NIR}, but not CN_{WF} (Figure S1B). Sequencing of final phage pools from the WT and NIR datasets identified 214 unique peptides (Figure 1C). Among these were eight established CN-binding SLiMs, some of which were represented by a single sequence read (Table S1). Therefore, to preserve the maximum number of potential CN-binding peptides we analyzed this entire dataset, which likely includes non-specific binders.

Identification of enriched motifs within the ProP-PD peptides

To identify possible SLiMs in the ProP-PD dataset, all (214) peptides were analyzed using SLiMFinder (Edwards et al., 2007), which detected L.VP as the most highly enriched motif with 44 instances (significance: $<1e^{-16}$), four of which are established LxVP sequences in CN substrates (Figure 1B, Table S1). No PxIxIT-like motifs were enriched, although four previously identified PxIxIT sequences were identified in the data set. We reasoned that PxIxIT-containing peptides should preferentially bind CN_{WT} vs CN_{NIR} (as observed for the known PxIxIT-containing peptides, Table S1), and thus analyzed 137 peptides that were detected only in CN_{WT} selections (Figure 1B, S1C). This revealed multiple enriched PxIxIT-related motifs, the most permissive of which, P.[FILV].[FILV], identified 30 instances (significance: $9.76e^{-10}$), including the known PxIxIT sequences (Table S1). Surprisingly, we noticed that three of these peptides contained both motifs in one ‘combination’ sequence i.e. L.VP.[FILV].[FILV], and found two additional instances of this longer motif within the total peptide set. Therefore, in total these analyses

bioRxiv preprint doi: https://doi.org/10.1101/632547; this version posted May 9, 2019. The copyright holder for this preprint (which was not certified by peer review) is the author/funder. All rights reserved. No reuse allowed without permission.

identified 39 L.VP instances, 25 P.[FILV].[FILV] instances, and 5 peptides where both motifs overlap (Figure 1C, S1A).

Validation of peptide binding to CN

Because the vast majority of these sequences were not known to bind CN, we measured the ability of ProPD-isolated peptides (fused to GST) to co-purify with heterodimeric CN_{WT} relative to peptides containing known motifs and GST alone (negative control). 23 of 36 newly detected L.VP-containing peptides showed significant binding to CN_{WT}, and co-purified with CN to different extents relative to peptides containing established LxVP motifs from NFATc1, NFATc2 and KSR2 (Figures 1D) (See STAR methods). Furthermore, these peptides displayed reduced binding to CN_{WF}, indicative of LxVP-directed interactions (Figures 1D, E, S2B). As a complementary approach to establishing motif function, we showed that mutating the LxVP motif in a peptide from Notch1 ($Notch1_{MUT}$) reduced binding to CN_{WT} (Figure 1E).

Similarly, the ability of peptides containing the enriched P.[FILV].[FILV] motif to bind CN_{WT} was examined relative to the well characterized PxIxIT from NFATc1 and GST alone. Excluding previously characterized motifs (Table S1), we tested 20 peptides,16 of which showed significant, PxIxIT-dependent binding to CN_{WT} (Figure 1F, 1G, S2C). Two of these peptides (from SSC5D and LCORL) each contained a pair of PxIxIT sequences that both contributed to CN binding (data not shown). Thus, in total 18 novel CN-binding PxIxIT motifs were identified. Furthermore, upon mutation of the PxIxIT sequence in a Nup153 peptide ($Nup153_{MUT}$; Figure 1G), CN_{WT} co-purification was disrupted, confirming that the identified motif is a critical binding determinant.

Finally, we predicted that 5 “combination” peptides in our dataset, containing coincident L.VP and P.[FILV].[FILV] motifs (Table S1), would display properties of both SLiMs. Four of these showed CN binding. Analysis of the peptide from CACNA1H (which contains a previously identified LxVP sequence (Huang et al., 2013)) showed that co-purification with CN_{WT} was reduced upon mutation of LxV or IxIT residues (Figure 1H), and that binding to CN_{NIR} or CN_{WF} was significantly reduced (undetectable) relative to CN_{WT} (Figure S2A). Thus, both PxIxIT and LxVP-type binding modes were evident in this single peptide, properties also displayed by the peptide from C16orf74 (previously identified as a PxIxIT (Nakamura et al., 2017)) (data not shown).

Of the 145 remaining peptides, 26 that either contained enriched motifs related to L.VP or P.[FILV].[FILV], or no motifs were tested for *in vitro* binding to CN_{WT}. The vast majority of these (24) showed no CN-binding (data not shown, Table S1), increasing our confidence that the majority of CN-binding peptides had been characterized.

In summary, our ProP-PD analyses tripled the number of validated LxVP and PxIxIT motifs from 22 to 67 (Figures 3A, 3B) and uncovered peptides with characteristics of both motifs. Together these analyses highlight the ability of an unbiased proteome-wide selection method to detect previously unknown CN-binding SLiMs in disordered regions of human proteins.

Newly discovered SLiMs identify Notch1 as a CN substrate

Proteins containing the CN-binding SLiMs described above include two previously established CN substrates (Filamin A and KCNJ8; Table S1) and uncover putative CN-interactors with a variety of biological functions (Figure 2A, Table S1). These proteins include Nup153, a nucleoporin and component of the NPC, as well as Notch1, a critical developmental regulator. Association of the Nup153 and Notch1 proteins with CN was further investigated *in vivo* using proximity-dependent labeling with the promiscuous biotin ligase, BirA*. The sensitivity of this method (BioID) allows transient, low-affinity interactions, such as those mediated by

bioRxiv preprint doi: https://doi.org/10.1101/632547; this version posted May 9, 2019. The copyright holder for this preprint (which was not certified by peer review) is the author/funder. All rights reserved. No reuse allowed without permission.

SLiMs, to be detected (Gingras et al., 2018; Roux et al., 2012). Consistent with the presence of a demonstrated PxIxIT motif in Nup153, exogenously expressed FLAG-Nup153 (full-length protein) showed reduced biotinylation with BirA*-CN_{NIR} vs -CN_{WT}, and biotinylation of FLAG-Nup153 containing a mutated PxIxIT motif ($PxIxIT_{MUT}$) was reduced with both enzymes (Figure 2B). Notch1 is a large transmembrane receptor that is cleaved in response to ligand binding to produce an intracellular domain (NICD; Figure 2C), which enters the nucleus and induces gene expression (Tzoneva and Ferrando, 2012). Consistent with the identification of a LxVP motif in the NICD C-terminus, FLAG-$NICD_{WT}$ was biotinylated significantly more by BirA*-CN_{WT} than BirA*-CN_{WF}, and biotinylation of FLAG-NICD-$LxVP_{MUT}$, containing a mutated LxVP motif, was significantly reduced relative to $NICD_{WT}$ (Figure 2D). Together, these data show that identified SLiMs in Nup153 and Notch1 mediate proximity, and likely direct interaction with CN *in vivo*.

To examine whether Notch1 is a direct substrate of CN, we expressed FLAG-NICD in HEK293 Flp-In T-REx cells. Co-expression of constitutively active, truncated CN (CN_{trunc}) consistently increased the electrophoretic mobility of $NICD_{WT}$ but not NICD-$LxVP_{MUT}$, and this shift was counteracted by the CN inhibitor, FK506 (Figure 2E). Furthermore, incubating immunopurified FLAG-$NICD_{WT}$ with CN_{trunc} or the non-specific λ phosphatase *in vitro* caused an increase in electrophoretic mobility that was blocked by phosphatase inhibitors, demonstrating that observed mobility shifts reflect changes in the phosphorylation state of NICD (Figure 2F). In contrast, the electrophoretic mobility of NICD-$LxVP_{MUT}$ increased upon incubation with λ but not CN_{trunc}. Together, these findings demonstrate SLiM-dependent regulation of NICD phosphorylation by CN *in vivo* and *in vitro* and establish the NICD as a direct CN substrate. The LxVP motif identified here resides within a C-terminal PEST domain that promotes rapid phosphorylation-dependent degradation of NICD (Figure 2C) (Tzoneva and Ferrando, 2012) and we note that NICD-$LxVP_{MUT}$ levels were reduced relative to $NICD_{WT}$ (Figure 2E). Furthermore, levels of $NICD_{WT}$ but not NICD-$LxVP_{MUT}$ increased with CN_{trunc} expression, although FK506 failed to significantly reverse this effect (Figure S3A). These observations suggest possible regulation of NICD stability by CN and are consistent with reports that CN promotes Notch signaling (Kasahara et al., 2013; Mammucari et al., 2005; Medyouf et al., 2007). Importantly, our analyses with NICD support the use of SLiM identification and disruption as a tool to elucidate CN signaling across the human proteome.

Computational prediction and validation of CN-binding SLiMs

To further expand the set of CN-binding motifs, we next developed *in silico* tools, based on SLiMs from our ProP-PD selections and previously published CN-binding sequences (Table S4), to discover PxIxIT and LxVP sequences in the human proteome. Validated CN-binding sequences were used to construct specificity-determinant models that reflect the physiochemical preferences of the core and flanking residues of each motif (Figures 3A and B; Table S2) (Roy and Cyert, 2019; Sheftic et al., 2016) (Nguyen et al. bioRxiv 306779). Position-specific Scoring Matrices (PSSMs), statistical models that include weighted sequence information at each motif position, were built to represent these specificity determinants. The PSSMs were assessed by leave-one-out cross-validation and shown to be robust, sensitive, and specific (see STAR Methods) (Figures S4B and C).

To identify putative PxIxIT and LxVP motifs in the human proteome, a series of filtering steps were applied (schematized in Figure S4A). All peptides matching a loose regular expression for each motif (P[^PG][ILVF][^PG][ILVF][^PG] or Lx[VLI]P) were scored and ranked using the PSSM. Next, 1,121 PxIxIT and 1,167 LxVP instances with PSSM p-values ≤ 10^{-4} were filtered using additional criteria: 1) Due to CN localization in the cytosol and nucleoplasm (Hallhuber et al., 2006), any extracellular, transmembrane, or intra-organellar sequences were removed; 2) Because SLiMs are found in regions of intrinsic disorder (Tompa et al., 2014) and >

bioRxiv preprint doi: https://doi.org/10.1101/632547; this version posted May 9, 2019. The copyright holder for this preprint (which was not certified by peer review) is the author/funder. All rights reserved. No reuse allowed without permission.

90% of our training peptides exhibit high predicted disorder scores (Table S2), sequences were limited to those with an IUPRED disorder propensity score ≥ 0.30, which significantly improved predictive power (Table S2). Although conservation did provide some additional predictive power (Table S2), we chose not to employ this characteristic as a filter, as our previous work on the yeast CN network revealed rapid evolution of PxIxIT motifs (Goldman et al., 2014).

After applying these additional criteria, the performance of each PSSM was compared to that of 1,000 randomly shuffled variants of the PSSMs using two sets of proteins that should be enriched for CN interactors: 1) The Protein-protein Interaction (PPI) dataset, which contains 182 CN-interacting proteins obtained from high- or low-throughput studies and reported in public databases (Table S4) and 2) The Positive Reference Set (PRS), which was assembled manually and contains 104 proteins that are dephosphorylated by CN *in vitro*, directly interact with CN, and/or display CN-dependent phosphorylation *in vivo* (Table S4). Both PxIxIT and LxVP PSSMs discovered a statistically enriched number of motif-containing proteins in each of these datasets and, when compared to randomly shuffled matrices, were among the top performing PSSMs (Figures 3E and F; Table S2). These analyses uncovered a PxIxIT motif in a CN-binding region of B-RAF (Duan and Cobb, 2010), as well as conserved PxIxIT and LxVP motifs in the CN-regulated MEF2A transcription factor (Bassel-Duby and Olson, 2006; Pan et al., 2004; Tian et al., 2010). Additional motifs discovered include a conserved PxIxIT in the synaptic vesicle protein, amphiphysin (Bauerfeind et al., 1997), and a combination motif in MAP3K7/TAK1, which regulates Jnk/p38 (Liu et al., 2009). These peptides displayed binding to CN_{WT} that was decreased by mutations in the predicted PxIxIT and/or LxVP motifs (Figure S4D). Taken together, these findings establish that our *in silico* tools identify biologically valid CN-interacting SLiMs, and can be used for systematic prediction of CN targets in the human proteome.

Using this *in silico* strategy, 409 putative PxIxITs and 410 putative LxVPs in 342 and 389 unique proteins, respectively, were identified in the human proteome (Figure 3D), with the vast majority of these containing a single motif instance. Current mechanistic understanding of CN suggests that both PxIxIT and LxVP motifs are utilized during dephosphorylation (Roy and Cyert, 2019), so we were surprised that our PSSM analyses identified only 40 proteins with both motifs (Figure 3D). Because PSSM scoring and filtering steps were optimized for selectivity rather than sensitivity, it is likely that many proteins contain degenerate motifs that are functional, but relatively low scoring. In fact, multivalent SLiM-mediated interactions are often driven by a single high-affinity/consensus motif, known as a gatekeeper motif, in combination with degenerate variants of the motif that often diverge significantly from the classical consensus (Ivarsson and Jemth, 2018; Stevers et al., 2018; Yaffe, 2002).

Together, these analyses predict hundreds of PxIxIT and LxVP instances in putative CN-interacting proteins across the human proteome and suggest broad regulatory roles for CN, many of which are not represented in the current literature. Furthermore, because CN, and in particular its SLiM-binding surfaces, is highly conserved, our computational tools can be used to identify CN-binding motifs in a wide range of organisms, and thus serve as a valuable resource for the Ca^{2+} signaling community. To this end, we developed a web-based resource to disseminate our findings and to identify putative CN-binding motifs in any protein or proteome of interest: **http://slim.ucd.ie/motifs/calcineurin/**.

Proximity-dependent biotinylation (BioID) identifies candidate CN interactors

To complement *in silico* analyses, which identify a “parts list” for CN interactions across the proteome, we explored the spatial distribution of CN within a cell, which should reflect the abundance and affinity of its SLiM-containing interacting partners (Roy et al., 2007). To accomplish this, we used proximity-dependent biotinylation coupled to mass spectrometry

bioRxiv preprint doi: https://doi.org/10.1101/632547; this version posted May 9, 2019. The copyright holder for this preprint (which was not certified by peer review) is the author/funder. All rights reserved. No reuse allowed without permission.

(PDB-MS), which sensitively maps subcellular organization (Gingras et al., 2018). Biotinylated proteins were identified by MS from HEK293 Flp-In T-REx cells stably expressing BirA*, BirA*-CN_{WT}, or docking mutants, -CN_{NIR} or -CN_{WF} (Figures 1A, 4A) (see STAR methods). BirA*-CN_{WT} specifically biotinylated 397 endogenous proteins (Table S3), including established CN substrates and regulators (AKAP5, PRKAR2A, RCAN1 and NFATc3), candidate interactors identified via ProP-PD (RTN1A and WNK2), and 50 proteins with computationally-identified SLiMs (Table S4). Importantly, proximity to CN was SLiM-dependent (Log_2WT/Mut > 0.5) for almost half of these proteins (196/397), which showed reduced biotinylation by BirA*-CN_{NIR} (139) and/or -CN_{WF} (133) relative to BirA*-CN_{WT} (Figures 4B and S5A). This group of docking-dependent proximal proteins was statistically enriched for proteins with PxIxIT and/or LxVP motifs identified by PSSMs, and more SLiM-containing proteins were identified by true PSSMs compared to the majority of shuffled PSSMs (Figure S5B, Table S2). In contrast, neither PSSM identified a statistically enriched number of motif-containing proteins in the set of SLiM-independent CN proximal proteins or in the CRAPome (non-specific background proteins that are consistently identified in AP-MS experiments; Table S2) (Mellacheruvu et al., 2013). In summary, our combined use of proximity labeling with wildtype vs. docking-defective BirA*-CN fusions and *in silico* identification of CN-binding SLiMs distinguishes candidate interactors from CN-proximal bystander proteins.

When analyzed for enriched cellular component GO Terms (Mi et al., 2013), CN-proximal proteins, i.e, either the 397 proteins identified with BirA*-CN_{WT} or the 196 docking-dependent proteins, were significantly enriched for multiple terms that are consistent with established regulatory functions for CN (Baumgartel and Mansuy, 2012; Chircop et al., 2010; Cousin and Robinson, 2001; Dong et al., 2016; Hoffman et al., 2017) (Figure 4C, Table S3). In addition, we observed enrichment for candidate interactors at cellular structures for which CN regulation is not known, in particular the centrosome and the nuclear pore complex (NPC).

CN shows proximity to centrosomal proteins

The centrosome, composed of two centrioles surrounded by pericentriolar material (PCM), is the major microtubule- organizing center in mammalian cells and centrioles are also required for cilia formation (Figure 4D). Components of centrosomes and cilia were manually curated in our set of 397 CN-proximal proteins, identifying 35 such proteins that were biotinylated by BirA*-CN_{WT} (8.8%), half of which (18) showed PxIxIT-dependent biotinylation (Figure 4E, Table S3). In particular, proteins that map to the distal end of the centriole (Azimzadeh et al., 2009; Singla et al., 2010; Tsang and Dynlacht, 2013) were highly represented in the BioID data, and were among the most strongly PxIxIT-dependent proximity interactions (CCP110, CEP97, CEP78, Talpid3/KIAA0586, OFD1 and POC5; Figure 4E, Table S3). These findings indicate that CN is proximal to the centrosome, and/or specific centriolar proteins. To further examine this possibility, the subcellular distribution of biotin specific to BirA*-CN_{WT} expression was visualized using fluorescence microscopy. 99% of cells expressing BirA*-CN_{WT} (n=276) displayed biotin labeling at the centrosome, compared to 0% of cells expressing BirA* alone (n=185) or without added biotin (Figure S5C, D). The biotin signal co-localized with centrosomal proteins γ-tubulin (Figures 4F) and centrin in both interphase and mitotic cells (Figures S5C and D). Thus, proximity labeling identified PxIxIT-dependent interactions of CN with centrosomes that were previously unknown.

CN dephosphorylates NPC basket proteins and regulates nuclear transport

Identification of a PxIxIT motif in Nup153 and enrichment of CN-proximal proteins at the NPC suggests that CN may regulate the structure and/or function of the NPC, which is without precedent in the current literature. The NPC is a highly conserved macromolecular structure

bioRxiv preprint doi: https://doi.org/10.1101/632547; this version posted May 9, 2019. The copyright holder for this preprint (which was not certified by peer review) is the author/funder. All rights reserved. No reuse allowed without permission.

comprised of multiple copies of ~30 unique proteins that serve structural roles and/or facilitate nucleocytoplasmic transport (Beck and Hurt, 2017). Nuclear transport proteins identified by our analyses as containing a CN-binding SLiM and/or showing proximity to CN in BioID (Figure 5A) include soluble nuclear transport factors (Ran, RanGap1, RanBP1, Importin-β), as well as several nucleoporin proteins (nups), most of which directly participate in nuclear transport. In particular, all three components of the NPC basket structure were identified: Nup153 contains an experimentally validated PxIxIT (Fig 1G) and shows SLiM-dependent proximity to CN *in vivo* (Figure 2B), whereas Nup50 and TPR both contain computationally predicted PxIxIT sites. To further investigate CN proximity to NPC components, biotinylated proteins were isolated from cells expressing BirA*-CN (WT or NIR) and probed specifically for the presence of nups via immunoblotting. These analyses revealed biotinylation of cytoplasmic filament nups (Nup358/RanBP2 and Nup214), a central channel FG nup (Nup62), and all 3 nuclear basket nups (Nup153, Nup50 and TPR) (Figure 5B). However, no biotinylation of Nup98 (a central FG nup) or PABPN1 (an abundant nuclear poly (A) binding protein) was observed, suggesting CN proximity to specific nucleoporin subcomplexes. Furthermore, significantly reduced biotinylation of Nup153, Nup62, and Nup50 with BirA*-CN_{NIR} suggests that one or more PxIxIT-dependent interactions target CN to the nuclear pore (Figure 5B).

Next, we tested for direct PxIxIT-dependent interaction of CN with the nuclear basket nups, Nup50 and Nup153 *in vitro*. Recombinant full-length Nup50 co-purified with GST-CN, but not GST alone, and this interaction was reduced upon mutation of the predicted PxIxIT in Nup50 (Figure 5C). Similarly, recombinant $Nup153_{228-611}$ showed co-purification with CN_{WT} that was reduced for CN_{NIR} (Figure 5D), and mutation of the PxIxIT in Nup153 reduced its interaction with CN. In addition, *in vitro* assays with peptides from TPR showed that CN interacts with a predicted PxIxIT-containing sequence in this protein (Figure S6A). Together, these findings demonstrate that PxIxIT motifs contribute to direct binding of CN to the nuclear basket structure of the NPC.

To investigate possible dephosphorylation of nuclear basket proteins by CN, appropriate phosphorylation conditions were first established. Phosphorylation of NPCs by CDKs that occurs during mitosis is reversed by PP1 and PP2A (Sales Gil et al., 2018). However, phosphatases that counteract ERK1/2, which phosphorylate NPC nuclear basket proteins to disrupt nucleocytoplasmic transport during oxidant stress, L-type viral infection, and in multiple cancer cell lines (Kodiha et al., 2009; Kosako et al., 2009; Porter et al., 2010; Stuart et al., 2015) remain to be identified. To investigate whether CN acts on ERK-phosphorylated nups, GST-$Nup153_{228-611}$ and full-length GST-Nup50 were phosphorylated with ERK2 and incubated with CN_{trunc}. We observed robust dephosphorylation of Nup153 and Nup50 (Figures 5 E and F) that was reduced to varying extents upon mutation of the PxIxIT motif in each protein (Figure S6B). Direct binding and dephosphorylation of these nups suggests that CN may promote transport of NLS-containing cargo through the nuclear pore by reversing ERK-mediated phosphorylation. To test this model, HeLa cells, which have active ERK1/2 signaling (data not shown), were transiently transfected with a GFP fusion protein containing the HIV Rev protein sequence, along with the hormone-binding domain of the glucocorticoid receptor (RGG), which translocates from cytoplasm to nucleus upon treatment with the receptor agonist, dexamethasone (Love et al., 1998). After addition of dexamethasone, live-cell imaging under control conditions (DMSO) or following pretreatment with a CN inhibitor (FK506 or CsA) showed that CN inhibition decreased both the rate and final extent of nuclear RGG accumulation (Figures 6A and B, Supplemental movie 1). Effects of FK506 and CsA, which inhibit CN through distinct mechanisms (Liu, 1993), were indistinguishable from each other. Together, these findings support the hypothesis that CN promotes nuclear accumulation of import cargo by dephosphorylating key NPC components.

bioRxiv preprint doi: https://doi.org/10.1101/632547; this version posted May 9, 2019. The copyright holder for this preprint (which was not certified by peer review) is the author/funder. All rights reserved. No reuse allowed without permission.

In *S. cerevisiae*, the orthologs of Nup153 and Nup50, Nups 1, 2 and 60 (Beck and Hurt, 2017), each contain predicted PxIxITs and, in the case of Nups 2 and 60, CN-dependent phosphorylation sites (Goldman et al., 2014). To investigate whether CN interaction with NPC components is conserved, we utilized yeast strains containing genomically tagged CN (*GFP-CNA1*) and overexpressing GST-Nup1, -2 or -60 (Zhu et al., 2001). As expected, GST-Elm1, an established CN substrate, but not GST alone co-purified with GFP-Cna1 from yeast extracts (Figure 6C). Co-purification of GFP-Cna1 with GST-Nup1, but not -Nup2 or -Nup60, was also observed. The Nup1-CN interaction was disrupted by a high-affinity PxIxIT peptide, PVIVIT (Aramburu et al., 1999), but not a scrambled version of this peptide (Figure 6C). Together, these findings suggest that PxIxIT-mediated binding of CN to nuclear basket nucleoporins is conserved.

During osmotic stress, yeast NPC nuclear basket proteins are phosphorylated by the Hog1 MAPK, and mutation of Hog1-dependent sites in Nup1 and Nup2 results in decreased expression of stress-responsive genes (Regot et al., 2013). To examine whether CN, which is also active during osmotic stress (Guiney et al., 2015), dephosphorylates yeast NPC nuclear basket proteins, recombinant Nup1, Nup2 and Nup60 were phosphorylated *in vitro* with activated Hog1 and then incubated with yeast CN_{trunc} and scrambled or PVIVIT peptides. We observed robust dephosphorylation of all 3 nups that was significantly inhibited by PVIVIT but not the scrambled peptide (Figure 6D), demonstrating a requirement for CN docking. These data suggest that Nup1, Nup2 and Nup60 contain functional PxIxIT motifs, although weaker affinity motifs in Nup2 and Nup60 may explain our failure to detect their co-purification with CN from extracts. Together, these analyses show that dephosphorylation of nuclear basket components of the NPC by CN is evolutionarily conserved.

This work is the first to report a role for CN at the NPC, although Ca^{2+}-dependent regulation of nucleocytoplasmic transport has been much debated (Sarma and Yang, 2011). Our findings suggest that local Ca^{2+} signals may directly control the activity of NPC proteins through CN-mediated dephosphorylation, and dramatically demonstrate the power of SLiM identification to discover unanticipated functions for Ca^{2+} and CN signaling.

Assembly and analysis of a SLiM-based CN interaction network

CN is ubiquitously expressed and modulates a range of tissue-specific processes that have not been systematically investigated. Therefore, we applied insights into CN-binding SLiMs gained in this work to assemble a high-confidence interaction network comprised of 486 unique proteins with experimental and/or *in silico* evidence of CN association (Figure 7A, Table S4). This network includes: proteins that contain a newly validated CN-binding SLiM, established substrates and interactors from the PRS, proteins from the PPI or PDB-MS data sets that contain putative SLiMs, docking dependent CN-proximal proteins (Bio-ID dataset) that contain a putative SLiM and proteins with one or more high-confidence CN binding motif identified *in silico* (Figure S7, Table S4). Motifs were designated as high-confidence if their PSSM score is greater than that of the lowest ranking experimentally validated motif. These 486 proteins define a network that is significantly enriched for protein-protein interactions (p-value $< 1.0 \times 10^{-16}$ (Szklarczyk et al., 2017)). This interaction network, which we termed the CNome, suggests that many more substrates and regulatory functions remain to be experimentally demonstrated for CN.

Functional analysis of the CNome revealed multiple enriched GO terms, as expected for the ubiquitous presence of CN and Ca^{2+}-dependent signaling machinery in humans (Figure 7B). These include terms related to phosphorylation, Ca^{2+}-dependent signaling, transcription, and the cytoskeleton, all of which expand on CN functions that are described in the published literature (Table S5). Extensive roles for CN in cardiac and synaptic signaling, where Ca^{2+} and CN-

bioRxiv preprint doi: https://doi.org/10.1101/632547; this version posted May 9, 2019. The copyright holder for this preprint (which was not certified by peer review) is the author/funder. All rights reserved. No reuse allowed without permission.

dependent regulation are prominent, are also indicated (see Discussion, Figures 7C and D). Enrichment of centrosomal and nuclear pore proteins in the CN interaction network is consistent with the PDB-MS and functional analyses presented here and demonstrate the power of systematic SLiM identification to discover sites of CN action. In total, this network serves as a resource for the Ca^{2+} signaling community that will fuel future investigations into Ca^{2+}/CN regulatory functions.

Discussion

In this work, we focus on SLiM discovery and use an effective combination of experimental and computational approaches to discover 45 novel CN-binding motifs and achieve surprising insights into signaling by the Ca^{2+}/calmodulin-regulated CN phosphatase.

Our approach to phosphatase substrate identification is fundamentally different from typical proteomic-based studies: Quantitative phosphoproteomics is often used to identify phosphorylation events that change upon perturbation of phosphatase activity, but many of these may be secondary rather than direct effects. Alternatively, affinity purification coupled to mass spectrometry (AP-MS) identifies phosphatase-interacting proteins, but fails to capture many low-affinity, SLiM-mediated associations (Gingras et al., 2018). In contrast, we leverage ProP-PD to discover CN docking sites with amino acid resolution on a proteome-wide scale, proximity-based labeling (PDB-MS) to uncover transient CN docking interactions, and *in silico* specificity determinant modeling to pinpoint candidate interactors as well as key sequences that can be mutated to examine CN-mediated regulatory events.

Although conserved recognition of PxIxIT and LxVP motifs by CN is well documented (Nygren and Scott, 2016; Roy and Cyert, 2009), challenges inherent to identifying these low affinity and degenerate sequences has limited their discovery. Here, we utilized ProP-PD to triple the number of validated CN-binding motifs in humans and establish a rich collection of PxIxITs and LxVPs that encompass diversity in sequence and binding strength. Furthermore, we documented the presence of combination LxVPxIxIT motifs in several proteins that exhibit both binding modes. Although the functional consequences of these combination SLiMs remain to be explored, simultaneous binding of both motifs to CN is unlikely, given the distance between LxVP and PxIxIT docking surfaces (Grigoriu et al., 2013). Instead, these SLiMs may mediate allovalent interactions where the presence of multiple pockets or motifs increases the probability of a re-binding event before the binding partners diffuse apart (Ivarsson and Jemth, 2018).

The newly uncovered PxIxIT and LxVP sequences described here identify unexpected CN-interacting proteins, including Notch1 and Nup153, which we show are directly dephosphorylated by CN. More importantly, this large collection of sequences was crucial for developing sensitive and robust statistical models (PSSMs) for systematic proteome-wide SLiM discovery. By encoding weighted information about each position of a motif, PSSMs offer significant advantages for motif identification over simple matching to a consensus sequence (Krystkowiak et al., 2018). Use of such regular expressions (RegEx) identifies only exact sequence matches and treats information at all motif positions equally. Limitations of this approach are illustrated by a previous effort to identify LxVP-containing proteins using a structure-based RegEx that fails to identify 16 of 25 LxVP-containing peptides discovered here via ProP-PD (Sheftic et al., 2016). Similarly, RegEx's used for PxIxIT identification exclude information from flanking residues, which significantly influence binding affinity (Nguyen et al., bioRxiv 306779) and are represented in the 12 position PSSM developed here. A limitation of querying phosphatase function via SLiM discovery is the failure to identify a physiological context and/or tissue for candidate dephosphorylation events. However, when used to analyze

bioRxiv preprint doi: https://doi.org/10.1101/632547; this version posted May 9, 2019. The copyright holder for this preprint (which was not certified by peer review) is the author/funder. All rights reserved. No reuse allowed without permission.

proteomic datasets, these tools provide a powerful method for substrate identification, as illustrated by our PDB-MS studies.

The ability of PDB-MS to reveal subcellular organization is highlighted by the unexpected identification of SLiM-dependent CN proximity to proteins at the centrosome. In particular, we observed PxIxIT-dependent biotinylation of proteins that map to the distal end of centrioles, including interacting partners CCP110 and CEP97: These proteins, which were selectively biotinylated by sub-set of BirA*-tagged centrosomal proteins in other studies (Firat-Karalar et al., 2014; Gupta et al., 2015), bind calmodulin and negatively regulate ciliogenesis (Spektor et al., 2007; Tsang et al., 2006). Previous reports of CN co-purification with Cep97 (Fogeron et al., 2013), and modulation of ciliary length by RCAN2, the CN regulator (Stevenson et al., 2018), further suggest a role for CN at centrosomes/cilia. Our attempts to detect CN enrichment at centrosomes have been unsuccessful (data not shown) and may indicate that CN-centrosome interactions are limited, transient, and/or temporally regulated. Investigations of Ca^{2+} signaling at centrosomes, which contain multiple Ca^{2+}- and/or calmodulin-binding proteins (Dantas et al., 2013; Galletta et al., 2014; Spektor et al., 2007; Tsang et al., 2006) and cilia, which constitute a distinct Ca^{2+} compartment (Delling et al., 2013; Delling et al., 2016), are ongoing. Our findings point to CN as a likely downstream effector of Ca^{2+} signals at these organelles.

The SLiM-based approaches described here also yielded unanticipated evidence that CN regulates nucleocytoplasmic transport and dephosphorylates NPC proteins. We show that CN positively regulates the rate and accumulation of one transport cargo, although further studies are required to determine how broadly CN affects nucleocytoplasmic transport. Furthermore, because CN activity is strictly controlled by the availability of Ca^{2+} and calmodulin (Mehta and Zhang, 2014), our findings support a model where these signaling molecules are locally regulated at NPCs. The existence of calmodulin-dependent transport pathways provides evidence of functional calmodulin pools at NPCs (Wagstaff and Jans, 2009). Similarly, NPCs may represent a discrete Ca^{2+} signaling domain, as the nuclear envelope stores and releases Ca^{2+} with dynamics that are distinct from cytosolic Ca^{2+} signals (Bengtson and Bading, 2012; Ljubojevic and Bers, 2015). Changes in $[Ca^{2+}]_{cyto}$ were shown to alter the structure of key transport nucleoporins (Mooren et al., 2004; Paulillo et al., 2006; Sakiyama et al., 2017; Stoffler et al., 1999), although investigations into Ca^{2+}-dependent regulation of nucleocytoplasmic transport have produced conflicting results (Greber and Gerace, 1995; Strubing and Clapham, 1999). Given recent advances in Ca^{2+} imaging, our findings argue that Ca^{2+} dynamics at NPCs should be re-examined. More broadly, our studies uncovered many potential CN substrates with functions that are currently unconnected to Ca^{2+} signaling, therefore providing rich new avenues for exploration of Ca^{2+}-regulated processes.

Collectively, our analyses yield a catalogue of candidate targets of CN-dependent signaling throughout the body. This is exemplified by processes in the excitable tissues, heart and brain, where roles of Ca^{2+} and CN signaling are well documented. CN signaling dramatically impacts heart development and function via regulation of NFAT, and is known to signal from cardiac Z discs, components of which are enriched in the CNome (Figure 7C) (Parra and Rothermel, 2017) (Chang et al., 2004; Wilkins and Molkentin, 2004). Moreover, proteins in the CNome align with the pleiotropic consequences of CN deletion in mouse cardiomyocytes (Maillet et al., 2010). CN-binding peptides were identified in key signaling, structural and contractile proteins that suggest possible explanations for defects in cardiac development, proliferation and contractility that were observed in CN KO mice, while the striking enrichment in the CNome of ion channels that regulate cardiac action potentials offers insight into causes of the arrhythmias observed in these animals. Similarly, CN is highly expressed in the brain, where it significantly impacts learning, memory and other aspects of behavior (Baumgartel and Mansuy, 2012; Lin et al., 2003; Suh et al., 2013). The CNome suggests expanded targets for

bioRxiv preprint doi: https://doi.org/10.1101/632547; this version posted May 9, 2019. The copyright holder for this preprint (which was not certified by peer review) is the author/funder. All rights reserved. No reuse allowed without permission.

CN both pre- and post-synaptically and points particularly to unexplored roles for CN in the pre-synaptic active zone, which coordinates neurotransmitter release (Figure 7D). Identified SLiMs in BSN, PCLO, RIMS1, and RIMS2 suggest that these proteins, whose phosphorylation decreases during exocytosis, are regulated directly by CN (Kohansal-Nodehi et al., 2016). In sum, the network presented here provides a road map for targeted elucidation of CN signaling pathways in the heart, brain and other tissues.

Another indication of undocumented CN signaling mechanisms comes from studies of patients chronically exposed to CN inhibitors (CNIs; FK506 and CsA), which have been used for immunosuppression therapy for >35 years. The CNome provides a critical resource for investigating the etiologies of adverse effects caused by CNIs, including hypertension, diabetes, seizures and a characteristic pain syndrome, which result from CN inhibition in non-immune tissues (Roy and Cyert, 2019). A case in point is CNI-induced hypertension, caused in part by hyperphosphorylation of a Na/Cl cotransporter (NCC/SLC12A3) in the kidney (Hoorn et al., 2011). Our studies identify possible CN-binding SLiMs in kinases that regulate NCC function (ASK3/MAP3K15, STK39/SPAK, and OXSR1/OSR; (Naguro et al., 2012)) and in NEDD4L, a ubiquitin ligase that regulates levels of another key target for hypertension, the ENaC Na^+ channel (Rizzo and Staub, 2015). Thus, by systematically identifying putative CN targets, the CNome may yield strategies to alleviate the major complications incurred during CNI-based immunosuppression. Similarly, this network provides clues to understanding how mutations in CNAα give rise to early onset epilepsy, a devastating neurological disorder that is associated with a rapidly growing set of mutations (Mizuguchi et al., 2018; Myers et al., 2017; Wang et al., 2017). Epilepsy genes in the CNome encode synaptic vesicle proteins (DNM1, SYNJ1), ion channels (GABRB2, SCNA1, CACNA1H), and protein modifiers (SIK1, UBA5, NEDD4L). Dysregulation of some or all of these proteins may contribute to seizures in individuals with impaired CN function.

In summary, the CN signaling network (CNome) established here provides a basis for future investigations of Ca^{2+}/CN signaling in normal and disease-associated physiology, including effects of prolonged immunosuppression. Moreover, our studies emphasize the importance of continuing to identify and characterize SLiMs, components of the dark proteome (Bitard-Feildel et al., 2018) that can unlock the mysteries of cell signaling. All major signaling pathways rely on SLiMs to form rapid, specific, and dynamic PPIs that transmit cellular information and our studies provide a blueprint for investigating any SLiM-based network using a combination of experimental and computational strategies.

Supplemental Information

Additional information is presented in supplemental figures (S1-S7), tables (S1-S5) and movies (S1).

Acknowledgements

We are indebted to all members of the Cyert lab, especially Idil Ulengin-Talkish for critical feedback on this work and manuscript. We thank Mark Dell'Acqua for helpful discussion, Jeremy Thorner and Francesc Posas for generous gifts of reagents, and the Skotheim lab for generous use of their cell culture facilities. MSC, JR, NPD and CPW were funded by NIH grants (R01 GM119336 to MSC, JR, and NPD, F32 GM120916 to CPW). NED and IK were funded by a Science Foundation Ireland Starting Investigator Research Grant 13/SIRG/2193; YI, VY and CB were funded by the Swedish research council (2016‐04965), the Carl Trygger Foundation (CTS14:209) and Lenannders Foundation. The support of ER by the Landesoffensive zur Entwicklung wissenschaftlich-ökonomischer Exzellenz (LOEWE), LOEWE-Zentrum Translationale Medizin und Pharmakologie, is gratefully acknowledged. ACG and CJW were

bioRxiv preprint doi: https://doi.org/10.1101/632547; this version posted May 9, 2019. The copyright holder for this preprint (which was not certified by peer review) is the author/funder. All rights reserved. No reuse allowed without permission.

funded the Canadian Institutes of Health Research (Foundation grant FDN143301) and the Governments of Canada and Ontario through Genome Canada, Ontario Genomics and the Ontario Research Fund (OGI-139 and RE08-065). ACG is the Canada Research Chair in Functional Proteomics. KU and DM were funded by 1R01GM131052. TS and JTW were funded by NIGMS (R35 GM130286 to TS; K99 GM131024 to JTW).

Author contributions

CPW and JR performed the majority of wet-lab experiments, supervised by MSC, with the exception of the following: VY and CB carried out the proteomic phage display screening, supervised by YI; ER performed the NGS analysis; CJW carried out BioID labeling, MS analyses and data processing, supervised by ACG; DM carried out live-cell imaging and data analyses of RGG accumulation, supervised by KU; JTW carried out imaging of biotin-labelled cells, and annotation of centrosomal proteins identified by BioID, supervised by TS. Bioinformatic analyses were carried out by NED, NPD and IK. CPW, JR, MSC and NED conceived and supervised the work and wrote the manuscript with input from all the authors.

Declaration of interests

The authors declare no competing interests.

Figure legends

Figure 1: *ProP-PD discovers CN-binding PxIxIT and LxVP sequences in humans*. **A**. Structure showing calcineurin (catalytic Aα (light grey) and regulatory B (dark grey) subunits, catalytic center (salmon)) complexed with the PxIxIT (orange) and LxVP (green) motifs from the viral inhibitor, A238L (PDB: 4F0Z). CN amino acids crucial for PxIxIT- (^{330}NIR^{332}: yellow) and LxVP (^{352}W,^{356}F: lime) docking are colored. **B**. Motif enrichment of the entire set of 214 Pro-PD peptides or 137 Pro-PD peptides that were enriched with CN_{WT} only, using SLIMFinder. Data shown for all peptides (most significant motif: L.VP; expected: 0.6; observed: 44; Sig: $<1^{e-16}$) and CN_{WT} - CN_{NIR} (3rd most significant motif: P.[FILV].[FILV]; expected: 2.95; observed: 28; Sig: 9.76^{e-10}). **C**. Motif distribution in 214 ProP-PD peptides isolated with CN. **D**. *In vitro* co-purification of GST-tagged LxVP-peptides with His-CN heterodimer. Means of 3 independent experiments, normalized to the binding of NFATC1-LxVP to CN, are shown with SEM. In all cases, p<0.01. Bar color: Known (black), novel (gray) LxVP motifs. **E**. Co-purification of GST-Nfatc1-LxVP peptide (FCEQY**LSVP**QASYQW) and GST-Notch1-LxVP peptides ($Notch1_{WT}$: NTPSHQ**L**Q**VP**EHPFLT or $Notch1_{MUT}$: NTPSHQ**A**Q**AA**EHPFLT) with His-CN holoenzyme (CN_{WT} or CN_{WF}). **F**. *In vitro* binding of GST-PxIxIT-peptides to His-CN as in D. Means of 3 independent experiments, normalized to the binding of NFATc1-PxIxIT to CN, are shown with SEM. In all cases, p<0.01. Bar color: Known (black), novel (gray) PxIxIT motifs. **G**. Co-purification of GST-NUP153-PxIxIT peptide ($NUP153_{WT}$: L**P**T**F**N**FS**SPEITTSSP or $NUP153_{MUT}$: L**A**T**A**NF**A**SPEITTSSP) with His-CN heterodimer (CN_{WT} or CN_{NIR}). **H**. *In vitro* co-purification of GST-tagged LxVPxIxIT-peptide from CACNA1H (WT or mutants as indicated) with His-CN heterodimer. Means of 3 independent experiments with SEM are shown. *: p<0.05, **: p<0.01.

Figure 2: *Newly discovered CN-SLiMs establish in vivo CN-interacting partners and identify Notch1 as a CN substrate*. **A**. GO process terms associated with 27/42 CN-SLiM containing proteins identified via Pro-PD are shown (SUPT20HL2 was removed due to inaccessibility to CN). Remaining proteins (15) are not represented as they define unique processes not shared with other ProPD-identified proteins. **B**. CN associates with NUP153 *in vivo* in a PxIxIT-dependent manner. HEK293T cells were co-transfected with myc-BirA*-CN (CN_{WT} or CN_{NIR})

bioRxiv preprint doi: https://doi.org/10.1101/632547; this version posted May 9, 2019. The copyright holder for this preprint (which was not certified by peer review) is the author/funder. All rights reserved. No reuse allowed without permission.

and FLAG-tagged NUP153 WT (^{485}**P**T**F**NF**S**^{490}) or PxIxIT$_{MUT}$ (^{485}**A**T**A**NF**A**^{490}). Biotinylated proteins were purified with streptavidin beads and probed with anti-FLAG antiserum. Binding was quantified as FLAG/Myc bound signal normalized to FLAG/Actin Input signal. Graph represents means for at least 3 independent experiments with SEM. **: p<0.01, ***: p<0.005. **C**. Schematic of Notch1 intracellular domain (NICD) protein structure. The sequence of WT and LxVP$_{MUT}$ are indicated. RAM: RBP-Jκ associated module, TAD: trans-activating domain, PEST: proline, glutamine, serine and threonine rich domain. Triangles and diamonds: positions of PEST domain mutations found in T-ALL patients. **D.** CN associates with NICD *in vivo* in an LxVP dependent manner. BioID as in B with myc-BirA*-CN (CN$_{WT}$ or CN$_{WF}$) and NICD (WT or LxVP$_{MUT}$). Graphs as in B, *: p<0.05. **E**. *In vivo* regulation of NICD phosphorylation by CN. Immunoblot analysis of HEK293 Flp-In T-REx cells stably expressing NICD-FLAG (WT and LxVP$_{MUT}$) under CN activating (HA-CN$_{trunc}$) or inhibitory conditions (FK506; 1 μM). **F**. *In vitro* regulation of NICD phosphorylation by CN. Flag NICD, WT (upper panel) or LxVP$_{MUT}$ (lower panel) were purified from stably expressing HEK293 Flp-In T-REx cells and treated *in vitro* with activated calcineurin (CN$_{trunc}$) or lambda phosphatase (λ) in the presence or absence of phosphatase inhibitors (PPI) as indicated.

Figure 3: *Computational prediction of CN-binding SLiMs in the human proteome*.
A, **B**. List of previously known (22) and newly established (45) PxIxIT (A) and LxVP (B) SLiMs with flanking residues. **C**. Position Specific Scoring Matrices (PSSMs) generated for PxIxIT and LxVP SLiMs. Each PSSM includes flanking amino acids, as indicated. **D**. Number of proteins from the human proteome predicted to contain CN SLiMs after filtering (see Fig. S4A). **E**, **F**. Frequency of SLiM-containing proteins discovered by 1,000 randomly shuffled PSSMs in sets of proteins enriched for CN interacting partners. PPI: 182 CN interacting proteins from public datasets. PRS: 104 manually curated CN substrates or direct interacting partners. Red diamond: number of proteins with newly discovered SLiMs. Green diamond: number of proteins with previously known SLiMs.

Figure 4: *BioID identifies candidate CN-interacting partners*. **A.** Schematic for BirA*-tagged constructs used for BioID with location of NIR and WF mutations in CNAα shown. **B**. Log$_2$ ratio of spectral counts of proteins biotinylated by CN$_{WT}$ or docking site mutants (CN$_{NIR}$ and CN$_{WF}$) in HEK293 Flp-In T-REx cells. Peptides were analyzed by data-dependent acquisition (DDA). Proteins containing PxIxIT (blue dots), LxVP (red dots) or both (green dots) SLiMs are indicated. **C**. Number of proteins in statistically enriched GO-cellular component categories for 397 CN-proximal proteins (Total) or 196 'SLiM-dependent' proteins (Log$_2$ WT/mutant > 0.5). **D**. Schematic of centrosome structure and associated regions. **E**. Centrosomal location for significant CN-proximal proteins as determined by BioID (Table S3). Bold: proteins with SLiM-dependent biotinylation. Underlined: proteins containing a high confidence LxVP or PxIxIT from PSSM analyses (Table S4). **F**. BirA*-CNAα signal co-localizes with centrosomes. HEK-293 Flp-In T-REx cells expressing BirA*-CNAα were incubated with biotin to allow for promiscuous biotinylation of proximal components. Centrosomes are marked by gamma-tubulin (green). Streptavidin (red) binds to proteins labeled by BirA*-CNAα. DAPI (blue) marks the nucleus. The region of interest is boxed in the merge. The image is a maximum projection of a confocal z-stack. Scale bar: 5 μm.

Figure 5: *CN interacts with nuclear pore proteins*. **A**. Schematic for proteins comprising the human nuclear pore. CN-proximal proteins (as determined in Fig. 4) are marked in red. **B**. BioID of nuclear pore proteins with BirA*-FLAG-CN. Biotinylated proteins were purified with streptavidin beads and analyzed by immunoblotting with mAb414 (recognizes RanBP2,

bioRxiv preprint doi: https://doi.org/10.1101/632547; this version posted May 9, 2019. The copyright holder for this preprint (which was not certified by peer review) is the author/funder. All rights reserved. No reuse allowed without permission.

NUP214, NUP153, NUP98 and NUP62), PABPN1, NUP50, and TPR antibodies. Binding was quantified as signal for protein of interest/FLAG in bound samples and normalized to levels of the protein of interest in input. Normalized biotinylation (quantified for four independent experiments in the bottom panel) is significantly reduced with CN_{NIR} vs. CN_{WT} for NUP153, NUP50 and NUP62. *: p<0.05, ****: p<0.001. **C**. NUP50 interacts with CN *in vitro*. Co-purification of His-NUP50 (WT or $PxIxIT_{mut}$) with GST-CN. * = non-specific background band. **D**. $NUP153_{(228-611)}$ interacts with CN *in vitro.* Co-purification of GST- $NUP153_{(228-611)}$ (WT or $PxIxIT_{mut}$) with His-CN_{WT} or CN_{NIR} (mut). PxIxIT peptide from NFAT2 (GST-NFAT2) is a positive control. **E, F.** NUP50 and $NUP153_{(228-611)}$ are CN substrates *in vitro*. Recombinant GST-NUP50 or $NUP153_{(228-611)}$ (WT or $PxIxIT_{mut}$) were phosphorylated *in vitro* with ERK2 and de-phosphorylated with constitutively active CN_{trunc}. Total phosphorylation (^{32}P incorporation) was analyzed at indicated times and normalized to total protein. Fraction of normalized phosphorylation retained is indicated below.

Figure 6: *CN regulates nuclear transport.* **A, B.** Nuclear accumulation of RGG reporter was assessed in HeLa cells treated with DMSO or CN inhibitors, FK506 or CsA (1 μM). A montage of frames from representative videos are shown in A. Nuclear-cytoplasmic ratio of GFP at times after dexamethasone addition is graphed in B. Data represent mean ± SEM for 146 (DMSO), 99 (FK506), or 81 (CsA) individual cells. Import rates calculated from the linear regression of measurements within the 7.5-30 minute window after dexamethasone (dashed lines) are indicated as the change in nuclear:cytoplasmic ratio of the pRGG reporter over time (ΔN:C/min) and are statistically significant from one another (p<0.0001) in each treatment group. **C.** CN interacts with the yeast nucleoporin NUP1 *in vivo*. Co-purification of GST-Nups with GFP-CNA1 from extracts of yeast strain JRY19 expressing GST-NUP1, -NUP2, -NUP60 or -Elm1 (positive control). PVIVIT, a high-affinity PxIxIT peptide or scrambled (control) added to disrupt PxIxIT-mediated interactions. * indicates full-length proteins. **D**. Yeast nuclear basket proteins are CN substrates *in vitro*. Recombinant GST-NUP1, -NUP2 and -NUP60 were phosphorylated *in vitro* with activated Hog1 and de-phosphorylated with constitutively active yeast CN_{trunc}. Total phosphorylation was analyzed at indicated times and normalized to total protein. Competitor peptide (PVIVIT) or scrambled (control) were included during dephosphorylation. Means of 3 independent experiments with SEM are shown. *: p<0.05, **: p<0.01.

Figure 7: *Functional analysis of SLiM-based CNome*. **A**. The 486 proteins comprising the CNome originate from 6 individual datasets (see Table S4). Validated = experimentally verified SLiMs (Figures 3A and B); PRS = positive reference set (Table S4); PPI = high-throughput protein-protein interactions (Table S4). Overlaps between Validated, PRS, PPI, and BioID datasets are not indicated in schematic (see Figure S7). **B**. For each significantly enriched GO-term category, the number of proteins identified in the CNome and previously defined in the PRS are indicated. **C**, **D**. The CNome suggests novel roles for CN in cardiomyocytes (C) and neurons (D; presynaptic axons, the active zone and post synaptic dendrites). Established CN targets (blue) and novel CN network proteins (mustard) are highlighted.

Figure S1: A. Flowchart for ProP-PD screen, motif enrichment and experimental validation of CN-Binding peptides. **B**. CN Sequence read counts for selected peptide-phage using wild-type or mutant calcineurin over 4 selection rounds are shown. Experiments were carried out in buffer containing $CaCl_2$ or EDTA as indicated. CN_{NIR} contains $^{330}NIR^{332}$-AAA mutations whereas CN_{WF} contains ^{352}W-A, ^{356}F-A mutations in CNAα. **C**. Distribution of read counts for the indicated peptide type between CN_{WT} and $CN_{NIR.}$ **D**. *In vitro* binding of purified His-tagged CN_{WT}, CN_{NIR} and CN_{WF} to GST-tagged LxVP peptide from Nfatc1or a high affinity PxIxIT peptide, PVIVIT

bioRxiv preprint doi: https://doi.org/10.1101/632547; this version posted May 9, 2019. The copyright holder for this preprint (which was not certified by peer review) is the author/funder. All rights reserved. No reuse allowed without permission.

(Aramburu et al., 1999). CN_{NIR} has reduced binding to PVIVIT but not to Nfatc1-LxVP whereas CN_{WF} has reduced binding to Nfatc1-LxVP but not to PVIVIT.

Figure S2: A. *In vitro* co-purification of GST-tagged LxVPIXIT-peptide from CACNA1H with purified wild-type (CN_{WT}) and mutant (CN_{NIR} and CN_{WF}) His-CN heterodimer. Graph represents mean with SEM for normalized binding to His-CN_{WT}. **B**. LxVP-peptides show greatly reduced binding to CN_{WF}. *In vitro* co-purification of LxVP peptides with purified His-CN_{WT} and His-CN_{WF}. Graph represents mean with SEM of two experiments. Binding to CN_{WF} is represented as a fraction of binding to CN_{WT}. **C**. PxIxIT-peptides show greatly reduced binding to CN_{NIR}. *In vitro* co-purification of PxIxIT peptides with purified His-CN_{WT} and His-CN_{NIR}. Graph represents mean with SEM of two experiments. Binding to CN_{NIR} is represented as a fraction of binding to $CN_{WT.}$

Figure S3: A. Steady state levels of Flag-NICD (WT or $LxVP_{mut}$) in stably expressing HEK293 Flp-In T-REx cells under calcineurin inhibiting (6 hr. 1 μM FK506 treatment vs. DMSO vehicle) or calcineurin activating (co-transfection of constitutively active HA-CN_{trunc} vs. pcDNA3 vector) conditions. LxVP mutation results in lower NICD levels. WT-NICD levels are enhanced with CN activation whereas $LxVP_{mut}$-NICD levels are unchanged. Graph represents mean with SEM of six experiments. **: $p<0.01$, n.s.: not significant.

Figure S4: A. Overview of computational prediction of CN binding SLiMs from the human proteome. **B, C.** Receiver operating characteristic (ROC) curves for leave-one-out cross-validation of PxIxIT (B) and LxVP (C) PSSMs. The blue line represents mean PSSM values whereas the red line represents those for a random sequence. Benchmarking parameters for each PSSM are depicted below the curves. **D**. Newly predicted CN-SLiMs in previously known CN regulated proteins (AMPH and MAP33K7) bind CN *in vitro*. Co-purification of GST-tagged wild-type CN-SLiMs or mutant versions as indicated, with purified His-CN_{WT}. PxIxIT-SLiM (PEISVT) from AMPH, but not a mutant version, co-purifies with CN. M3K7 contains an LxVPxIxIT combination SLiM, where mutations in either the LxV or IxIT parts, or both, reduce interaction with CN_{WT}.

Figure S5: A. Log_2 ratio of spectral counts of proteins biotinylated by CN_{WT} or docking site mutants (CN_{NIR} and CN_{WF}) in HEK293 Flp-In T-REx cells. Peptides were analyzed by sequential window acquisition of theoretical fragments (SWATH, data-independent acquisition). Proteins containing PxIxIT (blue dots), LxVP (red dots) or both (green dots) SLiMs are indicated. **B.** Frequency of SLiM containing proteins discovered for 1,000 randomly shuffled PSSMs in the set of 196 proteins that show CN docking-site dependent biotinylation. Red diamond: number of proteins with newly identified CN-SLiMs. Green diamond: number of proteins with previously known CN-SLiMs. **C, D.**: BirA*-CNA_{WT} signal co-localizes with centrosomes. HEK-293 Flp-In T-REx cells either at interphase (C) or undergoing mitosis (D), expressing BirA*-CNA_{WT} were incubated with biotin. Negative controls were processed in parallel: biotin-treated cells expressing BirA* alone, and untreated cells expressing BirA*-CNA_{WT}. Centrosomes are marked by centrin3 (green). Streptavidin (red) binds to proteins labeled by BirA*-CNAWT or BirA* alone. DAPI (blue) marks the nucleus. Images are maximum projections of confocal z-stacks. Scale bars: 5 μm. Lower panels are the same images with enhanced streptavidin signal.

Figure S6: A. One of two newly predicted PxIxIT-SLiMs from the nuclear basket protein TPR binds CN *in vitro*. Co-purification of GST-tagged PxIxIT peptides with purified His-CN_{WT} or His-CN_{NIR}. Co-purification is PxIxIT dependent and diminished with CN_{NIR}. **B.** CN de-phosphorylates ERK sites on NUP50 and NUP153. GST-tagged full length NUP50 or a fragment of NUP153

bioRxiv preprint doi: https://doi.org/10.1101/632547; this version posted May 9, 2019. The copyright holder for this preprint (which was not certified by peer review) is the author/funder. All rights reserved. No reuse allowed without permission.

(a.a. 228-611) were phosphorylated with purified ERK2 and $^{32\text{-}P}\gamma$ATP and subsequently de-phosphorylated with constitutively active CN_{trunc}. Total phosphorylation was analyzed at times after CN addition and normalized to protein amount. In both cases, mutations in the PxIxIT-SLiM reproducibly affected the extent of CN de-phosphorylation, though the reduction was more significant for NUP153. Graph represents mean (with SEM) for 3 different experiments.

Figure S7: A. The intersection of proteins identified from individual datasets that comprise the CNome. Colors are consistent with datasets highlighted in Figure 7A. Valid. = validated SLiM-containing proteins, PRS = positive reference set, PPI = high throughput protein-protein interactors, PSSM = proteins with an *in silico* predicted CN-SLiM, BioID = docking dependent CN-proximal proteins, H.C. = high confidence.

Methods

Purification of Calcineurin:

For proteomic peptide phage display, GST tagged human calcineurin A (α isoform, truncated at residue 400), either wild-type or mutants ^{330}NIR^{332}-AAA and ^{352}W-A,^{356}F-A were expressed in tandem with the calcineurin B subunit in *E. coli* BL21 (DE3) cells (Invitrogen) and cultures in LB medium containing carbenicillin (50 μg/ml) at 37°C to mid-log phase. Expression was induced with 1 mM isopropyl 1-thio-β-D-galactosidase (IPTG) at 16°C for 18 hours. Cells were pelleted, washed and frozen at -80°C for at least 12 hours. Thawed cell pellets were re-suspended in lysis buffer (50 mM Tris-HCl pH 8, 2 mM EDTA, 2mM EGTA, 150 mM NaCl, 1mM dithiothreitol (DTT), protease inhibitors) and lysed by sonication using four, 1-minute pulses at 40% output. NaCl added to 1.50M and extracts were clarified using two rounds of centrifugation (20,000 X g, 20 min). Tween-20 was added to 0.1% and extracts were bound to 1 ml of glutathione-sepharose beads (Fisher Scientific, USA) for 2-4 hr. at 4°C, in batch. Bound beads were loaded onto a column and washed with 10 column volumes of wash buffer (100 mM Tris-HCl pH 8.0, 100 mM KOAc, 2 mM MgOAc, 0.005% Tween-20, 1 mM DTT) followed by one column volume of wash buffer with 1 mM ATP and then eluted in wash buffer containing 40 mM glutathione, pH 8.0 and 5mM DTT. Purified calcineurin heterodimer were dialysed in buffer (50 mM Tris-HCl pH 7.5, 150 mM NaCl, 1 mM DTT) and stored in 10-15% glycerol at -80°C.

For *in vitro* peptide binding assays, N-terminally, 6-His-tagged human calcineurin A (α isoform, truncated at residue 400), either wild-type or mutants ^{330}NIR^{332}-AAA and ^{352}W-A, ^{356}F-A were expressed in tandem with the calcineurin B subunit in *E. coli* BL21 (DE3) cells (Invitrogen, USA) and cultured in LB medium containing carbenicillin (50 μg/ml) at 37°C to mid-log phase. Expression was induced with 1 mM IPTG at 16°C for 18 hours. Cells were pelleted, washed and frozen at -80°C for at least 12 hours. Thawed cell pellets were re-suspended in lysis buffer (50 mM Tris-HCl pH 7.5, 150 mM NaCl, 0.1% Tween 20, 1mM β-mercaptoethanol, protease inhibitors) and lysed by sonication using four, 1-minute pulses at 40% output. Extracts were clarified using two rounds of centrifugation (20,000 X g, 20 min) and then bound to 1 ml of Ni-NTA agarose beads (Invitrogen) in lysis buffer containing 5mM imidazole for 2-4 hr. at 4°C, in batch. Bound beads were loaded onto a column and washed with lysis buffer containing 20mM imidazole and eluted with lysis buffer containing 300 mM imidazole, pH 7.5. Purified calcineurin heterodimer were dialysed in buffer (50 mM Tris-HCl pH 7.5, 150 mM NaCl, 1 mM β-mercaptoethanol) and stored in 10-15% glycerol at -80°C.

Proteomic peptide phage display (ProP-PD):

Wild-type CN and mutants thereof (CN_{NIR} and CN_{WF}) were used as bait proteins in selections against a recently described M13 phage library that displays sixteen amino acids

bioRxiv preprint doi: https://doi.org/10.1101/632547; this version posted May 9, 2019. The copyright holder for this preprint (which was not certified by peer review) is the author/funder. All rights reserved. No reuse allowed without permission.

peptides tiling intrinsically disordered regions of the human proteome on the major coat protein p8 (Davey et al., 2017) Selections were performed following the published protocol (Davey et al., 2017) with slight modifications. In an attempt to assess the calcium dependence of the interactions, selections were performed in parallel using either 2 mM EDTA or 2 mM $CaCl_2$ during incubation of phages with bait proteins and during all washing steps. For phage selections, 20 µg proteins (GST, CN_{WT}, CN_{NIR} and CN_{WF}) in 100 µl TBS (20 mM Tris-HCl, 150 mM NaCl, pH 7.4) were immobilized in a Maxisorp plate (Nunc, Roskilde, Denmark) overnight at 4°C. Wells were thereafter blocked with 0.5% (w/v) bovine serum albumin (BSA) in TBS (1h, 4°C). Before each round of selection, the phage library (~10^{12} phage virions/100 µl TBT buffer (TBS + 0.05% (v/v) Tween20 + 0.5% (w/v) BSA)) was subjected to a pre-selection toward immobilized GST to remove non-specific binders (1 h, 4°C). The phage library was then transferred to target wells and the phages were allowed to bind for 2 h at 4°C. Target wells were washed five times with cold wash buffer (TBS, 0.5% v/v Tween-20) and retained phages were eluted with log phase (OD_{600} = 0.8) *E. coli* Omnimax in 2xYT (10 g yeast extract, 16 g tryptone, 5 g NaCl to 1 l H_20) by incubating for 30 min at 37°C with shaking. After incubation, M13KO7 (NEB, Ipswich, MA, USA) helper phages (1x10^{11} p.f.u./ml) were added to enable phage production and the cells were grown for 45 min at 37°C. To amplify phages, eluted phages were grown over night at 37°C in 10 ml 2xYT containing 100 µg/ml carbenicillin, 30 µg/ml kanamycin, and 0.3 mM IPTG. To determine the number of phages recovered from the selection rounds, dilution series of the infected bacteria were deposited on 2xYT plates containing 100 µg/ml of carbenicillin.

Bacteria were pelleted by centrifugation (4,000 X g, 10 min). Phages were harvested by addition of 2.5 ml ice-cold PEG/NaCl solution (20% w/v PEG 8000 + 2.5 M NaCl) to the supernatant, followed by incubation on ice for 10 min and centrifugation at 10,000 X g for 20 min. Phage pellets were re-suspended in 1 ml TBS and used for the next round of selections. After four rounds of selection, phage pools for each selection round were subjected to enzyme-linked immunosorbent assays as described elsewhere (Huang and Sidhu, 2011).

Enriched phage pools were barcoded for next-generation sequencing. Undiluted amplified phage pools (5 µl) were used as templates for 24 cycles 50 µl PCR reactions using a distinct set of barcoded primers (0.5 µM each primer) for each reaction and Phusion High Fidelity DNA polymerase (NEB) with a maximum polymerase concentration. PCR reactions were supplemented with Gel Loading Dye Purple (6x) (New England Biolabs) and separated on a 2.5 % low melt agarose (BioRad) gel stained with Roti-Safe GelStain (Carl-Roth). The DNA was visualized by UV light. The PCR products were cut out and extracted using the QIAquick Gel Extraction Kit (Qiagen) according to the manufacturer with the following exceptions: a) Gel extracts were resolved at room temperature; b) DNA was eluted with 30 µL low Tris-EDTA (TE) buffer (Life Technologies). Molarities of the eluted library DNA were determined on the 2100 Bioanalyzer using the High Sensitivity DNA Kit (Agilent). Template preparation was performed according to the manufacturer's instruction using the Ion PGM Template OT2 200 Kit on the Ion OneTouch 2 System (Thermo Fisher Scientific). 25 µL of 5 pM library DNA (1.25*10^{-4} pmol) were used in the template reaction. Sequencing was conducted on the Ion Torrent PGM sequencer using the Ion PGM Sequencing 200 Kit v2 and the Ion 314 Chip v2 (Thermo Fisher Scientific) according to the manuals. Signal processing and base calling were done using the Torrent Suite Software (Thermo Fisher Scientific). Reads were exported as FASTQ files for downstream processing.

In vitro peptide binding assays:

bioRxiv preprint doi: https://doi.org/10.1101/632547; this version posted May 9, 2019. The copyright holder for this preprint (which was not certified by peer review) is the author/funder. All rights reserved. No reuse allowed without permission.

Peptides were fused to GST in vector pGX4T-3 and expressed in *E. coli* BL21 (DE3) (Invitrogen). Cells were grown at 37°C to mid-log phase and induced with 1 mM IPTG for 2 hr. Cell lysates were prepared using the EasyLyse™ bacterial protein extract solution (Lucigen Corp. USA) or the CelLytic B reagent (Sigma, USA) according to the manufacturers' protocol and were stored at -80°C. 1-2 μg His-tagged calcineurin was first bound to Ni-NTA-agarose or magnetic Dynabeads (Thermo Fisher Sci. USA) in base buffer (50 mM Tris-HCl pH 7.5, 150 mM NaCl, 0.1% Tween 20, 1mM β-mercaptoethanol, protease inhibitors, 5-10 mM imidazole, 1 mg/ml BSA) for 1 hr at 4°C. 50-100 μg of bacterial cell lysate containing GST-peptide was then added to the binding reaction and incubated further for 2-3 hr. 3% of the reaction mix was removed as 'input' prior to the incubation, boiled in 2XSDS buffer and stored for downstream analysis. The beads were washed in base buffer containing 15-20 mM imidazole. Bound proteins were then extracted with 2X-SDS loading buffer by boiling for 5 min. The proteins were analyzed by SDS-PAGE and immunoblotting with anti-GST (BioLegend MMS-112P) and anti-His (Qiagen 34660) antibodies. Blots were imaged with the Li-Cor Odyssey imaging system. GST proteins co-purifying with HIS-CN were normalized to their respective input and calcineurin pulled down.

Candidate-based BioID Analyses:

HEK293T cells were co-transfected with "bait" (Myc-BirA*-CN constructs) and "prey" (FLAG-tagged candidate substrates) using calcium phosphate transfection. Media was changed 16 hours after transfection. 24 hours after transfection, cells were treated with fresh media containing 50 μM D-biotin (Sigma B-4501). After 24 hours of labeling, cells were collected and snap frozen in liquid nitrogen. Cells were lysed in RIPA-2 buffer (150 mM NaCl, 1% NP40, 0.5% Deoxycholate, 0.1% SDS, 50 mM Tris 8.0) on ice for 20 minutes and spun for 20 minutes at 13,000 RPM at 4°C. For each binding reaction, 2 mg of clarified lysate was incubated with 40 μL of rinsed streptavidin beads (Sigma 11641786001) overnight at 4°C. Beads were rinsed and rotated 3 x 10 minutes in RIPA-2 buffer and eluted in 2X sample buffer (12% SDS, 0.06% Bromophenol blue, 60% glycerol, 375 mM Tris-HCl pH 6.8, 0.6M DTT). Input (40 μg) and bound (50% of total binding) samples were resolved by SDS-PAGE and immunoblotted with FLAG (1:2,000; Sigma F1804), Myc (1:3,000; Cell Signaling 2276S), and β-Actin (1:3,000; Li-Cor Biosciences 926-42210) antibodies. Binding was quantified as FLAG/Myc bound signal normalized to FLAG/Actin Input signal.

To detect labeling of endogenous nuclear pore proteins, HEK293 Flp-In T-Rex cells expressing BirA*-FLAG-CN constructs were induced with 1 μg/mL doxycycline. After 24 hours of induction, cells were treated with 50 μM biotin for 24 hours. Cells were collected and processed as described above and immunoblotted with mAb414 (1:1,000; Abcam ab24609), TPR (1:1,000; Santa Cruz Biotechnology sc-271565), Nup50 (1:1,000; Santa Cruz Biotechnology sc-398993), and PABPN1 (1:3,000; Abcam ab75855) antibodies. Binding was quantified as signal for protein of interest/FLAG in bound samples and normalized to levels of the protein of interest in input.

In vivo dephosphorylation of Notch1 intracellular domain (NICD):

HEK293 Flp-In T-REx cells expressing WT or $LxVP_{MUT}$ ($_{2502}LQVP_{2505}$ ➔ AQAA) NICD-FLAG constructs were transfected with pcDNA3 (vector alone) or HA-tagged CN_{trunc} and induced with 1 μg/mL doxycycline. Media was changed and refreshed with doxycycline 24 hours after transfection. The following day, cells were treated with DMSO or FK506 (1 μM) for 6 hours and then harvested. Cells were lysed with RIPA-2 buffer and run out on 7.5% SDS-PAGE gels followed by rapid transfer on iBlot2 (Thermo Fisher). Changes in electrophoretic mobility were assessed via immunoblotting with FLAG (Sigma F3165), HA (Sigma H3663), and Actin (LiCor

bioRxiv preprint doi: https://doi.org/10.1101/632547; this version posted May 9, 2019. The copyright holder for this preprint (which was not certified by peer review) is the author/funder. All rights reserved. No reuse allowed without permission.

926-42210) antibodies. NICD-FLAG steady-state levels were quantified using ImageStudio imaging software and normalized as FLAG/Actin.

In vitro dephosphorylation of NICD:

HEK293 Flp-In T-REx cells expressing WT or $LxVP_{MUT}$ ($_{2502}LQVP_{2505}$ ➔ AQAA) NICD-FLAG constructs were grown in 10-cm dishes and induced with 1 µg/mL doxycycline and collected after 48 hours. Pellets were re-suspended in lysis buffer (50 mM Tris-HCL pH 7.5, 150 mM NaCl, 1% NP-40, 1mM DTT and protease inhibitors) supplemented with phosphatase inhibitors (5 mM NaF, 0.4 mM sodium orthovanadate, 0.1 mM β-glycerophosphate, 5 mM EDTA) by gently vortexing followed by fine-needle aspiration and then incubated on ice for 20 minutes. Lysates were prepared by centrifugation at 15,000g for 20 minutes and removing the supernatant. Total protein concentration was calculated with a BCA protein assay kit (Thermo-Fisher, USA). Approximately 750 µg of total protein lysate per pull-down was bound to 50 µl of Flag-M2 magnetic beads (Sigma-Aldrich, USA) in binding buffer (lysis buffer but with 1%-NP-40) at 4°C for 2 hr. on an end-over-end rotator. Flag-tagged proteins were pelleted at 2K for 2 min., washed 2X in binding buffer and then once in binding buffer lacking phosphatase inhibitors. The beads were then washed with λ-phosphatase PMP buffer (1X PMP buffer, 1mM $MnCl_2$, protease inhibitors), PMP buffer with phosphatase inhibitors (described above), calcineurin buffer (50 mM Tris-HCl, pH 7.5, 100 mM NaCl, 6 mM $MgCl_2$, 0.5 mM $CaCl_2$) or calcineurin buffer with phosphatase inhibitors, as required. 0.25 µl λ-phosphatase or 100 nM activated calcineurin was then added to the reactions followed by incubation at 30°C for 45 min. Reactions were stopped with 2X SDS dye and boiled for 5 min. Proteins were analyzed on 5-5.5 % SDS-PAGE gels followed by Western blotting with the anti-Flag M2 antibody (Sigma-Aldrich, USA).

PSSM Analyses:

Dataset construction: A set of experimentally characterized *CN-binding motifs* (CN-BM) for the PxIxIT- and LxVP-binding pockets was curated from (i) the newly validated peptides from the current study and (ii) the previously validated peptides from the CN literature (Table S2). A peptide from NFX1, that was discovered by the ProP-PD screen and validated as binding to the LxVP-pocket (Table S1), was also included as an LxVP motif. The CN-BM dataset contained 33 PxIxIT and 34 LxVP motifs. A background set of *unvalidated consensus matches* (CN-UCM) of PxIxIT- and LxVP-like peptides was constructed by searching the CN-binding PxIxIT- and LxVP motif consensuses (PxIxIT - P[^PG][ILVF][^PG][ILVF][^PG] and LxVP - Lx[VLI]P) against the human UniProt reviewed proteins and removing validated *CN-binding motifs*. The CN-UCM set will consist almost exclusively of peptides that cannot bind to CN but resemble the motifs specificity determinants of the CN motif-binding pocket. The CN-UCM peptide dataset contained 21,791 PxIxIT and 13,014 LxVP consensus matches (Table S2).

PSSM construction: Validated CN-binding peptides from the CN-BM set were trimmed, based on position-specific enrichment of amino acids, or physicochemical groupings of amino acids, as described for the consensus representation in the PSSMSearch tool, to create peptide alignments with the consensus xxxP[^PG][ILVF][^PG][ILVF][^PG]xxx for PxIxIT-motifs and xxLx[VLI]Px for the LxVP-motifs (Table S2). A position-specific scoring matrix (PSSM) was constructed from each alignment using the PSI BLAST IC scoring scheme of the PSSMSearch PSSM construction tool (Altschul et al., 1997; Krystkowiak et al., 2018) (Table S2).

Discriminatory Attribute Benchmarking: The ability of a range of motif attributes to correctly differentiate *binding* from *background* peptides was tested by analyzing the CN-BM and CN-UCM peptide sets. The classes of motif attributes tested were (i) intrinsic disorder propensity using IUPred and FELLS (Dosztanyi et al., 2005; Piovesan et al., 2017), (ii) disorder-to-order transition upon binding propensity using Anchor (Dosztanyi et al., 2009), (iii) secondary structure

bioRxiv preprint doi: https://doi.org/10.1101/632547; this version posted May 9, 2019. The copyright holder for this preprint (which was not certified by peer review) is the author/funder. All rights reserved. No reuse allowed without permission.

propensity using FELLS (helix and extended) and Hydrophobic Cluster Analysis (Piovesan et al., 2017), (iv) conservation using taxonomic range and relative local conservation probability on metazoan alignments (Davey et al., 2012; Krystkowiak and Davey, 2017) and (v) shared molecular function, localization and biological process ontology terms with CN (Krystkowiak and Davey, 2017). The discriminatory ability of the attributes were measured as (i) the AUC (*Area Under The Curve*) of a ROC (*Receiver Operating Characteristics*) curve to determine if the attributes are capable of distinguishing between *binding* and *background* peptides and (ii) Mann–Whitney U test p-values to determine whether the attribute values for the *binding* and *background* peptides were from the same distribution (Table S2). The ability of the PSSM to discriminate *binding* from *background* peptides was tested differently using *leave-one-out* cross-validation as the PSSM is built using the *binding* peptides. Each peptide in the CN-BM set was removed from the alignment for PSSM construction, the resulting PSSM was used to score the removed peptide and the rank/significance of the removed peptide was calculated (Table S2).
Peptide Filtering: The benchmarking analysis identified the PSSM score and accessibility as key discriminatory attributes. Therefore the consensus matches were filtered using the PSSM score *p-value* with a cut-off of 0.0001, localization based on intracellular localization GO terms, and accessibility based on: (i) overlap with a resolved region in a structure from PDB, (ii) intrinsic disorder predictions (retaining only peptides found in disordered regions as defined by an IUPred score ≥0.3 (Dosztanyi et al., 2005) and (iii) UniProt annotation of topologically inaccessible regions (e.g. transmembrane and extracellular regions) (UniProt, 2015). Applying these simple filtering criteria, we retained 409 putative PxIxIT motifs and 410 putative LxVP motifs in the human proteome (Table S2). The predictive power of each discriminatory attribute was recalculated as described in the benchmarking section after filtering was applied showing that no further filtering steps were available to improve confidence in the returned peptides (Table S2). However, relative local conservation probability remained significant in the Mann–Whitney U tests and can be used along with PSSM scores to rank peptides by confidence. This is intuitive as it suggests that peptides that are more conserved and more similar to validated peptides are more likely to be binders.
CN interactor enrichment: Distinct CN interaction datasets were created from several sources - the HIPPIE database, the HIPPIE database filtered by high-throughput methods, BioID data from the PDB-MS study (significant and non-significant), the BioID CRAPome, MAPK docking site-containing proteins and a manually curated set of interactors created for this project (PRS) (Table S4). The enrichment of predicted CN-binding motifs in each interaction dataset was quantified using a randomized PSSM approach. Each PSSM was shuffled 1000 times, the shuffled PSSMs were searched against the human proteome, and the returned peptides were scored and filtered as described above. The number of CN interactors was calculated for each "shuffled" dataset. The distribution of interactor counts for the 1000 shuffled PSSM peptide sets was then used to quantify the likelihood of the observed number of interactors with predicted CN-binding peptide-containing proteins (Table S2).
Web resource: Variants of the PSSMSearch tool, to analyses proteomes for regions with significant similarity to a specificity determinant model (Krystkowiak and Davey, 2017), and the ProViz tool, to investigate the functional and evolutionary features of a protein (Jehl et al., 2016), allowing PxIxIT and LxVP searches to be performed on the proteome and protein level are available at http://slim.ucd.ie/motifs/calcineurin/.

BioID/MS Analyses:
Cell line generation: BirA*-FLAG constructs were generated via Gateway cloning into pDEST 5' BirA*-FLAG pcDNA5 FRT TO. Stable cell lines were generated in HEK293 Flp-In T-REx cell pools as (https://doi.org/10.1016/j.ymeth.2012.06.002). Expression was induced with

bioRxiv preprint doi: https://doi.org/10.1101/632547; this version posted May 9, 2019. The copyright holder for this preprint (which was not certified by peer review) is the author/funder. All rights reserved. No reuse allowed without permission.

tetracycline (1µg/ml) for 24 hrs when cells reached 80% confluency on a 150mm plate in selection media. For BioID experiments, cells were treated with 50µM biotin alongside tetracycline induction for 24hrs.

Streptavidin affinity purification and data acquisition: Cell pellets were resuspended in a 1:4 ratio of pellet weight to radio-immunoprecipitation assay (RIPA) buffer [50 mM Tris-HCL (pH 7.5), 150 mM NaCl, 1% NP-40, 1 mM EGTA, 4.5 mM $MgCl_2$ and 0.4% SDS), supplemented with 250U/ml of benzonase and 1x Sigma protease inhibitors P8340. Cells were lysed in one freeze-thaw cycle (frozen on dry ice for 5 min, then transferred to 37°C water bath until a small amount of ice remained). The sample was gently agitated on a nutator at 4°C for 30 min and then centrifuged at 16,000g for 20 min at 4°C. The supernatant was transferred to 1.5 ml microcentrifuge tubes, and a 25 µl volume of 60% streptavidin-sepharose bead slurry (GE Healthcare, catalog no. 17-5113-01) was added. Prior to addition of beads to supernatant, the beads were washed three times with RIPA buffer and resuspended in RIPA buffer to make a 60% slurry. Affinity purification was performed at 4°C on a nutator overnight, beads were then washed once with 2% SDS buffer (500 µl of 2%SDS, 50 mM Tris pH 7.5), twice with 500 µl of RIPA buffer and three times with 50 mM ammonium bicarbonate pH 8.0 (ABC). After removal of the last wash, the beads were resuspended in 100 µl of 50 mM ABC (pH 8.0) with 1 µg of trypsin (Sigma-Aldrich, T6567) and rotated on a nutator at 37°C for 4hrs. After 4 hr., an additional 1 µg of trypsin was added to each sample (in 2 µl of 50 mM ABC) and rotated on a nutator at 37°C overnight. Beads were pelleted (500 g, 1 min) and the supernatant (pooled peptides) was transferred to a new 1.5-ml microcentrifuge tube. Beads were rinsed with 100 µl of MS-grade H_2O and combined with the pooled peptides. 50 µl of 10% formic acid was added to the supernatant for a final concentration of 2% formic acid. The pooled supernatant was centrifuged at 16,000g for 5 min to pellet remaining beads. 230 µl of the pooled supernatant was transferred to a new 1.5-ml microcentrifuge tube. Samples were dried using a vacuum concentrator. Tryptic peptides were resuspended in 10 µl of 5% formic acid, 2.5 µl was used for each analysis.

Peptides were analyzed by nano-HPLC (high-pressure liquid chromatography) coupled to MS. Nano-spray emitters were generated from fused silica capillary tubing (100µm internal diameter, 365 µm outer diameter) using a laser puller (Sutter Instrument Co., model P-2000, heat = 280, FIL = 0, VEL = 18, DEL = 2000). Nano-spray emitters were packed with C18 reversed-phase material (Reprosil-Pur 120 C18-AQ, 3 µm) in methanol using a pressure injection cell. 5ul of sample (2.5 µl of each sample with 3.5 µl of 5% formic acid) was directly loaded at 800 nl/min for 20 min. onto a 100 µm x15 cm nano-spray emitter. Peptides were eluted from the column with an acetonitrile gradient generated by an Eksigent ekspert™ nanoLC 425, and analyzed on a TripleTOF™6600 instrument (AB SCIEX, Concord, Ontario, Canada). The gradient was delivered at 400 nl/min from 2% acetonitrile with 0.1% formic acid to 35% acetonitrile with 0.1% formic acid using a linear gradient of 90 min. This was followed by a 15min wash with 80% acetonitrile with 0.1% formic acid and equilibration for another 15min to 2% acetonitrile with 0.1% formic acid, resulting in a total of 120min for the DDA (data-dependent acquisition) protocol.

The first MS1 scan had an accumulation time of 250 ms within a mass range of 400-1800Da. This was followed by 10 MS/MS scans of the top 10 peptides identified in the first DDA scan, with an accumulation time of 100ms for each MS/MS scan. Each candidate ion was required to have a charge state from 2-5 and a minimum threshold of 300 counts per second, isolated using a window of 50mDa. Previously analyzed candidate ions were dynamically excluded for 7 seconds. The DIA (data-independent acquisition; SWATH) protocol used the same gradient and nanoLC protocol as the DDA method. The MS1 scan had an accumulation time of 250ms within a mass range of 400-1800Da, followed by MS/MS scans split into 54 scan

bioRxiv preprint doi: https://doi.org/10.1101/632547; this version posted May 9, 2019. The copyright holder for this preprint (which was not certified by peer review) is the author/funder. All rights reserved. No reuse allowed without permission.

windows across the mass range of 400-1250Da. In each MS/MS scan window, the accumulation time was 65ms per MS/MS scan.

Both DDA and SWATH datasets has been deposited as a complete submission to the MassIVE repository (https://massive.ucsd.edu/ProteoSAFe/static/massive.jsp). The DDA data has been assigned the accession number MSV000083695. The ProteomeXchange accession is PXD013527. The dataset is currently available for reviewers at ftp://MSV000083695@massive.ucsd.edu. Please login with username MSV000083695_reviewer; password: Calcineurin2019. The SWATH data has been assigned the accession number MSV000083697. The ProteomeXchange accession is PXD013529. The dataset is currently available for reviewers at ftp://MSV000083697@massive.ucsd.edu. Please login with username MSV000083697_reviewer; password: CalcineurinS2019. Both datasets will be made public upon acceptance of the manuscript.

MS data analysis: Mass spectrometry data generated were stored, searched and analyzed using ProHits laboratory information management system (LIMS) platform (Liu et al., 2016). Within ProHits, WIFF files were converted to an MGF format using the WIFF2MGF converter and to a mzML format using ProteoWizard (V3.0.10702) and the AB SCIEX MS Data Converter (V1.3 beta). For DDA, the data was then searched using Mascot (V2.3.02) (Perkins et al., 1999) and Comet (V2016.01 rev.2) (Eng et al., 2013). The spectra were searched with the human and adenovirus sequences in the RefSeq database (version 57, January 30th, 2013) acquired from NCBI, supplemented with “common contaminants” from the Max Planck Institute (http://maxquant.org/contaminants.zip) and the Global Proteome Machine (GPM; ftp://ftp.thegpm.org/fasta/cRAP/crap.fasta), forward and reverse sequences (labeled “gi|9999” or “DECOY”), sequence tags (BirA, GST26, mCherry and GFP) and streptavidin, for a total of 72,481 entries. Database parameters were set to search for tryptic cleavages, allowing up to 2 missed cleavages sites per peptide with a mass tolerance of 35 ppm for precursors with charges of 2+ to 4+ and a tolerance of 0.15amu for fragment ions. Variable modifications were selected for deamidated asparagine and glutamine and oxidized methionine. Results from each search engine were analyzed through TPP (the Trans-Proteomic Pipeline, v.4.7 POLAR VORTEX rev 1) via the iProphet pipeline (Shteynberg et al., 2011).

For DIA, MSPLIT-DIA v1.0 (Wang et al., 2015) was used to analyze the data within the ProHits-LIMS platform (Wang et al., 2015). A unique peptide-spectrum library was generated from the peptide-spectrum matches (PSMs) from the matched DDA runs (30 runs). Only those with the lowest MS-GFDB (Kim et al., 2010) probability, with respect to each unique peptide sequence and precursor charge state, and passed a peptide level false-discovery rate (FDR) of 1% using the Target-Decoy approach (Elias and Gygi, 2007). The MS-GFDB was set to search for tryptic cleavages with no missed cleavage sites. In addition, the peptide length was restricted from 8 to 30 amino acids and required precursors to be within a mass tolerance of 50ppm and have charge states 2+ to 4+. Fragment ions were searched with a tolerance of +/- 50ppm. Oxidized methionine was selected as a variable modification in the MS-GFDB search. The NCBI RefSeq database (version 57, January 30th, 2013) was used to search the spectra. This database contains 36241 human and adenovirus sequences and was supplemented with common contaminants from Max Planck Institute (http://maxquant.org/contaminants.zip) and the Global Proteome Machine (GPM; ftp://ftp.thegpm.org/fasta/cRAP/crap.fasta). The spectra library also incorporates non-redundant PSMs from the SWATH-Atlas library (https://www.nature.com/articles/sdata201431). Additional decoys were added to the spectra library using the decoy library command built in to MSPLIT with a fragment mass tolerance of +/- 0.05 Da. This spectral library was used for protein identification of DIA data using MSPLIT (Wang et al., 2015). The MSPLIT search required parent mass tolerance of +/- 25 Da and a fragment mass tolerance of +/- 50ppm.

bioRxiv preprint doi: https://doi.org/10.1101/632547; this version posted May 9, 2019. The copyright holder for this preprint (which was not certified by peer review) is the author/funder. All rights reserved. No reuse allowed without permission.

SAINT analysis: SAINTexpress version 3.6.1 was used as a statistical tool to calculate the probability of potential protein-protein interactions from background contaminants using default parameters (Teo et al., 2014). SAINT analysis was performed using two biological replicates per bait for both DDA and SWATH. Twenty-two negative control experiments were conducted for BioID; eleven with 3xFLAG-alone samples and eleven with BirA*FLAG-alone samples. Controls were compressed to 11 samples and two unique peptide ions and a minimum iProphet probability of 0.99 were required for protein identification. SAINT probabilities were calculated independently for each sample, averaged (AvgP) across biological replicates and reported as the final SAINT score. Only SAINT scores with a FDR ≤ 1% were considered high-confidence protein interactions.

Immunofluorescence of centrosomal proteins:

HEK293 Flp-In T-REx cells were grown on poly-L-lysine-coated #1.5 glass coverslips (Electron Microscopy Sciences). Cells were treated with 1 µg/mL doxycycline for 24 h to induce expression of BirA* or BirA*-CNAα. Media was then replaced with fresh media containing 1 µg/mL doxycycline and 50 μM biotin, and labeling was allowed to proceed for 18 hr. Cells were fixed with -20°C methanol for 15 minutes, washed with PBS and blocked with PBS-BT (3% BSA, 0.1% Triton X-100, 0.02% sodium azide in PBS) for 30 min. Coverslips were incubated with primary antibodies diluted in PBS-BT for 1 hr., washed with PBS-BT, incubated with secondary antibodies and DAPI diluted in PBS-BT for 1 hr., then washed again. Samples were mounted using Mowiol (Polysciences) in glycerol containing 1,4,-diazobicycli-[2.2.2]octane (DABCO, Sigma-Aldrich) antifade.

Primary antibodies used for immunofluorescence: mouse IgG2b anti-centrin3, clone 3e6 (1:1000, Novus Biological) and mouse IgG1 anti-gamma-tubulin, clone GTU-88 (1:1000, Sigma-Aldrich). For detecting biotinylation: Alexa594-streptavidin (1:1000, Thermo Fisher). Secondary antibodies used for immunofluorescence were diluted 1:1000: Alexa647 anti mouse IgG1 (ThermoFisher) and Alexa488 anti mouse IgG2b (ThermoFisher). For Fig. 4E, images were acquired as 0.3695 μm Z-stacks on a Leica SP8 scanning laser confocal microscope with a 63x/1.4 NA oil objective, using white light laser excitation at 80% power, and LASX Software. For Fig. S5C and D, images were acquired as 0.25 μm Z-stacks using a Zeiss Axio Observer microscope with a confocal spinning-disk head (Yokogawa), PlanApoChromat 63x/1.4 NA oil objective, and a Cascade II:512 EM-CCD camera (Photometrics), run with MicroManager software (Edelstein et al., 2014). Post-imaging processing was performed using Fiji (Schindelin et al., 2012). Images are maximum projections of confocal stacks.

In vitro interaction between CN and NUP153:

For GST-NUP153 protein expression, WT and PxIxIT$_{MUT}$ ($_{485}$PTFNFS$_{490}$ ➔ ATANFA) fragments of NUP153 (AAs 228-611) were fused C-terminally to GST in pGEX4T-3 and expressed in BL21 DE3 cells (Sigma CMC0014). Cell pellets were lysed (50 mM Tris-HCl pH 8.0, 100 mM NaCl, 2 mM EDTA, 2 mM EGTA, and 5mM DTT with protease inhibitors) and sonicated (4 x 30-second pulses at 40% output), followed by immediate addition of 1 M NaCl for a final [NaCl] of 200 mM, then clarified by serial centrifugation of lysates. Following centrifugation, bacterial lysates were supplemented with 0.1% Tween-20 (Sigma P7949) and incubated with equilibrated glutathione sepharose beads (FisherScientific 45000139) at 4°C for 2.5 hours with rotation. Lysate-bead reactions were then subjected to column purification: beads were washed with 20 volumes of wash buffer (50 mM Tris-HCl pH 8.0, 110 mM KOAc, 2 mM MgOAc, 0.1% Tween-20, 2 mM DTT and protease inhibitors) and then eluted with 40 mM reduced glutathione (pH 8.0; Sigma G4251) and 5 mM DTT. Eluted fractions with peak protein

bioRxiv preprint doi: https://doi.org/10.1101/632547; this version posted May 9, 2019. The copyright holder for this preprint (which was not certified by peer review) is the author/funder. All rights reserved. No reuse allowed without permission.

concentration were pooled and dialyzed (50 mM Tris-HCl, pH 7.5, 150 mM NaCl, 1 mM DTT and 1 mM PMSF).

For binding reactions, purified His-tagged CN (WT and NIR; purification described above) was incubated with ~1 μg GST-NUP153$_{228-611}$ (WT and PxIxIT$_{MUT}$), GST-NFATc1 (16 AA peptide), or GST alone at 4°C for 1 hour with rotation (base binding buffer: 50 mM Tris-HCl pH 7.5, 150 mM NaCl, 0.1% Triton-X 100, 10 mM Imidazole, 1 mM BME and protease inhibitors). Following GST-His incubation, equilibrated Ni-NTA beads (Fisher PI25214) were added to each reaction and incubated for another 2 hours at 4°C with rotation. Beads were washed three times in base binding buffer supplemented with 15 mM Imidazole, followed by elution with 2X sample buffer at 37°C. Input (3% of total binding reaction) and bound samples (50% of binding reaction) were subjected to SDS-PAGE followed by immunoblot analysis with His (Qiagen 34660) and GST (BioLegend MMS-112P) antibodies.

In vitro interaction between CN and NUP50:

His-tagged NUP50 WT or PxIxIT$_{MUT}$ (P.M.: P345A, V347A, V349A, T350A mutation) were purified from BL21 bacterial cells with Ni-NTA beads as described above for His-tagged calcineurin. 1-2 μg of GST protein, or GST-CN (purification described above) were bound to 20 μl of glutathione sepharose beads in binding buffer (50 mM Tris-HCl pH 7.5, 150 mM NaCl, 0.1% Tween 20, 1 mM DTT, protease inhibitors) for 1 hr. at 4°C followed by addition of 1-2 μg of purified NUP50-WT or NUP50-PxIxIT$_{MUT}$. 3% of the reaction mix was removed as 'input' for further analysis. After an incubation of 2-4 hours at 4°C, the beads were collected and washed twice in binding buffer. Associated proteins were extracted in 2XSDS buffer by boiling for 5 min. and then analyzed by SDS-PAGE using anti-GST and anti-His antibodies, as described above. Bound His-NUP50 was normalized to input and bound GST-proteins.

In vitro dephosphorylation of human nucleoporins:

Constitutively active ERK2 (Addgene # 39212) was purified from BL21-DE3 RIPL cells (Stratagene 230280) as previously described (Khokhlatchev et al., 1997). GST-tagged Nup153$_{228-611}$ and Nup50 (full length) were purified from BL21-DE3 (Stratagene 230245) cells as described above.

For phosphorylation/dephosphorylation reactions, first ~1 μg of purified GST-153$_{228-611}$ (WT and PxIxIT$_{MUT}$) were phosphorylated with ~100 ng purified ERK2 in kinase buffer (20 mM Tris-HCL pH 7.5, 15 mM $MgCl_2$, 1 mM EGTA, 2mM DTT and phosphatase inhibitors) supplemented with 100 μM ATP and γ^{32}P ATP (3 μCi/reaction) for 1 hour at 30°C and then quenched with 0.5 mM EDTA. Unincorporated ATP was removed using a Centri-Sep spin column (ThremoFisher 401762). GST-NUP153 proteins were removed from the reaction by pulldown using glutathione sepharose beads (FisherScientific 45000139) at room temperature for 30 minutes (buffer: 50 mM Tris-HCl pH 7.5, 150 mM NaCl, 1 mM DTT and protease inhibitors). Rinsed beads were resuspended in dephosphorylation buffer (50 mM Tris-HCl pH 7.5, 150 mM NaCl, 6 mM $CaCl_2$, 1 mM $MgCl_2$, 1 mM DTT and protease inhibitors) and incubated with 100 nM purified CN at 30°C. Time points were collected at 0, 15, and 60 minutes after addition of CN and the reactions stopped by heating with 2X SDS dye. Samples were subjected to SDS-PAGE analysis followed by Gel Code staining (Fisher P124590), then dried in a gel drier and exposed to a phosphor-imager screen to quantify incorporated ^{32}P signal. ^{32}P signal was normalized to protein amount. The data represent an average of 3 experiments.

Time Lapse Imaging and Nuclear Import Assay:

HeLa cells grown in DMEM supplemented with 10% FBS were plated on 25 mm glass coverslips and transfected (Lipofectamine LTX; Life Technologies) with a plasmid encoding a

bioRxiv preprint doi: https://doi.org/10.1101/632547; this version posted May 9, 2019. The copyright holder for this preprint (which was not certified by peer review) is the author/funder. All rights reserved. No reuse allowed without permission.

chimeric Rev-GFP-Glucocorticoid Receptor protein [RGG; (Love et al., 1998)], which can be induced to import into the nucleus upon addition of dexamethasone. Twenty-four hours after plasmid transfection, cells were pretreated for 1 hour with 1 μM FK506, 2 μM cyclosporin A, or an equivalent volume of DMSO (vehicle control). Coverslips of cells were subsequently mounted in a Ludin Chamber (Life Imaging Services) and changed to DMEM/F12 supplemented with 10% FBS and HEPES buffer. Nuclear import of the RGG biosensor was induced in the presence of DMSO, FK506, or cyclosporin A by adding dexamethasone at a final concentration of 100 nM. Imaging was performed on an inverted Nikon T*i*-E microscope (Nikon Instruments) equipped with a Nikon 20X Plan Apo NA 0.75 objective. This system utilized an Andor spinning disk confocal (Andor Technology) and an Andor Ixon 885 EMCCD camera. Time lapse sequences were captured at 30 second intervals for 90 minutes using the Andor IQ imaging software. Regions of interest containing the nuclear and cytoplasmic compartments of individual cells were manually drawn and applied to all images in the time-lapse sequence stack. Fluorescence intensity in these regions was measured using the ImageJ software (NIH) and graphed as a ratio of nuclear/cytoplasmic fluorescence for each cell.

In vivo interaction between CN and yeast nucleoporins:

GAL1 inducible and N-terminally GST-tagged clones of NUP1 (pEGH-NUP1), NUP2 (pEGH-NUP2) and NUP60 (pEGH-NUP60) were obtained from the yeast GST fusion collection (Zhu et al., 2001). These plasmids were transformed into yeast strain JRY19, a derivative of strain JRY11 (Goldman et al., 2014) containing *3X-GFP-CNA1* and *ACT1-GEV* (McIsaac et al., 2011). Transformants were grown to mid-log phase when the *GAL1* promoter was induced with 2.5 μM β–estradiol for 4 hr. Cells were treated with 1M NaCl (osmotic stress) and 200 mM $CaCl_2$ (to activate calcineurin) for 15 min. prior to harvesting and cell pellets were frozen at -80°C. Pellets were thawed in lysis buffer (50 mM Tris-HCl pH 7.5, 150 mM NaCl, 1% Tween 20, 1mM DTT, protease inhibitors) and lysed with silica beads in a FastPrep-24 homogenizer (MP Biomedicals) with two 40 sec pulses at 6.5 m/sec. Lysed cells were clarified by centrifugation at 20,000g for 20 min. 5-6 mg of lysate was used for pull-downs with 30 μl of GFP-Trap magnetic beads (Bulldog Bio. Inc.) in binding buffer (50 mM Tris-HCl pH 7.5, 150 mM NaCl, 0.1% Tween 20, 1mM DTT, protease inhibitors) containing 200 μM peptides (VIVIT: MAGPHP**VIVIT**GPHEE, or a scrambled version SCR: MAGIVPIHVTHAPGEE) (Aramburu et al., 1999). The binding reactions were incubated at 4°C for 2-4 hr. The beads were washed twice in binding buffer (the first wash containing 200 μM peptides) and co-purifying proteins were extracted with heating in 2X –SDS dye at 37°C for 10 min. Extracted proteins were analyzed by SDS-PAGE followed by Western analysis. GST-proteins were observed with a mouse anti-GST monoclonal antibody and GFP tagged CNA1 was observed with a rabbit anti-GFP polyclonal antibody followed by secondary Li-Cor antibodies. Blots were imaged with the Li-Cor Odyssey imaging system.

In vitro dephosphorylation of yeast nucleoporins:

Purification of Hog1 kinase from yeast: Yeast strain BY4741 was transformed with plasmids BG1805-Hog1 and BJ1805-Hog1-KD expressing ZZ-3C-HA-6XHIS tagged, wild-type and kinase-dead mutant versions of Hog1 respectively, from the inducible *GAL1* promoter (a kind gift from Jeremy Thorner). Transformants were grown in 4% raffinose containing medium to mid-log phase followed by induction of the GAL1 promoter with 2% galactose for 20 hrs. at 30°C. Cells were treated with 1M NaCl for 20 min. to activate the Hog1 pathway prior to harvesting. Cells were pelleted, washed with water and frozen. Cell pellets were thawed in lysis buffer (50 mM Tris-HCl pH 7.5, 150 mM NaCl, 0.1% Tween 20, 1mM β-mercapto ethanol, 5mM imidazole with protease and phosphatase inhibitors, as above) and lysed with silica beads in the FastPrep-24 homogenizer (MP Biomedicals) with two 40 sec pulses at 6.5 m/sec. Lysed cells were clarified

bioRxiv preprint doi: https://doi.org/10.1101/632547; this version posted May 9, 2019. The copyright holder for this preprint (which was not certified by peer review) is the author/funder. All rights reserved. No reuse allowed without permission.

by centrifugation at 20,000g for 20 min. 60 mg of total cell lysate was bound to 1 ml Ni-NTA beads in lysis buffer at 4°C for 4 hr. Beads were washed with buffer containing 10 mM Imidazole and eluted with 250 mM imidazole. Pooled eluted fractions were dialyzed in buffer containing 50 mM Tris-HCL pH 7.5, 150 mM NaCl, 1mM β-mercapto ethanol.

Purification of GST-tagged yeast NUP proteins: Plasmids expressing GST-tagged Nup1 (PSR19), Nup2 (PSR3), and Nup60 (PSR21) in pGEX4T-3 (kind gifts from Francesc Posas) were expressed in BL21 bacterial cells. Cells were grown to OD_{600} 0.7-0.8 and GST-tagged proteins were expressed at 18°C for 16-18 hrs. and purified using glutathione-sepharose beads as detailed above for GST-CN purification.

***In vitro* de-phosphorylation of GST-NUPs:** ~5-10 μg of purified GST-Nup1/2/60 were phosphorylated with 1 μg Hog1 kinase in kinase buffer (50 mM Tris-HCL pH 7.5, 10 mM $MgCl_2$, 1mM DTT) supplemented with 100 μM ATP and 2 μl γ^{32}P ATP (3000Ci/mmol) for 2 hr. at 30°C. Unincorporated ATP was removed using a Centri-Sep spin column (ThermoFisher USA). The reactions were then incubated for 1 hr. with 5 μl washed Ni-NTA beads and spun briefly to remove His-Hog1. Supernatants were then incubated with 100nM purified CN that had been pre-incubated with 100μM VIVIT or SCR (see above) for 5 min. at 30°C. De-phosphorylation reactions were carried out at 30°C. Aliquots were removed at 0, 10, 30 and 80 min and the reactions stopped by heating with 2X SDS dye. Samples were subjected to SDS-PAGE. Gels were first stained with Gel Code protein stain, then dried in a gel drier and exposed to a phosphor-imager screen to quantify incorporated ^{32}P signal. ^{32}P signal was normalized to protein amount. The data represent an average of at least 3 experiments.

Methods References

Altschul, S.F., Madden, T.L., Schaffer, A.A., Zhang, J., Zhang, Z., Miller, W., and Lipman, D.J. (1997). Gapped BLAST and PSI-BLAST: a new generation of protein database search programs. Nucleic acids research *25*, 3389-3402.

Aramburu, J., Yaffe, M.B., Lopez-Rodriguez, C., Cantley, L.C., Hogan, P.G., and Rao, A. (1999). Affinity-driven peptide selection of an NFAT inhibitor more selective than cyclosporin A. Science *285*, 2129-2133.

Davey, N.E., Cowan, J.L., Shields, D.C., Gibson, T.J., Coldwell, M.J., and Edwards, R.J. (2012). SLiMPrints: conservation-based discovery of functional motif fingerprints in intrinsically disordered protein regions. Nucleic acids research *40*, 10628-10641.

Davey, N.E., Seo, M.H., Yadav, V.K., Jeon, J., Nim, S., Krystkowiak, I., Blikstad, C., Dong, D., Markova, N., Kim, P.M.*, et al.* (2017). Discovery of short linear motif-mediated interactions through phage display of intrinsically disordered regions of the human proteome. FEBS J *284*, 485-498.

Dosztanyi, Z., Csizmok, V., Tompa, P., and Simon, I. (2005). IUPred: web server for the prediction of intrinsically unstructured regions of proteins based on estimated energy content. Bioinformatics *21*, 3433-3434.

Dosztanyi, Z., Meszaros, B., and Simon, I. (2009). ANCHOR: web server for predicting protein binding regions in disordered proteins. Bioinformatics *25*, 2745-2746.

Edelstein, A.D., Tsuchida, M.A., Amodaj, N., Pinkard, H., Vale, R.D., and Stuurman, N. (2014). Advanced methods of microscope control using muManager software. Journal of biological methods *1*.

Elias, J.E., and Gygi, S.P. (2007). Target-decoy search strategy for increased confidence in large-scale protein identifications by mass spectrometry. Nature methods *4*, 207-214.

Eng, J.K., Jahan, T.A., and Hoopmann, M.R. (2013). Comet: an open-source MS/MS sequence database search tool. Proteomics *13*, 22-24.

bioRxiv preprint doi: https://doi.org/10.1101/632547; this version posted May 9, 2019. The copyright holder for this preprint (which was not certified by peer review) is the author/funder. All rights reserved. No reuse allowed without permission.

Goldman, A., Roy, J., Bodenmiller, B., Wanka, S., Landry, C.R., Aebersold, R., and Cyert, M.S. (2014). The calcineurin signaling network evolves via conserved kinase-phosphatase modules that transcend substrate identity. Mol Cell *55*, 422-435.
Huang, H., and Sidhu, S.S. (2011). Studying binding specificities of peptide recognition modules by high-throughput phage display selections. Methods Mol Biol *781*, 87-97.
Jehl, P., Manguy, J., Shields, D.C., Higgins, D.G., and Davey, N.E. (2016). ProViz-a web-based visualization tool to investigate the functional and evolutionary features of protein sequences. Nucleic acids research *44*, W11-15.
Khokhlatchev, A., Xu, S., English, J., Wu, P., Schaefer, E., and Cobb, M.H. (1997). Reconstitution of mitogen-activated protein kinase phosphorylation cascades in bacteria. Efficient synthesis of active protein kinases. J Biol Chem *272*, 11057-11062.
Kim, S., Mischerikow, N., Bandeira, N., Navarro, J.D., Wich, L., Mohammed, S., Heck, A.J., and Pevzner, P.A. (2010). The generating function of CID, ETD, and CID/ETD pairs of tandem mass spectra: applications to database search. Mol Cell Proteomics *9*, 2840-2852.
Krystkowiak, I., and Davey, N.E. (2017). SLiMSearch: a framework for proteome-wide discovery and annotation of functional modules in intrinsically disordered regions. Nucleic acids research *45*, W464-W469.
Krystkowiak, I., Manguy, J., and Davey, N.E. (2018). PSSMSearch: a server for modeling, visualization, proteome-wide discovery and annotation of protein motif specificity determinants. Nucleic acids research *46*, W235-W241.
Liu, G., Knight, J.D., Zhang, J.P., Tsou, C.C., Wang, J., Lambert, J.P., Larsen, B., Tyers, M., Raught, B., Bandeira, N.*, et al.* (2016). Data Independent Acquisition analysis in ProHits 4.0. Journal of proteomics *149*, 64-68.
Love, D.C., Sweitzer, T.D., and Hanover, J.A. (1998). Reconstitution of HIV-1 rev nuclear export: independent requirements for nuclear import and export. Proc Natl Acad Sci U S A *95*, 10608-10613.
McIsaac, R.S., Silverman, S.J., McClean, M.N., Gibney, P.A., Macinskas, J., Hickman, M.J., Petti, A.A., and Botstein, D. (2011). Fast-acting and nearly gratuitous induction of gene expression and protein depletion in Saccharomyces cerevisiae. Mol Biol Cell *22*, 4447-4459.
Perkins, D.N., Pappin, D.J., Creasy, D.M., and Cottrell, J.S. (1999). Probability-based protein identification by searching sequence databases using mass spectrometry data. Electrophoresis *20*, 3551-3567.
Piovesan, D., Walsh, I., Minervini, G., and Tosatto, S.C.E. (2017). FELLS: fast estimator of latent local structure. Bioinformatics *33*, 1889-1891.
Schindelin, J., Arganda-Carreras, I., Frise, E., Kaynig, V., Longair, M., Pietzsch, T., Preibisch, S., Rueden, C., Saalfeld, S., Schmid, B.*, et al.* (2012). Fiji: an open-source platform for biological-image analysis. Nature methods *9*, 676-682.
Shteynberg, D., Deutsch, E.W., Lam, H., Eng, J.K., Sun, Z., Tasman, N., Mendoza, L., Moritz, R.L., Aebersold, R., and Nesvizhskii, A.I. (2011). iProphet: multi-level integrative analysis of shotgun proteomic data improves peptide and protein identification rates and error estimates. Mol Cell Proteomics *10*, M111 007690.
Teo, G., Liu, G., Zhang, J., Nesvizhskii, A.I., Gingras, A.C., and Choi, H. (2014). SAINTexpress: improvements and additional features in Significance Analysis of INTeractome software. Journal of proteomics *100*, 37-43.
UniProt, C. (2015). UniProt: a hub for protein information. Nucleic acids research *43*, D204-212.
Wang, J., Tucholska, M., Knight, J.D., Lambert, J.P., Tate, S., Larsen, B., Gingras, A.C., and Bandeira, N. (2015). MSPLIT-DIA: sensitive peptide identification for data-independent acquisition. Nature methods *12*, 1106-1108.

bioRxiv preprint doi: https://doi.org/10.1101/632547; this version posted May 9, 2019. The copyright holder for this preprint (which was not certified by peer review) is the author/funder. All rights reserved. No reuse allowed without permission.

Zhu, H., Bilgin, M., Bangham, R., Hall, D., Casamayor, A., Bertone, P., Lan, N., Jansen, R., Bidlingmaier, S., Houfek, T.*, et al.* (2001). Global analysis of protein activities using proteome chips. Science *293*, 2101-2105.

Text References

Aramburu, J., Yaffe, M.B., Lopez-Rodriguez, C., Cantley, L.C., Hogan, P.G., and Rao, A. (1999). Affinity-driven peptide selection of an NFAT inhibitor more selective than cyclosporin A. Science *285*, 2129-2133.
Azimzadeh, J., Hergert, P., Delouvee, A., Euteneuer, U., Formstecher, E., Khodjakov, A., and Bornens, M. (2009). hPOC5 is a centrin-binding protein required for assembly of full-length centrioles. The Journal of cell biology *185*, 101-114.
Bassel-Duby, R., and Olson, E.N. (2006). Signaling pathways in skeletal muscle remodeling. Annual review of biochemistry *75*, 19-37.
Bauerfeind, R., Takei, K., and De Camilli, P. (1997). Amphiphysin I is associated with coated endocytic intermediates and undergoes stimulation-dependent dephosphorylation in nerve terminals. J Biol Chem *272*, 30984-30992.
Baumgartel, K., and Mansuy, I.M. (2012). Neural functions of calcineurin in synaptic plasticity and memory. Learning & memory *19*, 375-384.
Beck, M., and Hurt, E. (2017). The nuclear pore complex: understanding its function through structural insight. Nature reviews Molecular cell biology *18*, 73-89.
Bengtson, C.P., and Bading, H. (2012). Nuclear calcium signaling. Advances in experimental medicine and biology *970*, 377-405.
Bitard-Feildel, T., Lamiable, A., Mornon, J.P., and Callebaut, I. (2018). Order in Disorder as Observed by the "Hydrophobic Cluster Analysis" of Protein Sequences. Proteomics *18*, e1800054.
Brautigan, D.L., and Shenolikar, S. (2018). Protein Serine/Threonine Phosphatases: Keys to Unlocking Regulators and Substrates. Annual review of biochemistry *87*, 921-964.
Chang, C.P., Neilson, J.R., Bayle, J.H., Gestwicki, J.E., Kuo, A., Stankunas, K., Graef, I.A., and Crabtree, G.R. (2004). A field of myocardial-endocardial NFAT signaling underlies heart valve morphogenesis. Cell *118*, 649-663.
Chircop, M., Malladi, C.S., Lian, A.T., Page, S.L., Zavortink, M., Gordon, C.P., McCluskey, A., and Robinson, P.J. (2010). Calcineurin activity is required for the completion of cytokinesis. Cellular and molecular life sciences : CMLS *67*, 3725-3737.
Cousin, M.A., and Robinson, P.J. (2001). The dephosphins: dephosphorylation by calcineurin triggers synaptic vesicle endocytosis. Trends in neurosciences *24*, 659-665.
Dantas, T.J., Daly, O.M., Conroy, P.C., Tomas, M., Wang, Y., Lalor, P., Dockery, P., Ferrando-May, E., and Morrison, C.G. (2013). Calcium-binding capacity of centrin2 is required for linear POC5 assembly but not for nucleotide excision repair. PLoS One *8*, e68487.
Davey, N.E., Seo, M.H., Yadav, V.K., Jeon, J., Nim, S., Krystkowiak, I., Blikstad, C., Dong, D., Markova, N., Kim, P.M.*, et al.* (2017). Discovery of short linear motif-mediated interactions through phage display of intrinsically disordered regions of the human proteome. FEBS J *284*, 485-498.
Delling, M., DeCaen, P.G., Doerner, J.F., Febvay, S., and Clapham, D.E. (2013). Primary cilia are specialized calcium signalling organelles. Nature *504*, 311-314.
Delling, M., Indzhykulian, A.A., Liu, X., Li, Y., Xie, T., Corey, D.P., and Clapham, D.E. (2016). Primary cilia are not calcium-responsive mechanosensors. Nature *531*, 656-660.
Dong, J.M., Tay, F.P., Swa, H.L., Gunaratne, J., Leung, T., Burke, B., and Manser, E. (2016). Proximity biotinylation provides insight into the molecular composition of focal adhesions at the nanometer scale. Science signaling *9*, rs4.

bioRxiv preprint doi: https://doi.org/10.1101/632547; this version posted May 9, 2019. The copyright holder for this preprint (which was not certified by peer review) is the author/funder. All rights reserved. No reuse allowed without permission.

Duan, L., and Cobb, M.H. (2010). Calcineurin increases glucose activation of ERK1/2 by reversing negative feedback. Proc Natl Acad Sci U S A *107*, 22314-22319.
Edwards, R.J., Davey, N.E., and Shields, D.C. (2007). SLiMFinder: a probabilistic method for identifying over-represented, convergently evolved, short linear motifs in proteins. PLoS One *2*, e967.
Firat-Karalar, E.N., Rauniyar, N., Yates, J.R., 3rd, and Stearns, T. (2014). Proximity interactions among centrosome components identify regulators of centriole duplication. Current biology : CB *24*, 664-670.
Fogeron, M.L., Muller, H., Schade, S., Dreher, F., Lehmann, V., Kuhnel, A., Scholz, A.K., Kashofer, K., Zerck, A., Fauler, B.*, et al.* (2013). LGALS3BP regulates centriole biogenesis and centrosome hypertrophy in cancer cells. Nature communications *4*, 1531.
Galletta, B.J., Guillen, R.X., Fagerstrom, C.J., Brownlee, C.W., Lerit, D.A., Megraw, T.L., Rogers, G.C., and Rusan, N.M. (2014). Drosophila pericentrin requires interaction with calmodulin for its function at centrosomes and neuronal basal bodies but not at sperm basal bodies. Mol Biol Cell *25*, 2682-2694.
Gingras, A.C., Abe, K.T., and Raught, B. (2018). Getting to know the neighborhood: using proximity-dependent biotinylation to characterize protein complexes and map organelles. Current opinion in chemical biology *48*, 44-54.
Goldman, A., Roy, J., Bodenmiller, B., Wanka, S., Landry, C.R., Aebersold, R., and Cyert, M.S. (2014). The calcineurin signaling network evolves via conserved kinase-phosphatase modules that transcend substrate identity. Mol Cell *55*, 422-435.
Greber, U.F., and Gerace, L. (1995). Depletion of calcium from the lumen of endoplasmic reticulum reversibly inhibits passive diffusion and signal-mediated transport into the nucleus. The Journal of cell biology *128*, 5-14.
Grigoriu, S., Bond, R., Cossio, P., Chen, J.A., Ly, N., Hummer, G., Page, R., Cyert, M.S., and Peti, W. (2013). The molecular mechanism of substrate engagement and immunosuppressant inhibition of calcineurin. PLoS biology *11*, e1001492.
Guiney, E.L., Goldman, A.R., Elias, J.E., and Cyert, M.S. (2015). Calcineurin regulates the yeast synaptojanin Inp53/Sjl3 during membrane stress. Mol Biol Cell *26*, 769-785.
Gupta, G.D., Coyaud, E., Goncalves, J., Mojarad, B.A., Liu, Y., Wu, Q., Gheiratmand, L., Comartin, D., Tkach, J.M., Cheung, S.W.*, et al.* (2015). A Dynamic Protein Interaction Landscape of the Human Centrosome-Cilium Interface. Cell *163*, 1484-1499.
Hallhuber, M., Burkard, N., Wu, R., Buch, M.H., Engelhardt, S., Hein, L., Neyses, L., Schuh, K., and Ritter, O. (2006). Inhibition of nuclear import of calcineurin prevents myocardial hypertrophy. Circulation research *99*, 626-635.
Hoffman, A., Taleski, G., and Sontag, E. (2017). The protein serine/threonine phosphatases PP2A, PP1 and calcineurin: A triple threat in the regulation of the neuronal cytoskeleton. Molecular and cellular neurosciences *84*, 119-131.
Hoorn, E.J., Walsh, S.B., McCormick, J.A., Furstenberg, A., Yang, C.L., Roeschel, T., Paliege, A., Howie, A.J., Conley, J., Bachmann, S.*, et al.* (2011). The calcineurin inhibitor tacrolimus activates the renal sodium chloride cotransporter to cause hypertension. Nature medicine *17*, 1304-1309.
Huang, C.H., Chen, Y.C., and Chen, C.C. (2013). Physical interaction between calcineurin and Cav3.2 T-type Ca2+ channel modulates their functions. FEBS Lett *587*, 1723-1730.
Ivarsson, Y., and Jemth, P. (2018). Affinity and specificity of motif-based protein-protein interactions. Current opinion in structural biology *54*, 26-33.
Jain, J., McCaffrey, P.G., Miner, Z., Kerppola, T.K., Lambert, J.N., Verdine, G.L., Curran, T., and Rao, A. (1993). The T-cell transcription factor NFATp is a substrate for calcineurin and interacts with Fos and Jun. Nature *365*, 352-355.

bioRxiv preprint doi: https://doi.org/10.1101/632547; this version posted May 9, 2019. The copyright holder for this preprint (which was not certified by peer review) is the author/funder. All rights reserved. No reuse allowed without permission.

Kasahara, A., Cipolat, S., Chen, Y., Dorn, G.W., 2nd, and Scorrano, L. (2013). Mitochondrial fusion directs cardiomyocyte differentiation via calcineurin and Notch signaling. Science *342*, 734-737.
Kataria, M., Mouilleron, S., Seo, M.H., Corbi-Verge, C., Kim, P.M., and Uhlmann, F. (2018). A PxL motif promotes timely cell cycle substrate dephosphorylation by the Cdc14 phosphatase. Nat Struct Mol Biol *25*, 1093-1102.
Kodiha, M., Tran, D., Morogan, A., Qian, C., and Stochaj, U. (2009). Dissecting the signaling events that impact classical nuclear import and target nuclear transport factors. PLoS One *4*, e8420.
Kohansal-Nodehi, M., Chua, J.J., Urlaub, H., Jahn, R., and Czernik, D. (2016). Analysis of protein phosphorylation in nerve terminal reveals extensive changes in active zone proteins upon exocytosis. eLife *5*.
Kosako, H., Yamaguchi, N., Aranami, C., Ushiyama, M., Kose, S., Imamoto, N., Taniguchi, H., Nishida, E., and Hattori, S. (2009). Phosphoproteomics reveals new ERK MAP kinase targets and links ERK to nucleoporin-mediated nuclear transport. Nat Struct Mol Biol *16*, 1026-1035.
Krystkowiak, I., Manguy, J., and Davey, N.E. (2018). PSSMSearch: a server for modeling, visualization, proteome-wide discovery and annotation of protein motif specificity determinants. Nucleic acids research *46*, W235-W241.
Li, H., Rao, A., and Hogan, P.G. (2004). Structural delineation of the calcineurin-NFAT interaction and its parallels to PP1 targeting interactions. J Mol Biol *342*, 1659-1674.
Lin, C.H., Yeh, S.H., Leu, T.H., Chang, W.C., Wang, S.T., and Gean, P.W. (2003). Identification of calcineurin as a key signal in the extinction of fear memory. J Neurosci *23*, 1574-1579.
Liu, J. (1993). FK506 and ciclosporin: molecular probes for studying intracellular signal transduction. Trends in pharmacological sciences *14*, 182-188.
Liu, Q., Busby, J.C., and Molkentin, J.D. (2009). Interaction between TAK1-TAB1-TAB2 and RCAN1-calcineurin defines a signalling nodal control point. Nat Cell Biol *11*, 154-161.
Ljubojevic, S., and Bers, D.M. (2015). Nuclear calcium in cardiac myocytes. J Cardiovasc Pharmacol *65*, 211-217.
Love, D.C., Sweitzer, T.D., and Hanover, J.A. (1998). Reconstitution of HIV-1 rev nuclear export: independent requirements for nuclear import and export. Proc Natl Acad Sci U S A *95*, 10608-10613.
Maillet, M., Davis, J., Auger-Messier, M., York, A., Osinska, H., Piquereau, J., Lorenz, J.N., Robbins, J., Ventura-Clapier, R., and Molkentin, J.D. (2010). Heart-specific deletion of CnB1 reveals multiple mechanisms whereby calcineurin regulates cardiac growth and function. J Biol Chem *285*, 6716-6724.
Mammucari, C., Tommasi di Vignano, A., Sharov, A.A., Neilson, J., Havrda, M.C., Roop, D.R., Botchkarev, V.A., Crabtree, G.R., and Dotto, G.P. (2005). Integration of Notch 1 and calcineurin/NFAT signaling pathways in keratinocyte growth and differentiation control. Dev Cell *8*, 665-676.
Medyouf, H., Alcalde, H., Berthier, C., Guillemin, M.C., dos Santos, N.R., Janin, A., Decaudin, D., de The, H., and Ghysdael, J. (2007). Targeting calcineurin activation as a therapeutic strategy for T-cell acute lymphoblastic leukemia. Nature medicine *13*, 736-741.
Mehta, S., and Zhang, J. (2014). Using a genetically encoded FRET-based reporter to visualize calcineurin phosphatase activity in living cells. Methods Mol Biol *1071*, 139-149.
Mellacheruvu, D., Wright, Z., Couzens, A.L., Lambert, J.P., St-Denis, N.A., Li, T., Miteva, Y.V., Hauri, S., Sardiu, M.E., Low, T.Y.*, et al.* (2013). The CRAPome: a contaminant repository for affinity purification-mass spectrometry data. Nature methods *10*, 730-736.
Mi, H., Muruganujan, A., Casagrande, J.T., and Thomas, P.D. (2013). Large-scale gene function analysis with the PANTHER classification system. Nature protocols *8*, 1551-1566.

bioRxiv preprint doi: https://doi.org/10.1101/632547; this version posted May 9, 2019. The copyright holder for this preprint (which was not certified by peer review) is the author/funder. All rights reserved. No reuse allowed without permission.

Mizuguchi, T., Nakashima, M., Kato, M., Okamoto, N., Kurahashi, H., Ekhilevitch, N., Shiina, M., Nishimura, G., Shibata, T., Matsuo, M.*, et al.* (2018). Loss-of-function and gain-of-function mutations in PPP3CA cause two distinct disorders. Hum Mol Genet *27*, 1421-1433.
Mooren, O.L., Erickson, E.S., Moore-Nichols, D., and Dunn, R.C. (2004). Nuclear side conformational changes in the nuclear pore complex following calcium release from the nuclear membrane. Physical biology *1*, 125-134.
Myers, C.T., Stong, N., Mountier, E.I., Helbig, K.L., Freytag, S., Sullivan, J.E., Ben Zeev, B., Nissenkorn, A., Tzadok, M., Heimer, G.*, et al.* (2017). De Novo Mutations in PPP3CA Cause Severe Neurodevelopmental Disease with Seizures. Am J Hum Genet *101*, 516-524.
Naguro, I., Umeda, T., Kobayashi, Y., Maruyama, J., Hattori, K., Shimizu, Y., Kataoka, K., Kim-Mitsuyama, S., Uchida, S., Vandewalle, A.*, et al.* (2012). ASK3 responds to osmotic stress and regulates blood pressure by suppressing WNK1-SPAK/OSR1 signaling in the kidney. Nature communications *3*, 1285.
Nakamura, T., Katagiri, T., Sato, S., Kushibiki, T., Hontani, K., Tsuchikawa, T., Hirano, S., and Nakamura, Y. (2017). Overexpression of C16orf74 is involved in aggressive pancreatic cancers. Oncotarget *8*, 50460-50475.
Nygren, P.J., and Scott, J.D. (2016). Regulation of the phosphatase PP2B by protein-protein interactions. Biochem Soc Trans *44*, 1313-1319.
O'Keefe, S.J., Tamura, J., Kincaid, R.L., Tocci, M.J., and O'Neill, E.A. (1992). FK-506- and CsA-sensitive activation of the interleukin-2 promoter by calcineurin. Nature *357*, 692-694.
Pan, F., Ye, Z., Cheng, L., and Liu, J.O. (2004). Myocyte enhancer factor 2 mediates calcium-dependent transcription of the interleukin-2 gene in T lymphocytes: a calcium signaling module that is distinct from but collaborates with the nuclear factor of activated T cells (NFAT). J Biol Chem *279*, 14477-14480.
Parra, V., and Rothermel, B.A. (2017). Calcineurin signaling in the heart: The importance of time and place. J Mol Cell Cardiol *103*, 121-136.
Paulillo, S.M., Powers, M.A., Ullman, K.S., and Fahrenkrog, B. (2006). Changes in nucleoporin domain topology in response to chemical effectors. J Mol Biol *363*, 39-50.
Porter, F.W., Brown, B., and Palmenberg, A.C. (2010). Nucleoporin phosphorylation triggered by the encephalomyocarditis virus leader protein is mediated by mitogen-activated protein kinases. J Virol *84*, 12538-12548.
Regot, S., de Nadal, E., Rodriguez-Navarro, S., Gonzalez-Novo, A., Perez-Fernandez, J., Gadal, O., Seisenbacher, G., Ammerer, G., and Posas, F. (2013). The Hog1 stress-activated protein kinase targets nucleoporins to control mRNA export upon stress. J Biol Chem *288*, 17384-17398.
Rizzo, F., and Staub, O. (2015). NEDD4-2 and salt-sensitive hypertension. Curr Opin Nephrol Hypertens *24*, 111-116.
Rodriguez, A., Roy, J., Martinez-Martinez, S., Lopez-Maderuelo, M.D., Nino-Moreno, P., Orti, L., Pantoja-Uceda, D., Pineda-Lucena, A., Cyert, M.S., and Redondo, J.M. (2009). A conserved docking surface on calcineurin mediates interaction with substrates and immunosuppressants. Mol Cell *33*, 616-626.
Roux, K.J., Kim, D.I., Raida, M., and Burke, B. (2012). A promiscuous biotin ligase fusion protein identifies proximal and interacting proteins in mammalian cells. The Journal of cell biology *196*, 801-810.
Roy, J., and Cyert, M.S. (2009). Cracking the phosphatase code: docking interactions determine substrate specificity. Science signaling *2*, re9.
Roy, J., and Cyert, M.S. (2019). Identifying new substrates and functions for an old enzyme: Calcineurin. . Cold Spring Harb Perspect Biol

bioRxiv preprint doi: https://doi.org/10.1101/632547; this version posted May 9, 2019. The copyright holder for this preprint (which was not certified by peer review) is the author/funder. All rights reserved. No reuse allowed without permission.

Roy, J., Li, H., Hogan, P.G., and Cyert, M.S. (2007). A conserved docking site modulates substrate affinity for calcineurin, signaling output, and in vivo function. Mol Cell *25*, 889-901.
Sakiyama, Y., Panatala, R., and Lim, R.Y.H. (2017). Structural dynamics of the nuclear pore complex. Seminars in cell & developmental biology *68*, 27-33.
Sales Gil, R., de Castro, I.J., Berihun, J., and Vagnarelli, P. (2018). Protein phosphatases at the nuclear envelope. Biochem Soc Trans *46*, 173-182.
Sarma, A., and Yang, W. (2011). Calcium regulation of nucleocytoplasmic transport. Protein Cell *2*, 291-302.
Sheftic, S.R., Page, R., and Peti, W. (2016). Investigating the human Calcineurin Interaction Network using the piLxVP SLiM. Sci Rep *6*, 38920.
Singla, V., Romaguera-Ros, M., Garcia-Verdugo, J.M., and Reiter, J.F. (2010). Ofd1, a human disease gene, regulates the length and distal structure of centrioles. Dev Cell *18*, 410-424.
Spektor, A., Tsang, W.Y., Khoo, D., and Dynlacht, B.D. (2007). Cep97 and CP110 suppress a cilia assembly program. Cell *130*, 678-690.
Stevenson, N.L., Bergen, D.J.M., Xu, A., Wyatt, E., Henry, F., McCaughey, J., Vuolo, L., Hammond, C.L., and Stephens, D.J. (2018). Regulator of calcineurin-2 is a centriolar protein with a role in cilia length control. Journal of cell science *131*.
Stevers, L.M., de Vink, P.J., Ottmann, C., Huskens, J., and Brunsveld, L. (2018). A Thermodynamic Model for Multivalency in 14-3-3 Protein-Protein Interactions. Journal of the American Chemical Society *140*, 14498-14510.
Stoffler, D., Goldie, K.N., Feja, B., and Aebi, U. (1999). Calcium-mediated structural changes of native nuclear pore complexes monitored by time-lapse atomic force microscopy. J Mol Biol *287*, 741-752.
Strubing, C., and Clapham, D.E. (1999). Active nuclear import and export is independent of lumenal Ca2+ stores in intact mammalian cells. The Journal of general physiology *113*, 239-248.
Stuart, S.A., Houel, S., Lee, T., Wang, N., Old, W.M., and Ahn, N.G. (2015). A Phosphoproteomic Comparison of B-RAFV600E and MKK1/2 Inhibitors in Melanoma Cells. Mol Cell Proteomics *14*, 1599-1615.
Suh, J., Foster, D.J., Davoudi, H., Wilson, M.A., and Tonegawa, S. (2013). Impaired hippocampal ripple-associated replay in a mouse model of schizophrenia. Neuron *80*, 484-493.
Szklarczyk, D., Morris, J.H., Cook, H., Kuhn, M., Wyder, S., Simonovic, M., Santos, A., Doncheva, N.T., Roth, A., Bork, P.*, et al.* (2017). The STRING database in 2017: quality-controlled protein-protein association networks, made broadly accessible. Nucleic acids research *45*, D362-D368.
Tian, X., Kai, L., Hockberger, P.E., Wokosin, D.L., and Surmeier, D.J. (2010). MEF-2 regulates activity-dependent spine loss in striatopallidal medium spiny neurons. Molecular and cellular neurosciences *44*, 94-108.
Tompa, P., Davey, N.E., Gibson, T.J., and Babu, M.M. (2014). A million peptide motifs for the molecular biologist. Mol Cell *55*, 161-169.
Tsang, W.Y., and Dynlacht, B.D. (2013). CP110 and its network of partners coordinately regulate cilia assembly. Cilia *2*, 9.
Tsang, W.Y., Spektor, A., Luciano, D.J., Indjeian, V.B., Chen, Z., Salisbury, J.L., Sanchez, I., and Dynlacht, B.D. (2006). CP110 cooperates with two calcium-binding proteins to regulate cytokinesis and genome stability. Mol Biol Cell *17*, 3423-3434.
Tzoneva, G., and Ferrando, A.A. (2012). Recent advances on NOTCH signaling in T-ALL. Current topics in microbiology and immunology *360*, 163-182.

bioRxiv preprint doi: https://doi.org/10.1101/632547; this version posted May 9, 2019. The copyright holder for this preprint (which was not certified by peer review) is the author/funder. All rights reserved. No reuse allowed without permission.

Uyar, B., Weatheritt, R.J., Dinkel, H., Davey, N.E., and Gibson, T.J. (2014). Proteome-wide analysis of human disease mutations in short linear motifs: neglected players in cancer? Molecular bioSystems *10*, 2626-2642.
Van Roey, K., Uyar, B., Weatheritt, R.J., Dinkel, H., Seiler, M., Budd, A., Gibson, T.J., and Davey, N.E. (2014). Short linear motifs: ubiquitous and functionally diverse protein interaction modules directing cell regulation. Chemical reviews *114*, 6733-6778.
Wagstaff, K.M., and Jans, D.A. (2009). Importins and beyond: non-conventional nuclear transport mechanisms. Traffic *10*, 1188-1198.
Wang, J., Lin, Z.J., Liu, L., Xu, H.Q., Shi, Y.W., Yi, Y.H., He, N., and Liao, W.P. (2017). Epilepsy-associated genes. Seizure *44*, 11-20.
Wilkins, B.J., and Molkentin, J.D. (2004). Calcium-calcineurin signaling in the regulation of cardiac hypertrophy. Biochem Biophys Res Commun *322*, 1178-1191.
Yaffe, M.B. (2002). How do 14-3-3 proteins work?-- Gatekeeper phosphorylation and the molecular anvil hypothesis. FEBS Lett *513*, 53-57.
Zhu, H., Bilgin, M., Bangham, R., Hall, D., Casamayor, A., Bertone, P., Lan, N., Jansen, R., Bidlingmaier, S., Houfek, T.*, et al.* (2001). Global analysis of protein activities using proteome chips. Science *293*, 2101-2105.

bioRxiv preprint doi: https://doi.org/10.1101/632547; this version posted May 9, 2019. The copyright holder for this preprint (which was not certified by peer review) is the author/funder. All rights reserved. No reuse allowed without permission.

Figure 1

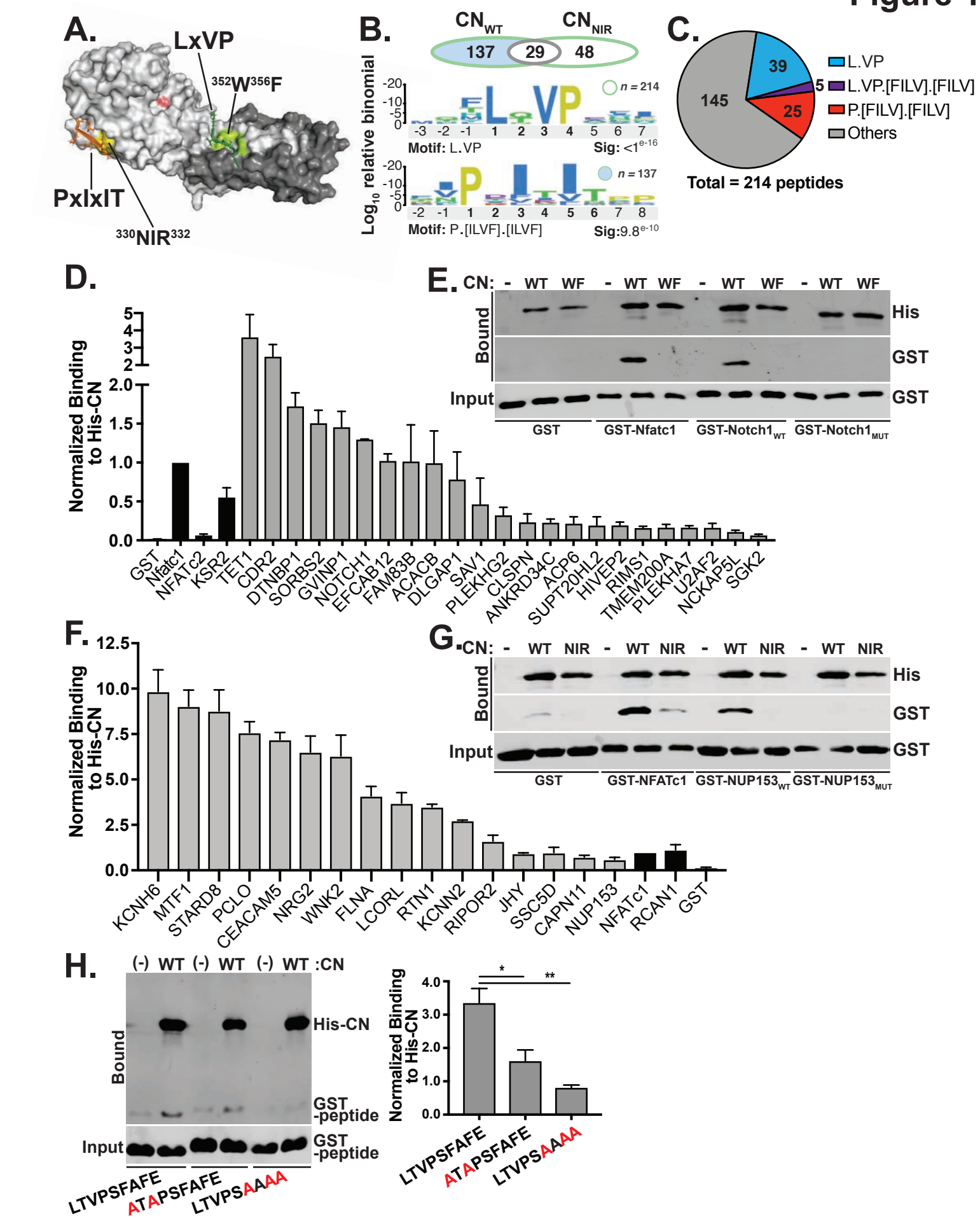

bioRxiv preprint doi: https://doi.org/10.1101/632547; this version posted May 9, 2019. The copyright holder for this preprint (which was not certified by peer review) is the author/funder. All rights reserved. No reuse allowed without permission.

Figure 2

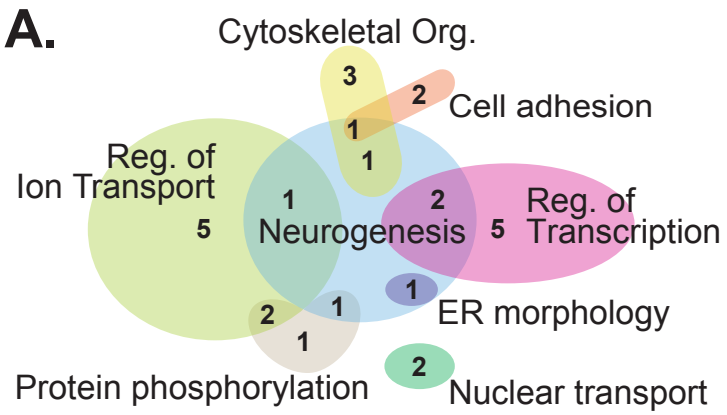

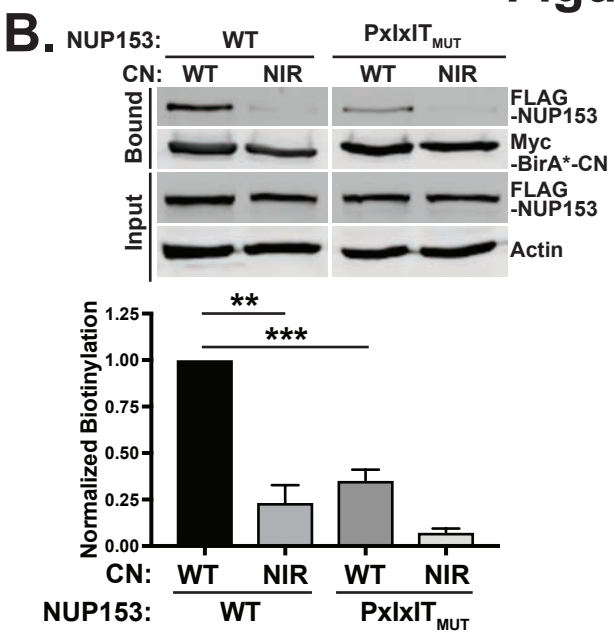

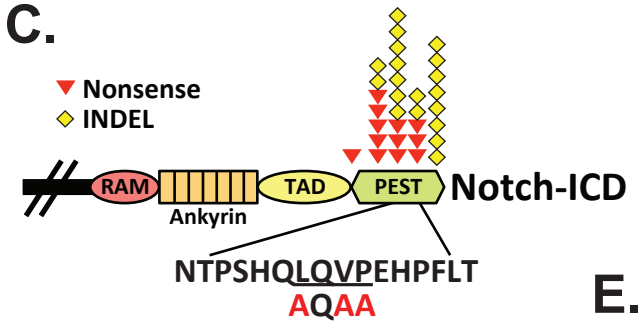

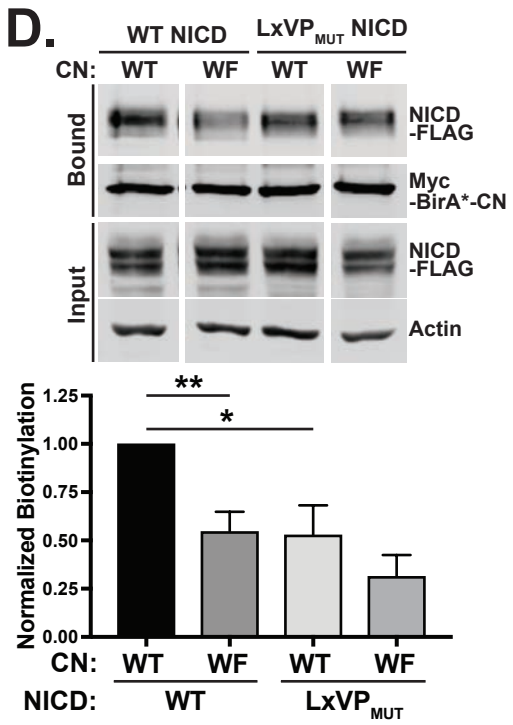

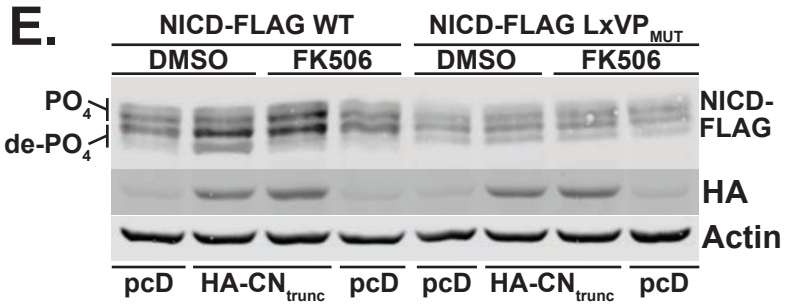

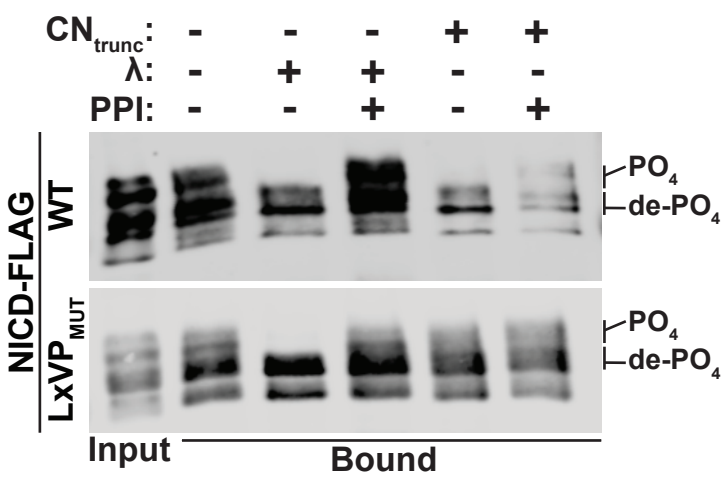

bioRxiv preprint doi: https://doi.org/10.1101/632547; this version posted May 9, 2019. The copyright holder for this preprint (which was not certified by peer review) is the author/funder. All rights reserved. No reuse allowed without permission.

Figure 3

A.

		Gene
Known	335-MEP IAIIIT DTE-346	AKAP79
	2143-KFP PEITVT PPT-2154	CABIN1
	2187-MSP PCISVE PPA-2198	CACNA1H
	841-PGV PRITIS DP-COOH	DYN1-Iso3
	341-DDI PTVVIH PPE-352	SLC4A7
	197-EAV PQIIIS AEE-208	TRESK
	115-LES PRIEIT SCL-126	NFATC1
	108-GLS PRIEIT PSH-119	NFATC2
	106-FEC PSIQIT SIS-117	NFATC3
	111-LEC PSIRIT SIS-122	NFATC4
	712-EDL PVITID PAS-723	NHE1
	206-DTT PSVVVH VCE-217	RCAN1
	33-LDV PDIIIT PPT-44	C16orf74
ProP-PD validated	482-SSL PTFNFS SPE-493	NUP153
	613-TQV PTFEIT SPN-624	NRG2
	1900-MKV PTISVT SFH-1911	WNK2
	2261-LTV PSFAFE PLD-2272	CACNA1H
	61-SSA PEIVVS KPE-72	KCNN2
	1057-RTN PDLILT SPD-1068	SSC5D
	1064-LTS PDFALS TPD-1075	SSC5D
	5-KLI PKLSIQ SPV-16	JHY
	454-STN PEITIT PAE-465	RIPOR2
	179-SQI PQFTLN FVE-190	RTN1
	313-DTV PTVTVS EPE-324	KCNH6
	545-TNN PTITIT PTP-556	MTF1
	2164-LKI PEISIQ DMT-2175	FLNA
	2056-LSI PDVKIT QHF-2067	PCLO
	58-LAV PAVSVD RKG-69	CACUL1
	284-LFI PNITVN NSG-295	CEACAM5
	405-TSN PTVQLK IPQ-416	LCORL
	412-LKI PQLRVS SVS-423	LCORL
	416-WTN PQFKIS LPE-427	CAPN11
	76-TSL PVITVS LPP-87	STARD8

B.

		Gene
Known	2259-EHLTVPS-2265	CACNA1H
	624-NLLDVPV-630	DNM1L
	84-EDLEVPV-90	PRKAR2A
	385-QYLAVPQ-391	NFATC1
	367-SILLVPP-373	NFATC2
	391-QFLSVPS-397	NFATC3
	376-DYLAVPS-382	NFATC4
	238-NTLQLPP-244	KCNK18
	391-NTLSVPR-397	KSR2
ProP-PD validated	612-HTLQVPE-618	FAM83B
	431-VFLPVPP-437	TET1
	166-QYLNVPP-172	ANKRD34C
	649-LTLQVPQ-655	SUPT20HL2
	489-NFLNIPQ-495	NFIX
	290-QSLLVPA-296	SAV1
	2500-HQLQVPE-2506	NOTCH1
	294-MFLTVPE-300	CDR2
	393-QTLQVPT-399	ACACB
	556-SMLEVPR-562	PLEKHA7
	79-QLLEVPP-85	ACP6
	46-LLLPVPP-52	SGK2
	1005-EFLTVPA-1011	HIVEP2
	711-GFLSVPK-717	CLSPN
	403-SSLMVPK-409	KCNJ8
	309-DLLTVPA-315	EFCAB12
	205-ELLSVPK-211	GVINP1
	340-QHLDVPR-346	SORBS2
	281-ITLQVPN-287	DTNBP1
	936-TTLTVPE-942	RIMS1
	962-LHLQVPA-968	PLEKHG2
	583-LTLEVPQ-589	NCKAP5L
	356-VTLQVPG-362	U2AF2
	316-QYLQVPQ-322	DLGAP1
	325-DSLVVPL-331	TMEM200A

C.

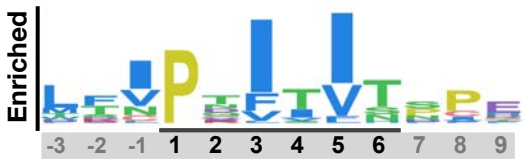

D.

E.

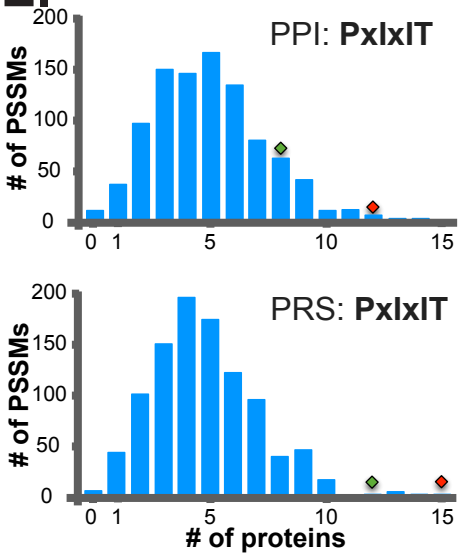

F.

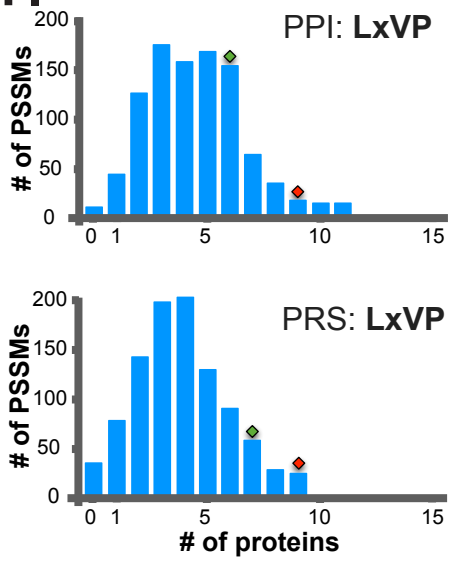

bioRxiv preprint doi: https://doi.org/10.1101/632547; this version posted May 9, 2019. The copyright holder for this preprint (which was not certified by peer review) is the author/funder. All rights reserved. No reuse allowed without permission.

Figure 4

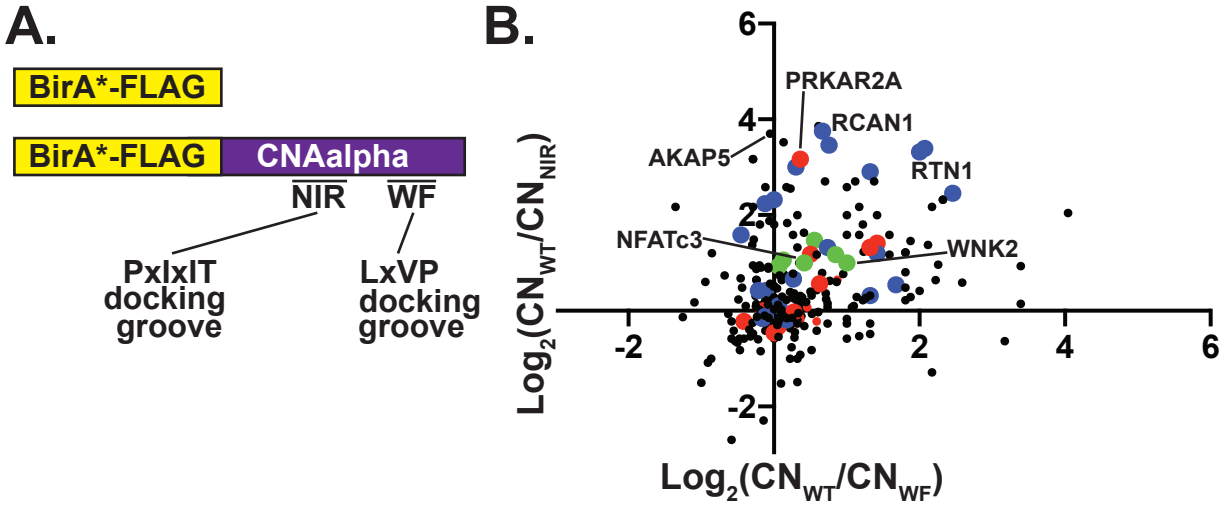

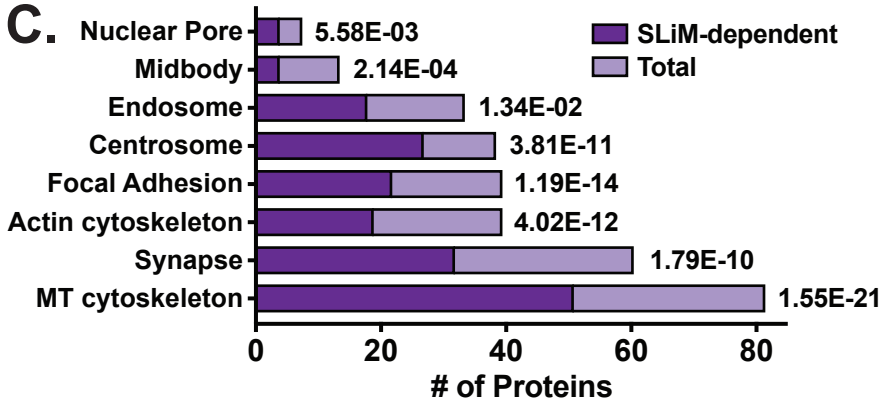

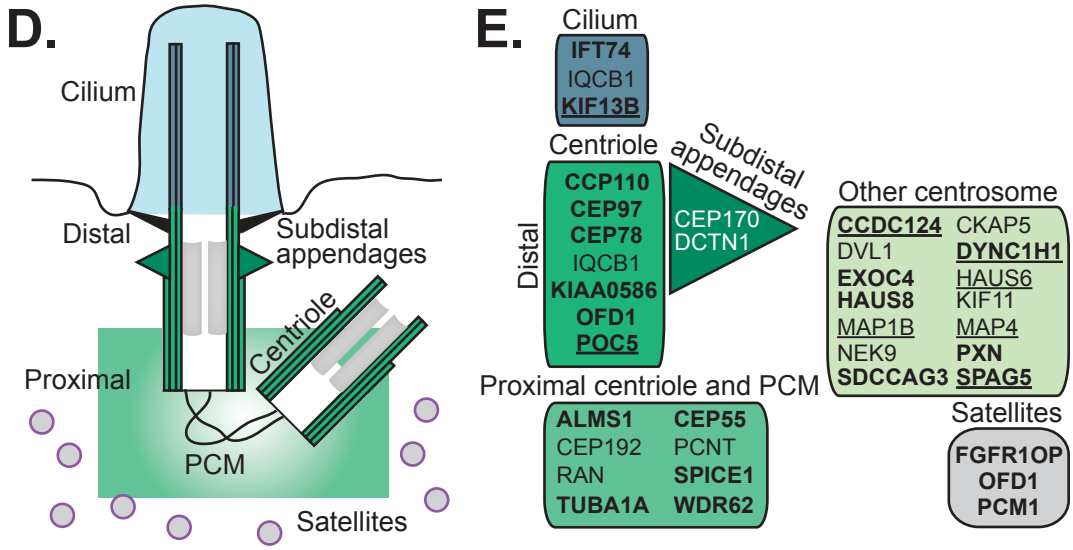

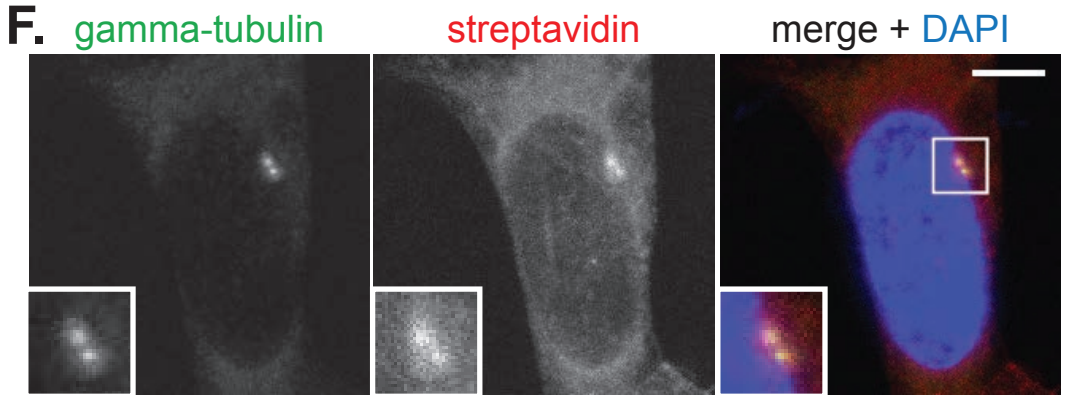

bioRxiv preprint doi: https://doi.org/10.1101/632547; this version posted May 9, 2019. The copyright holder for this preprint (which was not certified by peer review) is the author/funder. All rights reserved. No reuse allowed without permission.

Figure 5

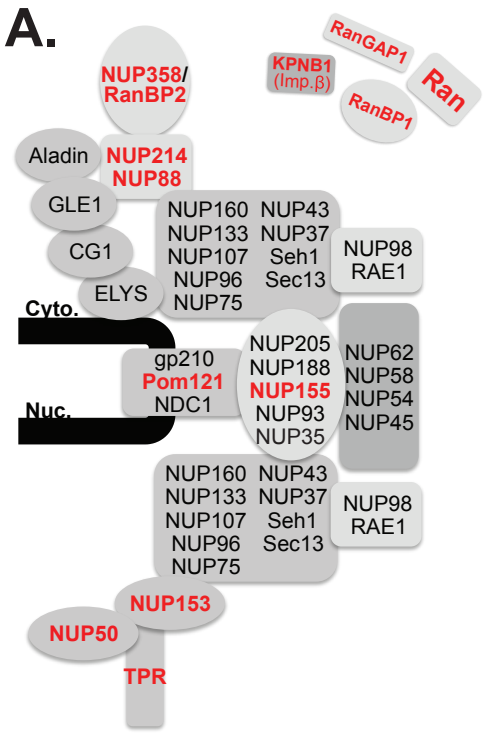

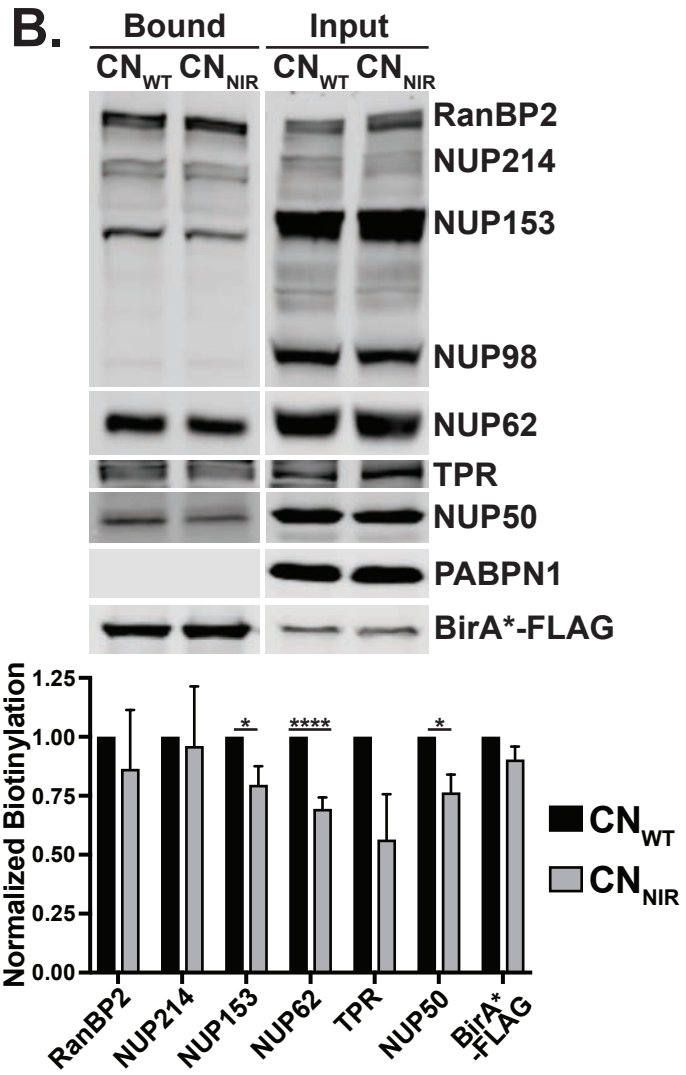

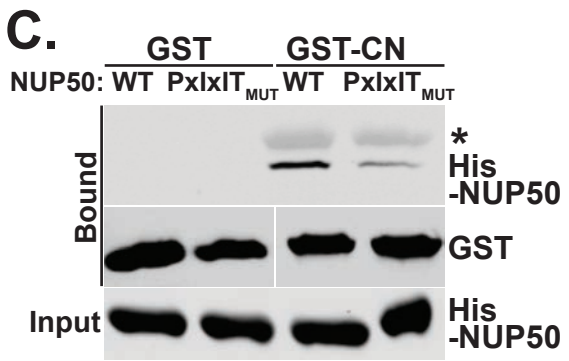

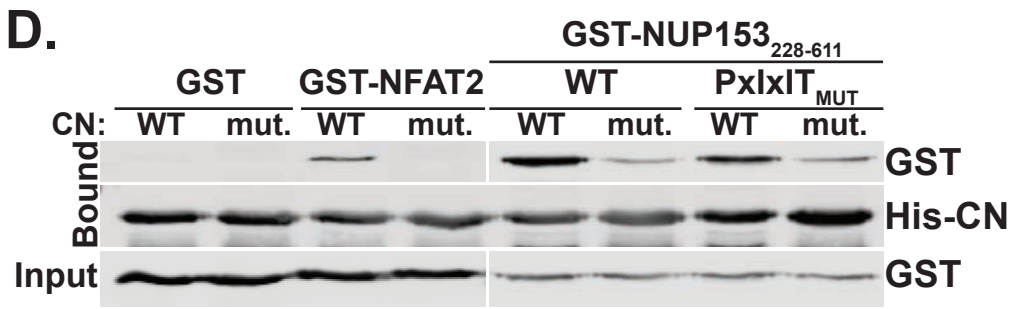

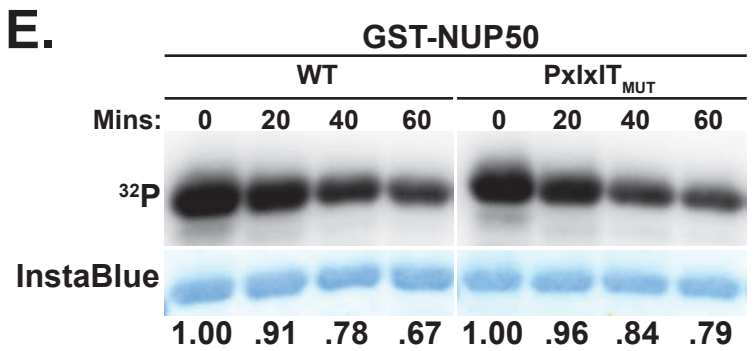

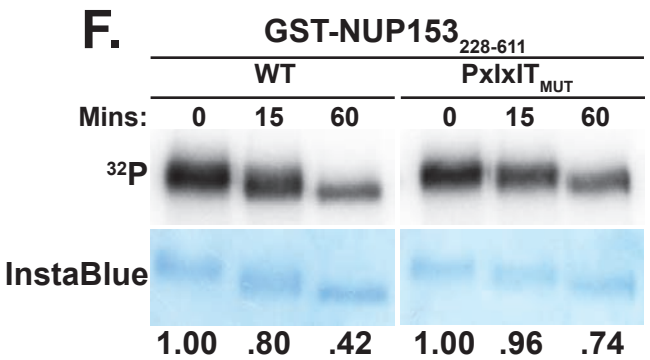

bioRxiv preprint doi: https://doi.org/10.1101/632547; this version posted May 9, 2019. The copyright holder for this preprint (which was not certified by peer review) is the author/funder. All rights reserved. No reuse allowed without permission.

Figure 6

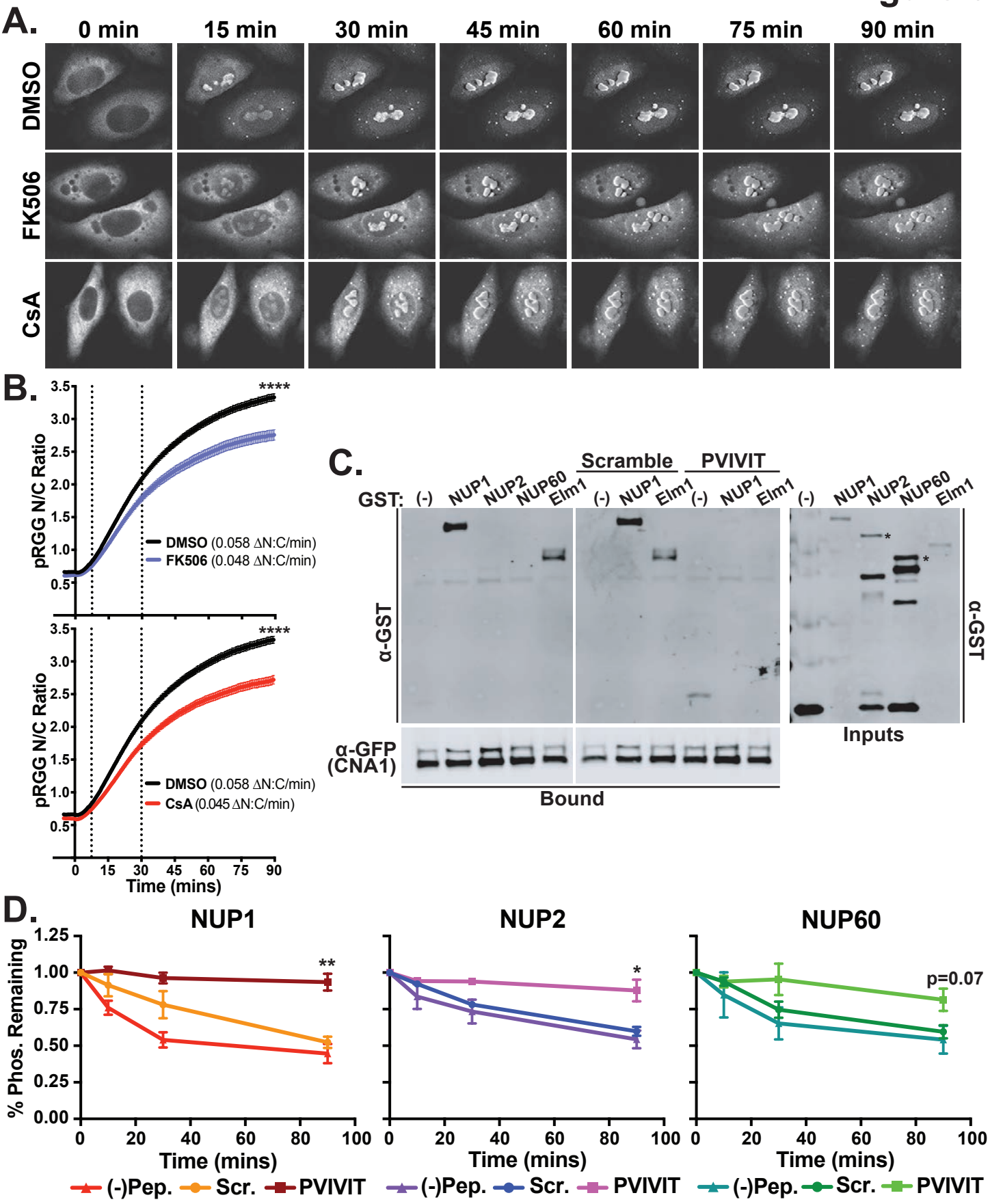

bioRxiv preprint doi: https://doi.org/10.1101/632547; this version posted May 9, 2019. The copyright holder for this preprint (which was not certified by peer review) is the author/funder. All rights reserved. No reuse allowed without permission.

Figure 7

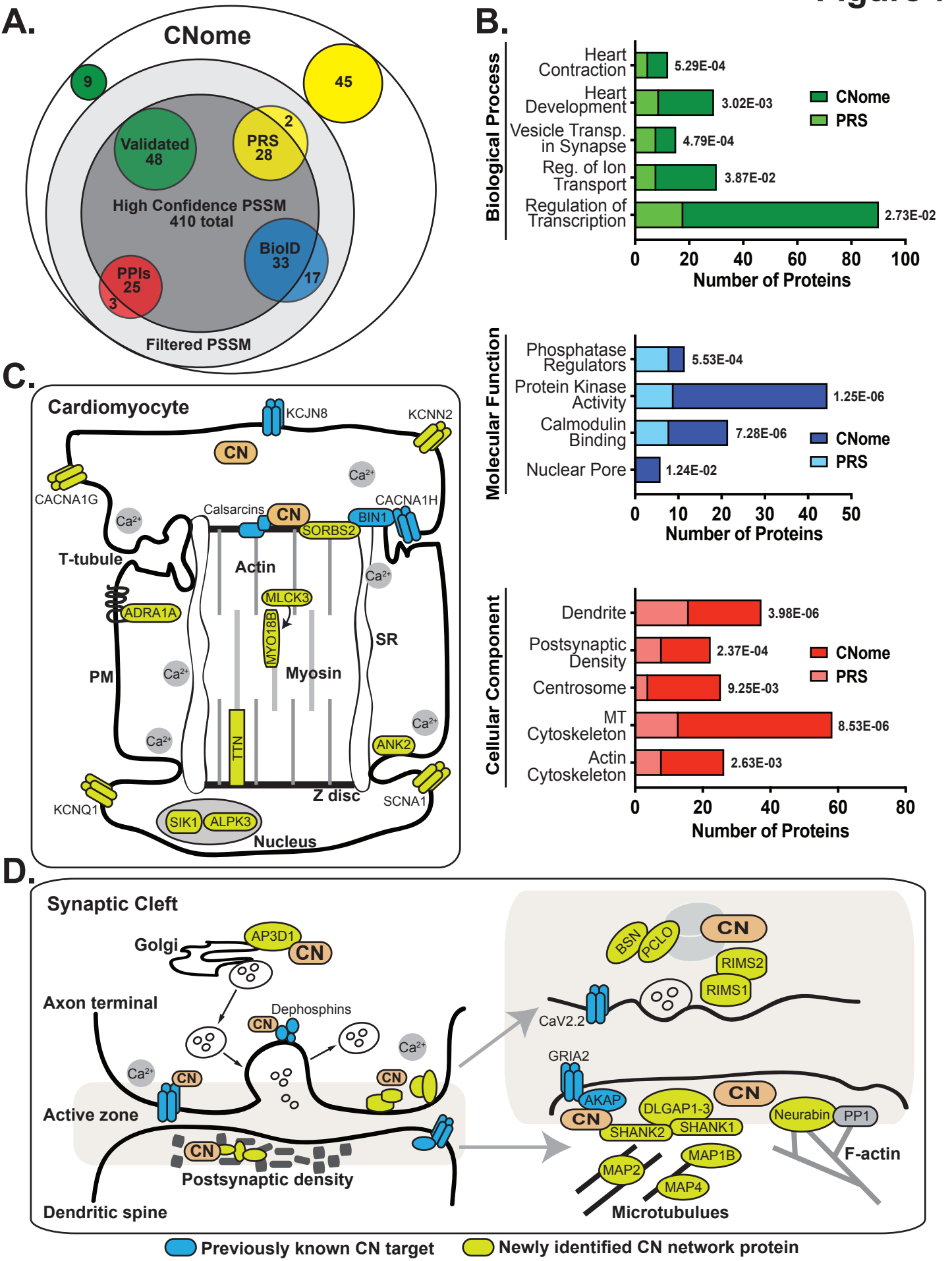

bioRxiv preprint doi: https://doi.org/10.1101/632547; this version posted May 9, 2019. The copyright holder for this preprint (which was not certified by peer review) is the author/funder. All rights reserved. No reuse allowed without permission.

Supplemental Figure 1

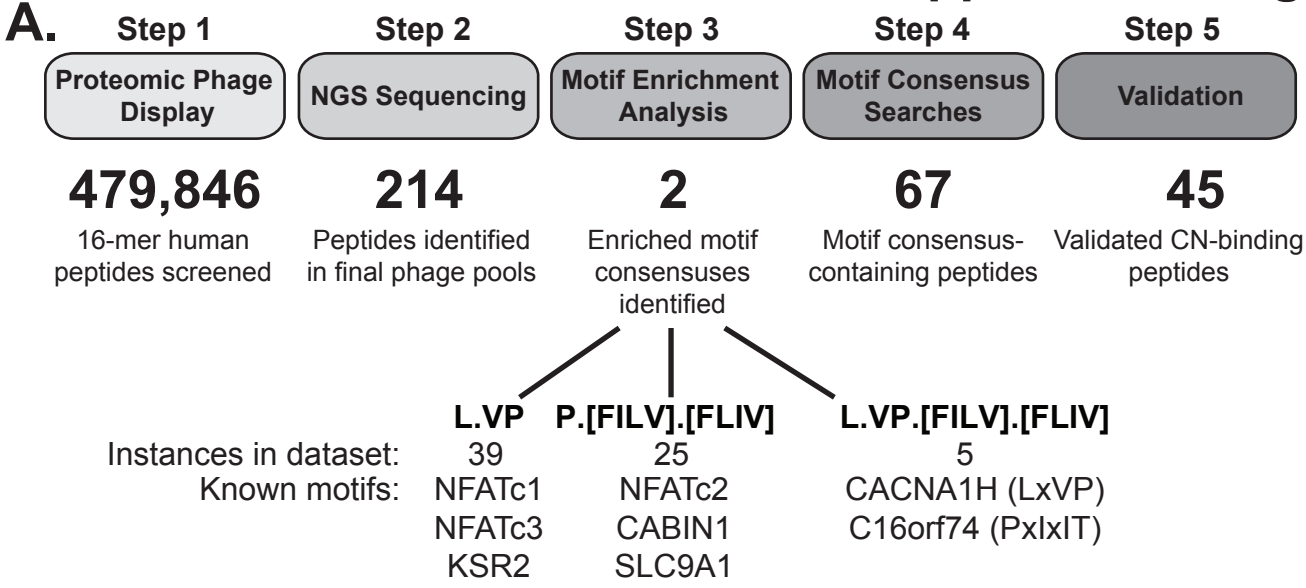

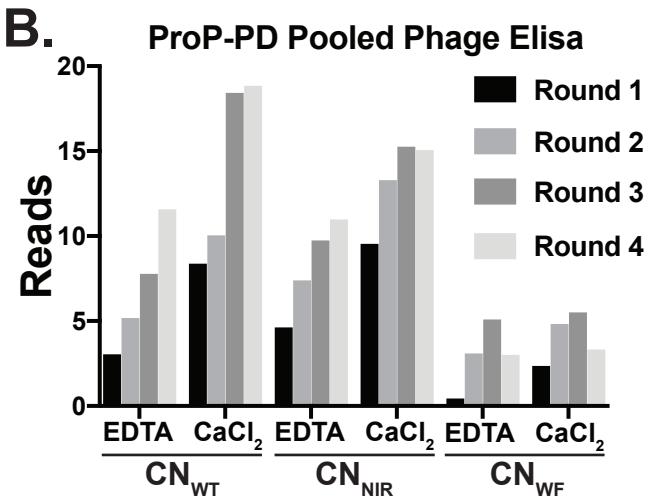

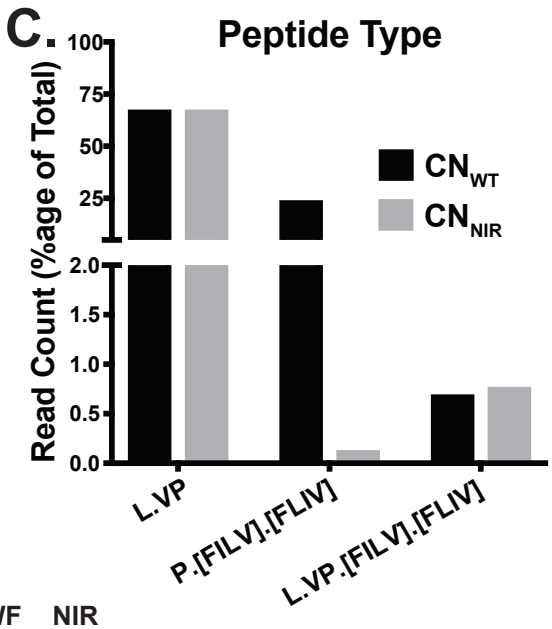

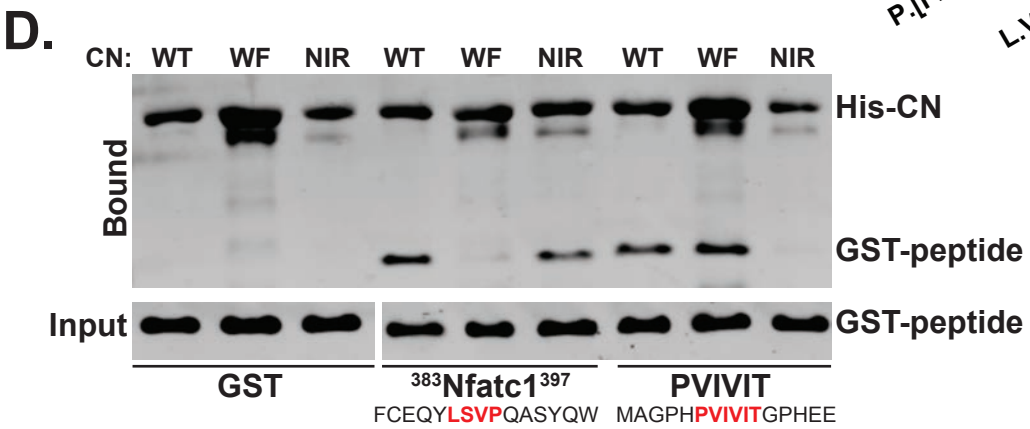

bioRxiv preprint doi: https://doi.org/10.1101/632547; this version posted May 9, 2019. The copyright holder for this preprint (which was not certified by peer review) is the author/funder. All rights reserved. No reuse allowed without permission.

Supplemental Figure 2

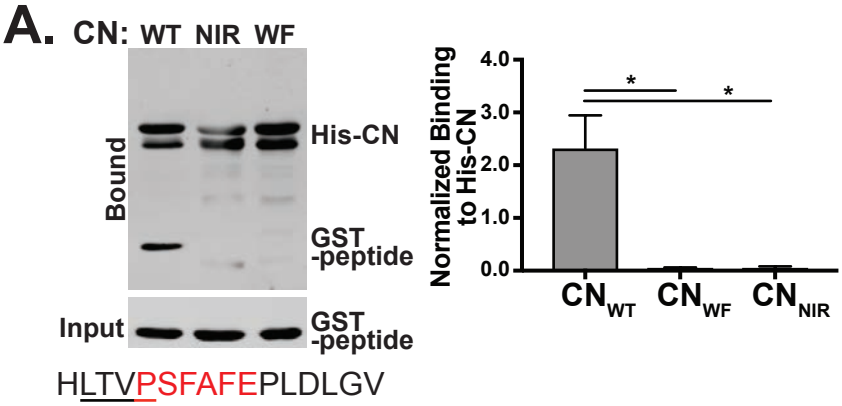

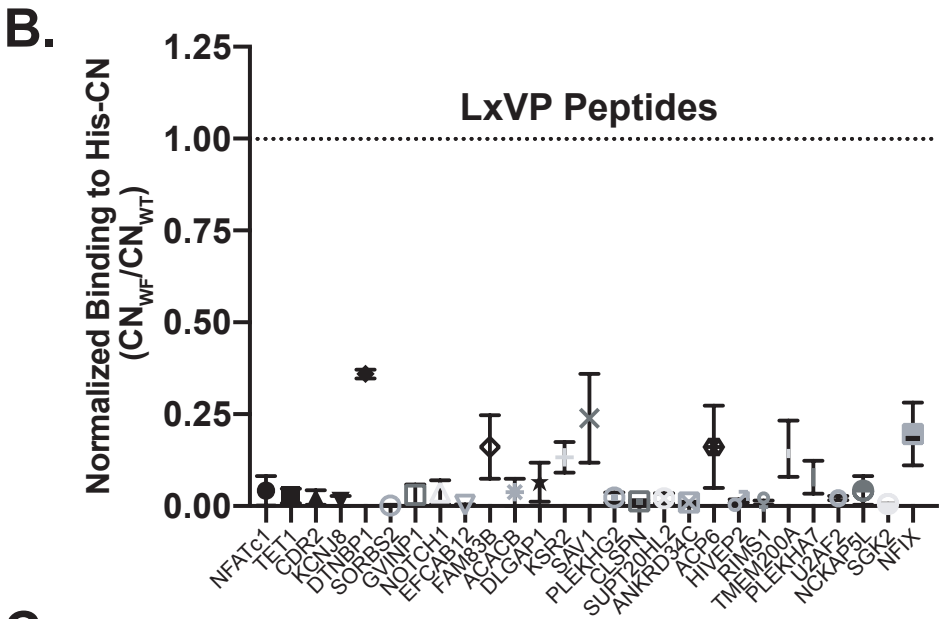

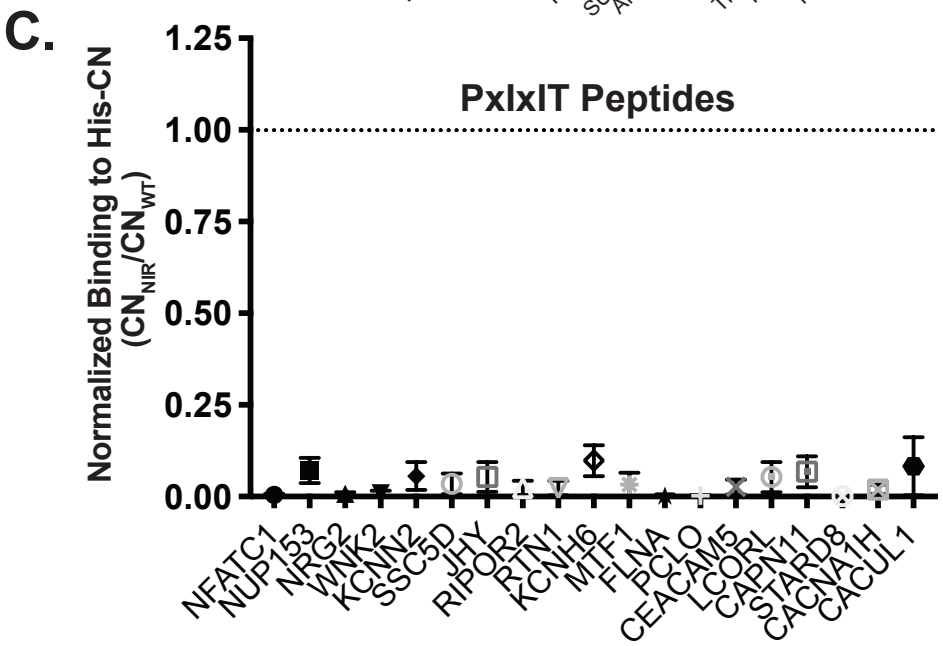

bioRxiv preprint doi: https://doi.org/10.1101/632547; this version posted May 9, 2019. The copyright holder for this preprint (which was not certified by peer review) is the author/funder. All rights reserved. No reuse allowed without permission.

Supplemental Figure 3

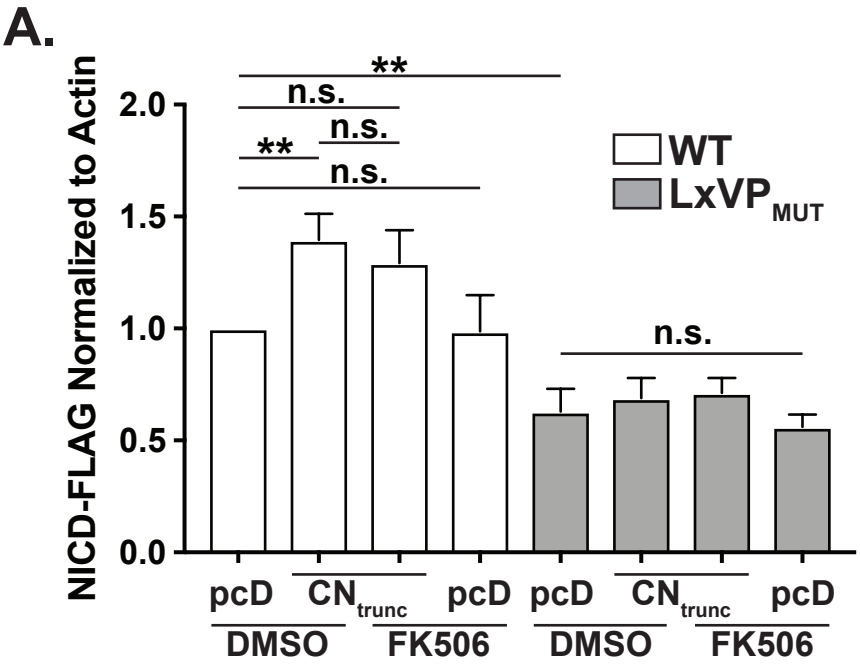

bioRxiv preprint doi: https://doi.org/10.1101/632547; this version posted May 9, 2019. The copyright holder for this preprint (which was not certified by peer review) is the author/funder. All rights reserved. No reuse allowed without permission.

Supplemental Figure 4

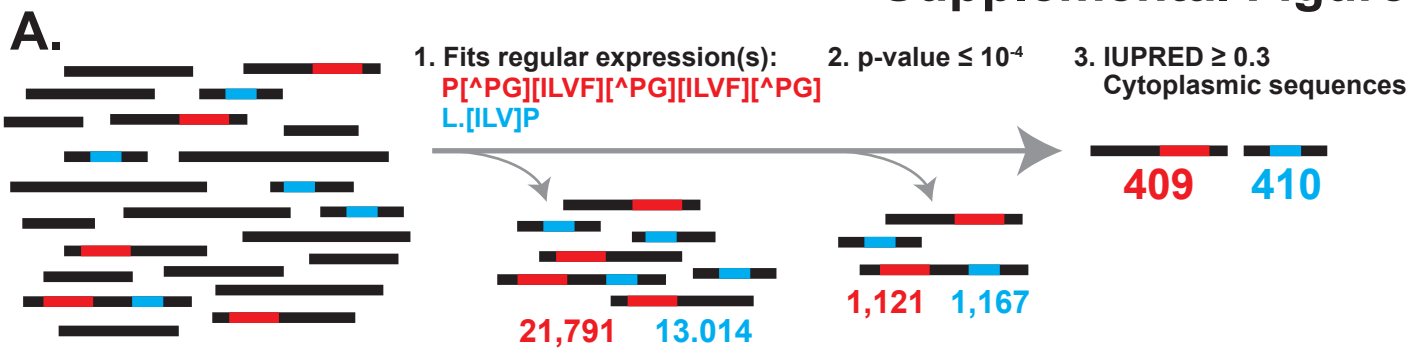

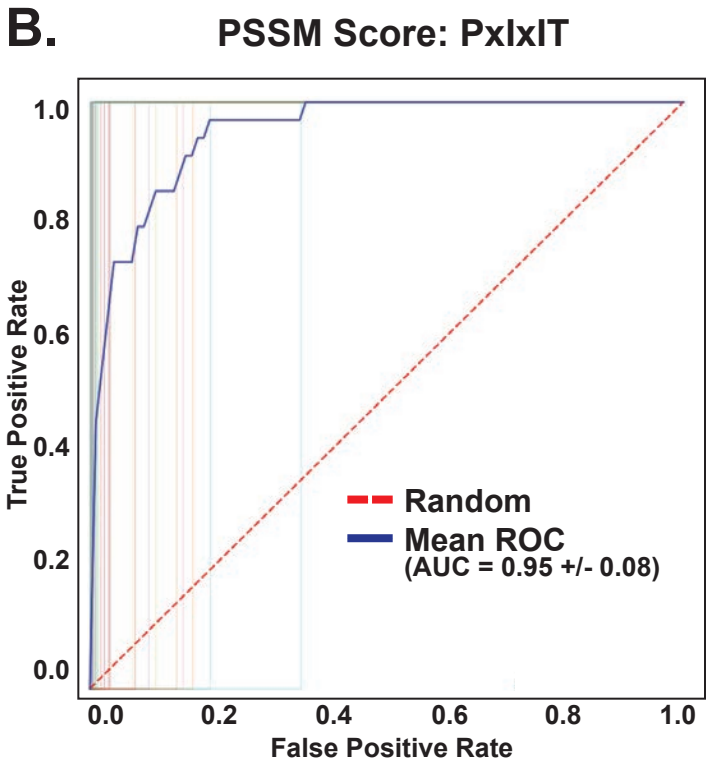

Mean Accuracy:	0.96
Mean AUC:	0.95
Mean Sensitivity:	0.73
Mean Specificity:	0.96
Mean Strength:	0.84

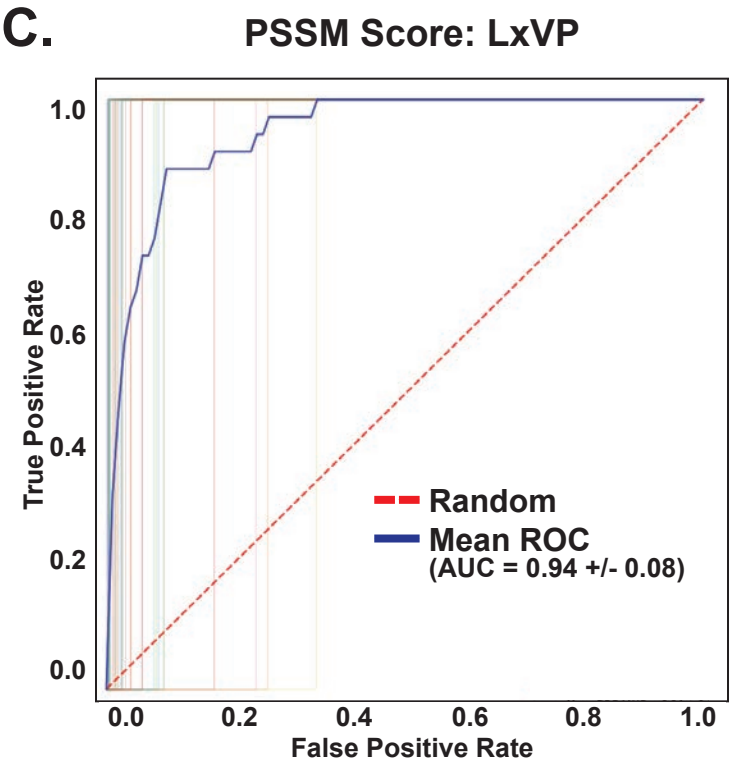

Mean Accuracy:	0.91
Mean AUC:	0.94
Mean Sensitivity:	0.82
Mean Specificity:	0.91
Mean Strength:	0.87

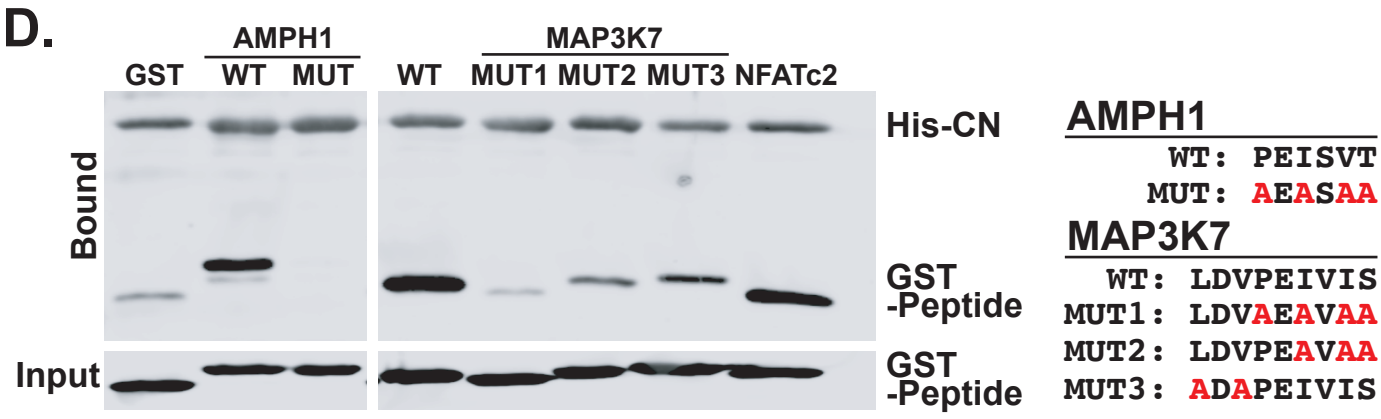

bioRxiv preprint doi: https://doi.org/10.1101/632547; this version posted May 9, 2019. The copyright holder for this preprint (which was not certified by peer review) is the author/funder. All rights reserved. No reuse allowed without permission.

Supplemental Figure 5

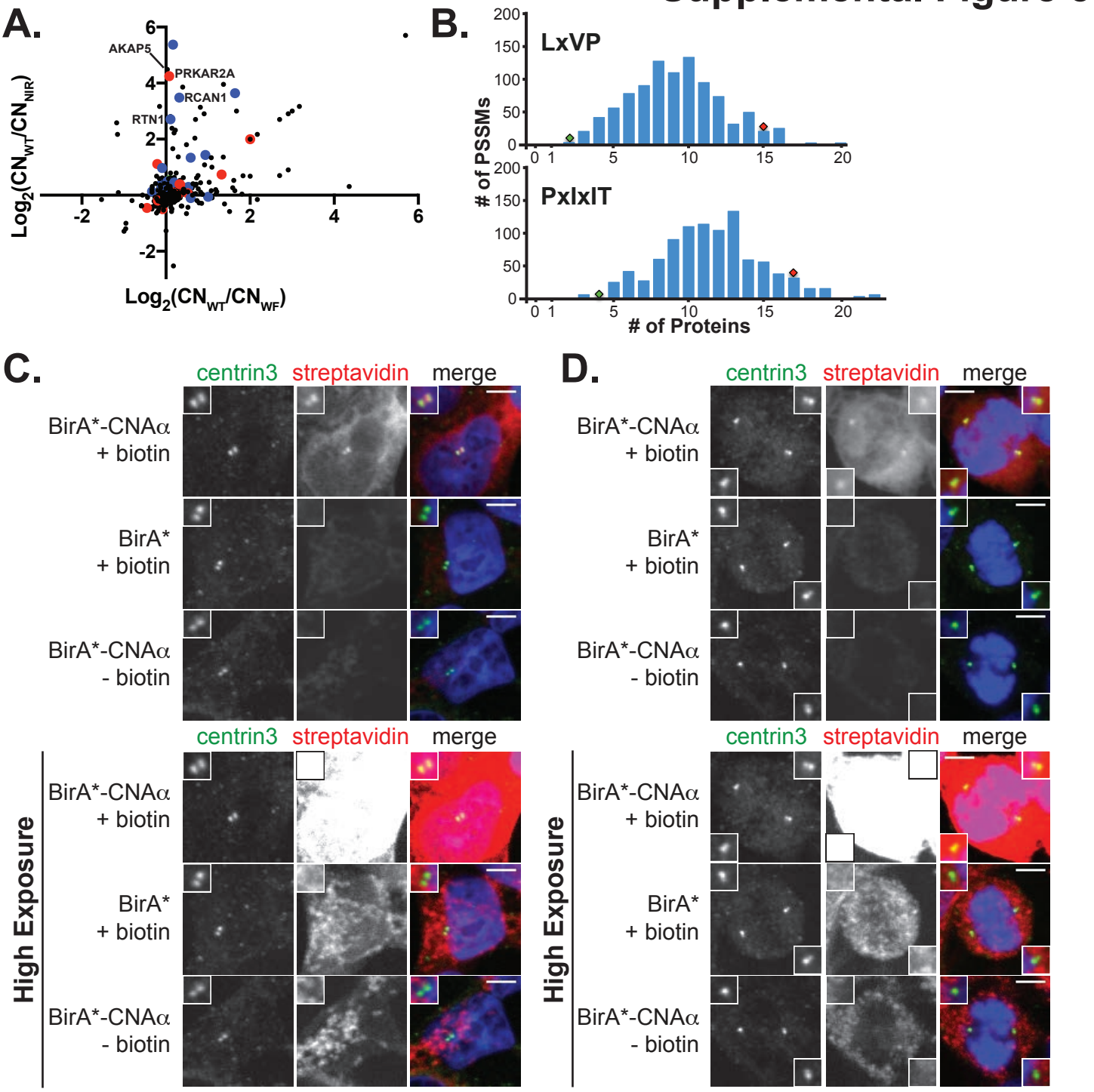

bioRxiv preprint doi: https://doi.org/10.1101/632547; this version posted May 9, 2019. The copyright holder for this preprint (which was not certified by peer review) is the author/funder. All rights reserved. No reuse allowed without permission.

Supplemental Figure 6

A.

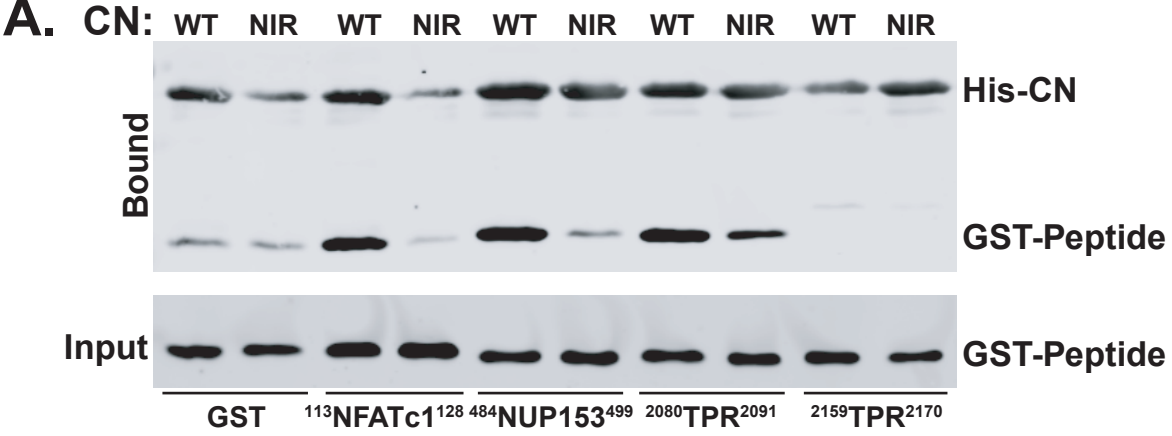

NFATc1: PALESPRIEITSCLGL
NUP153: LPTFNFSSPEITTSSP
TPR (2080-2091): PLPPRLTIHAPP
TPR (2159-2170): AGVPRFRFGPPE

B.

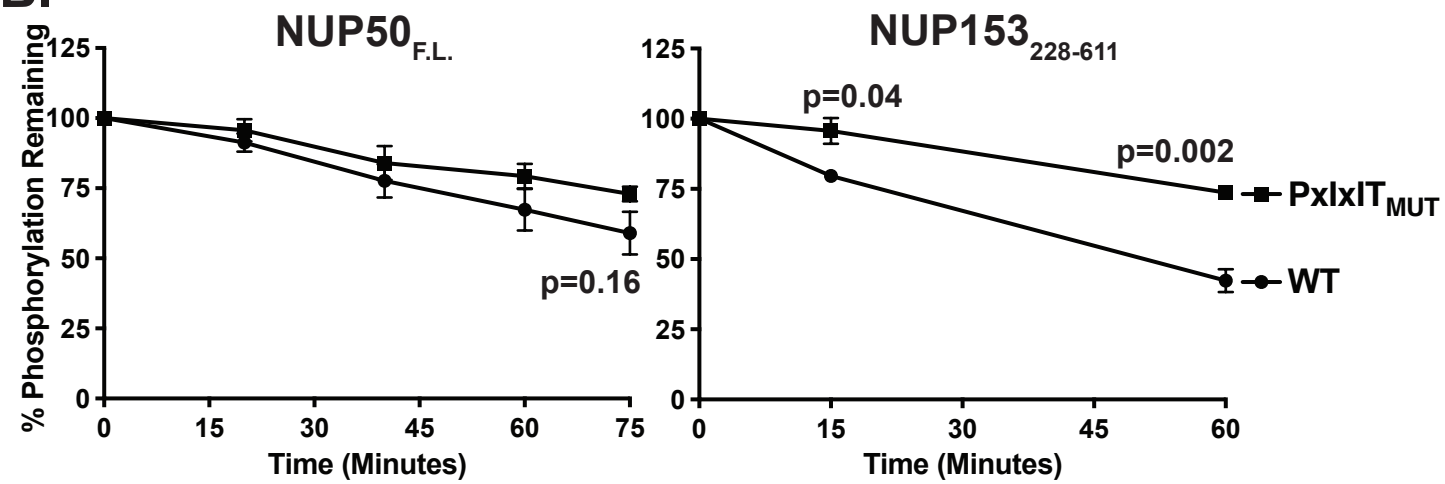

bioRxiv preprint doi: https://doi.org/10.1101/632547; this version posted May 9, 2019. The copyright holder for this preprint (which was not certified by peer review) is the author/funder. All rights reserved. No reuse allowed without permission.

Supplemental Figure 7

A.

	Valid.	PRS	PPIs/ PSSM	BioID/ PSSM	H.C. PSSM
Valid.	57	16	11	5	48
PRS	16	75	14	5	28
PPIs/ PSSM	11	14	28	4	25
BioID/ PSSM	5	5	4	50	33
H.C. PSSM	48	28	25	33	410